CRITICAL REVIEW

Unveiling additively manufactured cellular structures in hip implants: a comprehensive review

Juliana Marques Dias[1] · Filipe Samuel Correia Pereira da Silva[1] · Michael Gasik[2] ·
Maria Georgina Macedo Miranda[3] · Flávio Jorge Fernandes Bartolomeu[1]

Abstract

The prospect of improved quality of life and the increasingly younger age of patients benefiting from Total Hip Arthroplasty will soon lead to the landmark of 10 million interventions per year worldwide. More than 10% of these procedures lead to significant bone resorption, increasing the need for revision surgeries. Current research focuses on the development of hip implant designs to achieve a stiffness profile closer to the natural bone. Additive Manufacturing has emerged as a viable solution by offering promising results in the fabrication of implant architectures based on metallic cellular structures that have demonstrated their capacity to replicate bone behavior mechanically and biologically. Aiming to offer an up-to-date overview of titanium cellular structures in hip implants, for both acetabular and femoral components, produced by Additive Manufacturing, including its design intricacies and performance, this comprehensive review meticulously examines the historical development of hip implants, encompassing commercial solutions and innovative attempts. A broad view of the practical applications and transformative potential of hip implants incorporating cellular structures is presented, aiming to outline opportunities for innovation.

✉ Juliana Marques Dias
marquesdias.juliana@gmail.com

Filipe Samuel Correia Pereira da Silva
fsamueldem@uminho.pt

Michael Gasik
michael.gasik@aalto.fi

Maria Georgina Macedo Miranda
gmiranda@ua.pt

Flávio Jorge Fernandes Bartolomeu
flaviojorgebartolomeu@gmail.com

1　Center for MicroElectroMechanical Systems
(CMEMS-UMinho), University of Minho, Campus de
Azurém, 4800-058 Guimarães, Portugal

2　Department of Materials Science and Engineering, School
of Chemical Technology, Aalto University Foundation,
Aalto, 00076 Espoo, Finland

3　CICECO, Aveiro Institute of Materials, Department
of Materials and Ceramic Engineering, University of Aveiro,
3810-193 Aveiro, Portugal

Nomenclature

3D	Three-dimensional
Alu	Alumina
AM	Additive manufacturing
CaCO	Calcium carbonate
CAD	Computer-aided design
CM	Conventional manufacturing
Co	Cobalt
CoCr	Cobalt-chromium
CoCrMo	Cobalt-chromium-molybdenum (commercial name: vitallium)
Cr	Chromium
D	Diamond-like
DS	Diamond-like with support
DIC	Digital image correlation
DMLS	Direct metal laser sintering
EBM	Electron beam melting
EBMP	Electron beam melting-processed
Fe	Iron
FE	Finite element
FEA	Finite element analysis
FGM	Functionally graded materials

FoV	Field of view
H	Honeycomb-like
HS	Honeycomb-like with support
HA	Hydroxyapatite
HMWPE	High molecular weight polyethylene
LENS	Laser-engineered net shaping
LPBF	Laser powder bed fusion
LRM	Laser rapid manufacturing
MES	Minimal effective strain
Mg	Magnesium
MgCO	Magnesium carbonate
Mo	Molybdenum
MSC	Mesenchymal Stem Cells
Nb	Niobium
NHOst	Normal human osteoblast cells
PBF	Powder bed fusion
PBS	Phosphate-buffered saline
PE	Polyethylene
PJI	Prosthetic joint infection
PPS	Polyphenylene sulfide
PTFE	Polytetrafluoroethylene
PU	Polyurethane
SDGPS	Schwartz diamond-graded porous structures
Sl	Silica
SOMA	Stryker orthopedics modeling and analytics
SS	Stainless steel
St	Steel
STSR	Strength-to-stiffness ratio
STVR	Surface-to-volume ratio
Ta	Tantalum
TAOR	Triply arranged octagonal rings
THA	Total hip arthroplasty
Ti	Titanium
Ti6Al4V	Alpha-beta titanium alloy
TiAlV	Titanium-aluminum-vanadium
Ti-VPS	Titanium vacuum plasma spray
TPMS	Triple periodic minimal surface
UHMWPE	Ultra-high-molecular-weight polyethylene
Va	Vanadium
VEHXLPE	Vitamin E-infused highly cross-linked polyethylene
YM	Young's modulus
YS	Yield strength
Zi	Zirconia
Zr	Zirconium

1 Introduction

Humankind's quest for constant improvement and evolution began in the primordial eras. For this reason, an enduring mission to explore every conceivable outcome and discover optimal solutions has emerged. In the past, the treatment for hip diseases was radical and relied on limb amputation [1]. Following the introduction of John Charnley's low-friction arthroplasty concept, surgical procedures became less burdensome for patients, substantially enhancing their quality of life. Nonetheless, this prosthetic innovation has been linked to several complications [2–8]. Some of these issues have diminished over time, while others have gained prominence.

Initially, chronic infection and resulting pain were common issues in limbs with the prosthesis due to the use of materials such as wood or ivory that were not well tolerated by human cells [9, 10]. Attempts were made to address these problems by using materials like glass [11], acrylic resin [12], and polytetrafluoroethylene (PTFE) [13]. However, these materials proved to be too fragile to withstand joint stresses, and some did not alleviate the pain, leading to implant failure [14].

Over time, with adjustments in materials and designs, surgeons were able to identify specific combinations that did not have immediate adverse effects. Nevertheless, 10% of all Total Hip Arthroplasty (THA) will fail after 15 years of the incision [15]. In these cases, the individuals may experience pain, limited mobility, and a decrease in overall well-being due to complications such as implant wear or loosening. This discomfort can impact daily activities, hinder mobility, and reduce the ability to enjoy an active lifestyle. The primary approach to address this issue is through implant revision surgery. However, the period until needing another surgery reduces to half, every time [15].

As the prevalence of THA and revision of THA increases [16–19], the demand for innovation in enhancing bone cell responses for improved fixation and load distribution becomes dominant. The intricate cellular structure of trabecular bone exhibits remarkable lightweight properties and exceptional energy absorption capabilities. The incorporation of porous structures in implants is believed to mimic the cancellous bone, fostering bone ingrowth within the pores [20–24] and driving the need for cutting-edge solutions. Mimicking this sophisticated design, engineered cellular structures are set to revolutionize the biomedical area. Consequently, these structures are extensively studied with a focus on their application in the orthopedic field, especially to reduce implant weight and minimize existing complications. However, a current and comprehensive review encompassing titanium lattice structures produced through Additive Manufacturing (AM) technologies in the orthopedic sector, examining their potential for bone replacement, and consolidating ongoing research endeavors centered on the integration of cellular structures into significant components of hip implants, including both acetabular and femoral components, remains notably absent.

This review delves into the historical context and evolution of hip implants, offering an overview of solutions for hip arthroplasties since 1880, comparing them with current options. It explores persistent issues in hip arthroplasties,

examining commercial solutions and patents proposing innovative concepts, such as fully porous shells or coatings, as well as advanced techniques like additive manufacturing. The potential of this technology in orthopedics was recognized, assessing the mechanical and biological performance of metallic structures, including various types found in the literature. The cellular structures that strike an ideal balance between key properties like Young's modulus, porosity, and pore size for hip implant applications are identified. The final goal of this review is to deliver an exhaustive narrative that traces the historical evolution of hip implants up to the present advancements, focusing on the integration of cellular structures within these implants, both acetabular and femoral components. With a comprehensive analysis of the development and contemporary research in the field, this review aims to offer insights into the transformative potential of hip implants incorporating cellular structures in real-world scenarios.

1.1 Historical context

The first instance where limb sacrifice was not required to preserve the joint occurred in 1821. This procedure, performed by Anthony White, involved the excision of the head of the femur, known as Excision Hip Arthroplasty [1, 25, 26]. In 1826, John Rea Barton developed the first Osteotomy, specifically when articular movement ceased and true anchylosis had taken place [27]. Incisions were made on the pelvic and/or femoral bone to reshape them, thereby improving femoral head coverage and stabilizing the hip joint [9, 28, 29]. Despite these revolutionary procedures, restoring joint mobility remained a challenge. Carnochan nearly reached the benchmark for the first hip implant replacement in 1840 by replacing the hip joint with wooden blocks between the damaged ends, the Interposition Arthroplasty. The poor material prompted Auguste Verneuill to develop Soft Tissue Interposition Arthroplasty in 1860 [9].

The human skeleton's structure laid the groundwork for modeling implants. In 1880, Themistocles Gluck pioneered artificial knee, elbow, wrist, shoulder, and hip implants from ivory [10, 30]. Gluck also introduced fast-hardening cement within the marrow [9, 10] for hip implant fixation [31], yet he faced chronic infections in all joint replacements [31].

The fascinating journey of hip implant innovation initiates in 1919 when Pierre Delbet pioneers a rubber femoral prosthesis for hip replacements [1]. Then, in 1923, Marius Smith-Petersen introduces the "mould," initially made of glass and seated on the femoral head. Over time, materials evolve into Pyrex, Bakelite, and finally Vitallium, a cobalt-chromium alloy, marking a pivotal moment in 1938 with over 500 implants by 1947 [11, 14]. Further experiments unfold, like Phillip Wiles' attempt with stainless steel in 1938 [14, 30], and Austin T. Moore and Harold Ray Bohlman's Vitallium

femoral implant driven into the medullary canal in 1940 [32, 33]. The late 1940s bring the Judet brothers, who implant an acrylic resin femoral head [12, 14]. Finally, in 1950, Frederick Roeck Thompson refined the Moore prosthesis, eliminating fenestrations and introducing a stem collar, a testament to the ever-evolving world of hip implant innovations [33].

At the Royal National Orthopaedic Hospital in Stanmore, a pioneering THA endoprosthesis emerged in 1963, offering effective pain relief until 1997 [34]. Subsequent innovations primarily involved modifications to existing models. The Thompson implant, introduced between 1956 and 1960 by G. K. McKee and J. Watson-Farrar, featured a reduced femoral component head dimension and a chrome-cobalt alloy cup attachment [35]. Additionally, Peter A. Ring enhanced Moore's prosthesis in 1964 with an acetabular component comprising a simplified cup and a posteriorly redesigned long stem to reinforce the junction area [36].

John Charnley, known as the modern THA pioneer, introduced low-friction arthroplasty in the 1950s using PTFE for the acetabulum's interior shell and the femoral head's exterior shell [1, 37–40]. However, in 1961, high molecular weight polyethylene (HMWPE) replaced PTFE due to its superior wear resistance, being 500–1000 times more wear-resistant [13]. In 1974, Gilles Bousquet and André Rambert introduced the dual mobility cup for the acetabular component [41]. The 1983 release of the Robert Mathys (RM) Classic monoblock cup featured two variants: Classic RM, a special surface finishing, and Classic HA, with a hydroxyapatite (HA) layer.

In the early 2000s, the RM Press-Fit cup came to the forefront but was later succeeded by the RM Vitamys, incorporating the transition from ultra-high molecular weight polyethylene (UHMWPE) to vitamin E-infused highly cross-linked polyethylene (VEHXLPE) [42]. Simultaneously, a modular cup system was developed by PINNACLE®, DePuy Synthes, available today.

The development of the femoral component progressed alongside the acetabular component. In 1970, Pierre-Boutin developed a ceramic-on-ceramic bearing [30, 43], while Robin Ling and Clive Lee introduced a stainless-steel alloy EN58J double-tapered and polished stem with a 30-mm head called Exeter, intended for cement fixation [44, 45]. Variations of the Exeter™ followed, such as the Exeter Universal, with a distal taper, in 1988 [45], and the Exeter™ V40™, with a centralizer, since 2002 [46]. Professor Müller introduced a straight stem with standard and lateralizing versions in 1977 and, a decade later, a self-locking straight stem [47]. The Taperloc, a collarless femoral component with Ti6Al4V porous coating, gained recognition in 1983 [48]. From 1986 to 1990, the Corail® Ti6Al6V4 stem with microtextural features and hydroxyapatite coating was introduced [49]. Based on Müller Straight Stem and the Corail® cementless HA-coated stem, the cementless Avenir stem,

incorporating Ti6Al4V alloy with macro surface structure, titanium plasma pre-coating, and full hydroxyapatite coating, was launched in 2005 [50].

The hip implant has seen notable changes in materials, design, and surface finishes. Despite these advancements, the fundamental concept remains unaltered. The significant shift from 2002 to the present is the utilization of AM for implant fabrication. The information sources encompassed review articles, survivorship reports, surgeon biographies, published articles, and books. Figure 1 offers a visual summary of the highlighted designs, showcasing the progression of this treatment over the years.

1.2 Commercially available hip implants

Based on the hip implant evolution described earlier, it is possible to understand that despite decades of evolution, current implants still adhere to the same designs with a few modifications, primarily focusing on surface topography [57]. These implants can be categorized into three types: cemented, cementless, or hybrid. In the cemented category, as the name suggests, acrylic cement is used [58, 59] not to fixate the prostheses to the surrounding bone, but rather to serve as an interposition layer between the bone and the implant, accommodating the stresses caused by the difference in stiffness between them

[60]. Cementless fixation is characterized as a press-fit fixation [60], wherein the implant is inserted into a bone canal prepared by the surgeon [58]. These implant components typically feature a porous coated surface to promote osteointegration and enhance initial stability [58–60]. The coating can include plasma-sprayed hydroxyapatite, sintered titanium beads, plasma-sprayed titanium, biomimetic titanium coatings, and others [59, 60]. Hybrid fixation refers to an implant fixation where one component is cementless while the other is fixated with bone cement [61]. Therefore, the design of the implant depends on the fixation type. For instance, in cementless fixation, the surface needs to be porous to facilitate osteointegration. Conversely, in cemented fixation, an end cap/centralizer is provided to enable the stem to subside within the cement mantle without end bearing, ensuring optimal load transfer [51]. These types of implant fixation are represented in Fig. 2.

The current THA relies primarily on two components: the acetabular component and the femoral component, depicted in Fig. 2. The most recent acetabular component used is the dual mobility cup, which consists of an acetabular cup with or without an inserted shell. It is fixated into the pelvis by press-fit (sometimes coupled with screw fixation) or by bone cement. The acetabular liner, mechanically locked in the shell, serves as a tribological surface. It undergoes wear as the femoral head moves inside the acetabular cup, providing

Fig. 1 Hip implant evolution (adapted and schematized from references [11, 13, 14, 30, 31, 33–35, 37, 38, 42, 48, 49, 51–56])

Fig. 2 (**a**) Type of fixation of implants, represented in the stems. (**b**) Type of component and denomination of the different parts of a hip implant (adapted and redrawn from references [38, 60])

(a) Fixation

Cement

Centraliser

Cementless   Cemented

(b) Components

Acetabular component

Neck

Stem
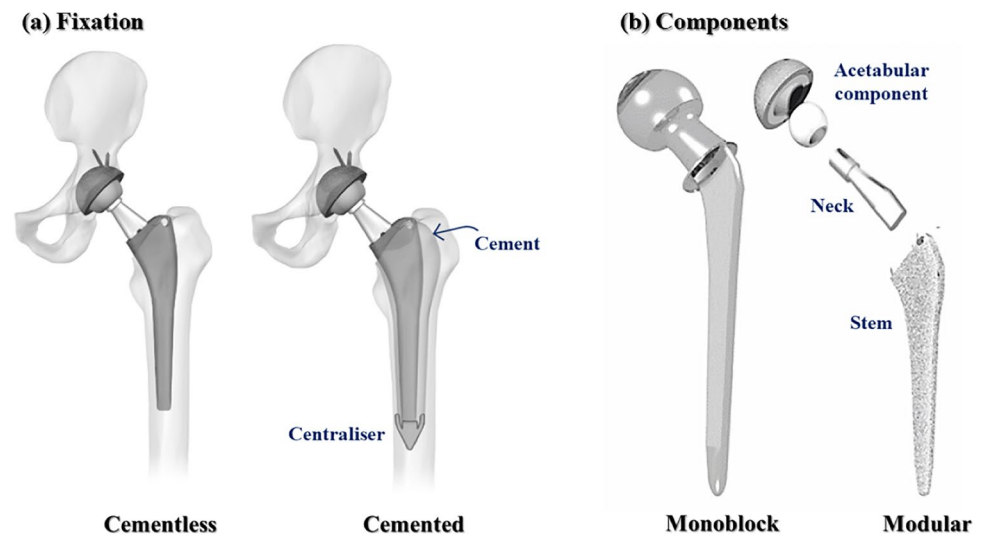
Monoblock   Modular

improved stability, reduced impingement, and lower friction and wear [41, 52]. These two parts can be separated with a modular acetabular cup, or they can be factory-preassembled in a single piece, known as a monoblock acetabular cup [62].

The femoral component consists of a stem and a femoral head. In the case of a monoblock femoral component, the stem and the femoral neck are joined in a single piece. However, in a modular femoral component, the two components are connected by a taper junction [59, 60, 63]. In some cases, a dual modular femoral component includes tapper junctions between the stem, the neck, and the femoral head [63]. Similar to the acetabular cups, the presence of taper junctions in the modular type allows for greater customization, enabling a more patient-specific neck length and orientation. However, this type of implant is more susceptible to fretting corrosion due to the increased number of components and taper junctions [59, 60].

The femoral component can be characterized by its size, either conventional or short stem, with the latter being smaller than the conventional and having a length of less than 120 mm [64]. A short stem aims to closely resemble the anatomical pattern of stress distribution and allow for reduced bone resection [65]. As the name suggests, this component is fixed in the femoral bone within a canal prepared by the surgeon.

The design for the femoral component is chosen based on factors such as geometry, shape, length, and location of the implant, presence or absence of collar support, stem cross-section and offset, surface finishing, the importance of a monoblock or modular stem, type and location of primary fixation, and bone preservation [60]. Despite numerous studies on the effect of each option, it remains challenging to establish definitive results for each parameter due to the multitude of factors that can influence the overall outcome. For example, regarding the option of stem collar support,

some studies argue that this feature significantly affects immediate stability compared to collarless stems [66], while others suggest that the presence of a collar support does not cause major differences in the primary stability of the stem [67]. These discrepancies may arise from variations in stem design, insertion approaches, and differences in bone properties among patients, making it difficult to attribute specific outcomes solely to the presence of stem collar support. Similar considerations apply to all the different design options, warranting further investigations that encompass as many factors as possible to find optimal solutions.

The materials for each implant component are chosen based on their specific requirements, such as the need for stiffness, fatigue resistance, roughness, and diameter. The most commonly used materials for the femoral stem and acetabular cup shell are metals, while the femoral head and acetabular cup liner can be made of materials from the metal, ceramic, or polymer classes [59].

In terms of hip implant production, the global market leaders are Zimmer, DePuy, Johnson & Johnson, and Stryker [68–72]. Their main offerings for different hip prosthesis components are summarized in Table 1 and Table 2.

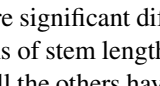Regarding the presented acetabular systems, the major difference between them lies in the surface finishing and geometry of the acetabular cup. Since this structure will be in contact with the bone and achieving bone ingrowth is a desired outcome, these systems incorporate features to enhance it. Regardless of the manufacturer, all have porous surfaces [53, 76, 80], geometrical structures [74], or a combination of both [78] to promote bone and cement fixation. These systems are characterized by dual mobility, allowing the option of using a liner between the femoral head and the cup. To achieve a porous surface, the shells are made of porous materials obtained through AM techniques like Laser Powder Bed Fusion (LPBF) [53, 79, 80] or porous coating

Table 1 Acetabular cup/system main offers from Zimmer, DePuy, Johnson & Johnson, and Stryker

Manufacturer	Reference	Main Features	
		Details	Schematic
Zimmer	Avantage® Dual Mobility [73]	• Cementless OR Cemented; • Non-constrained system; • Extended head coverage; • Possibility of using polymeric bearings with metal or ceramic modular heads	
	Allofit® [74]	• With OR without screw fixation; • Possible to combine with all current tribological bearings and different articulation diameters; • Polar region flattened; • Macrostructure with 1,000 teeth – 1mm in height	
	G7® [53, 75]	• With screw fixation; • E1® Antioxidant Infused Technology via Vitamin E; • Preassembled constraining ring; • Possible increased ranges of motion; • OsseoTi® Porous Metal technology; • Average pore size of 475μm	
DePuy, Johnson & Hohnson	PINNACLE® [54, 76]	• Cementless with OR without screw fixation; • GRIPTION® and POROCOAT® Porous Coatings; • DUOFIX® Porous Coating is also available on select cups; • ALTRX® Polyethylene Liner; • BIOLOX® delta Ceramic Heads	
	BI-MENTUM™ [77, 78]	• Cemented or Cementless with OR without screw fixation; • Monoblock dual mobility cup; • Stainless steel cup with a plasma-sprayed Ti and HA coating (cementless cup); • Radial and annular grooves (cemented cup)	
Stryker	Trident® II [79, 80] Acetabular shell	• Cementless; • Fixation with screw holes; • Slim shell wall; • Average pore size is 434μm;	
	Modular Dual Mobility® [81]	• Cementless; • Offers the option to use cancellous bone screws; • Modular having two points of articulation; • Possibility of coupling with Trident II	
	Anatomic Dual Mobility® [82]	• Cementless; • Two points of articulation; • Anatomic shell; • Plasma sprayed Ti surface overlayed with HA; • Peripheral self-locking.	

Table 2 Femoral stem main offers from Zimmer, DePuy, Johnson & Johnson, and Stryker

Manufacturer	Reference	Main Features	
		Details	Schematic
Zimmer	Avenir™ [55]	• Cementless; • Collarless OR collared; • Reduced distal geometry; • Double-layered coating designed for long-term stability; • Macro-structure that increases bone contact surface area and eases insertion of the stem; • Rectangular cross-section with smoothed edges designed for rotational stability	
	Taperloc™ [83]	• Cementless; • Collarless; • Reduced distal geometry; • Circumferential PPS coating; • Distribution of pore size between 100 and 1000μm; • Tapered portion that provides a wedge effect and a rotational fixation	
	Fitmore® [56, 84]	• Cementless; • Curved and short length stem design; • Triple taper design with proximal Ti-Plasma coating; • Trapezoidal cross-section with Ti-VPS coating proximally and rough-blasted distally	
DePuy, Johnson & Johnson	CORAIL® [85]	• Cementless; • Collared OR collarless; • Tapered neck geometry and ARTICUL/EZE™ Hip Taper designed to increase range of motion; • Vertical/horizontal grooves; • HA coating; • Step geometry	
	SUMMIT® Tapered [86]	• Cementless; • Collarless; • POROCOAT® Porous Coating; • DUOFIX® HA Coating; • Radial ZTT™ Steps; • Direct Lateralization	
	C-STEM® AMT [87]	• Cemented; • Collarless; • Presence of an end cap; • Polished and tapered design; • Triple taper stem section	
Stryker	Exeter® V40® [68, 88]	• Cemented; • Presence of an end cap; • Modular stem	
	Accolade® II [89, 90]	• Cementless; • Unique size-specific medial curvature; • Optimized stem length; • The distal geometry increases in size less than the proximal geometry; • Optimized length that accommodates muscle-sparing approaches and demonstrates improved initial stability	
	Insignia® [91, 92]	• Cementless; • Collared with a size-specific collar; • Direct lateral offset; • Low-profile shoulder; • Slim-distal profile	

[76, 78, 82, 93]. Except for the Anatomic Dual Mobility [82] and the Avantage® Dual Mobility [73], screw fixation can be used with almost every presented acetabular cup.

When it comes to femoral stems, there are significant differences in both surface and design. In terms of stem length, the Fitmore® has a short stem [84], while all the others have

standard stem lengths that can vary from short to longer based on the patient's needs. Regarding the porous surface, it is primarily achieved through porous coating [56, 85] or a combination of porous coating and surface blasting [55, 56, 86]. In this review, it is noted that there are some additively manufactured stems, such as the Accolade® II and the Insignia® TM stems, which are 3D CT-based designs created using the SOMA (Stryker Orthopaedics Modelling and Analytics) technology. This technology accurately designs the implant based on the patient's bone morphology through the acquisition of CT scans [90]. The C-STEM® and Exeter® V40® do not have a porous surface since these stems are used with cement. The presence of cement eliminates direct bone contact, so there is no need to enhance osteointegration.

## 2 Current issues and the need for innovation

Total hip arthroplasty's most common complications include dislocation, periprosthetic fracture, osteolysis, and aseptic loosening [2–7], often needing revision surgery [59, 94] and consequent implant replacement [2–8]. These challenges result from poor osteointegration between the bone and implant, leading to functional limitations and reduced patient quality of life. However, perioperative complications such as infection, nerve damage, and implant loosening can also significantly impact patient outcomes. Prosthetic joint infection (PJI) is a debilitating complication following THA, leading to increased morbidity and healthcare costs [61, 95]. The incidence of deep infection following primary THA is approximately 1% [59, 61, 95], emphasizing the importance of preventative measures during and after surgery. While surgical approaches may differ in their risk profiles, nerve injury remains a concern, with the sciatic nerve commonly affected in posterior THA. Surgeons' experience plays a crucial role in minimizing the risk of complications, underscoring the need for continuous training and improvement in surgical techniques [95, 96]. Nevertheless, this review primarily focuses on implant-related material issues and associated solutions, aiming to enhance the overall success and longevity of hip arthroplasty. Therefore, the dislocation, periprosthetic fracture, osteolysis, and aseptic loosening, represented in Fig. 3, will be discussed.

2.1 Dislocation

Implant stability has been a primary goal since the early days of THA. Initially, fixation problems were encountered with the use of screws [33] and bone cement composed of copper amalgam, plaster of Paris, or stone putty, which were prone to infection or loosening [10, 97]. Over time, various mechanisms have been developed to improve implant fixation

Fig. 3 Complications of hip implants (images adapted from references [99, 104, 260–264])
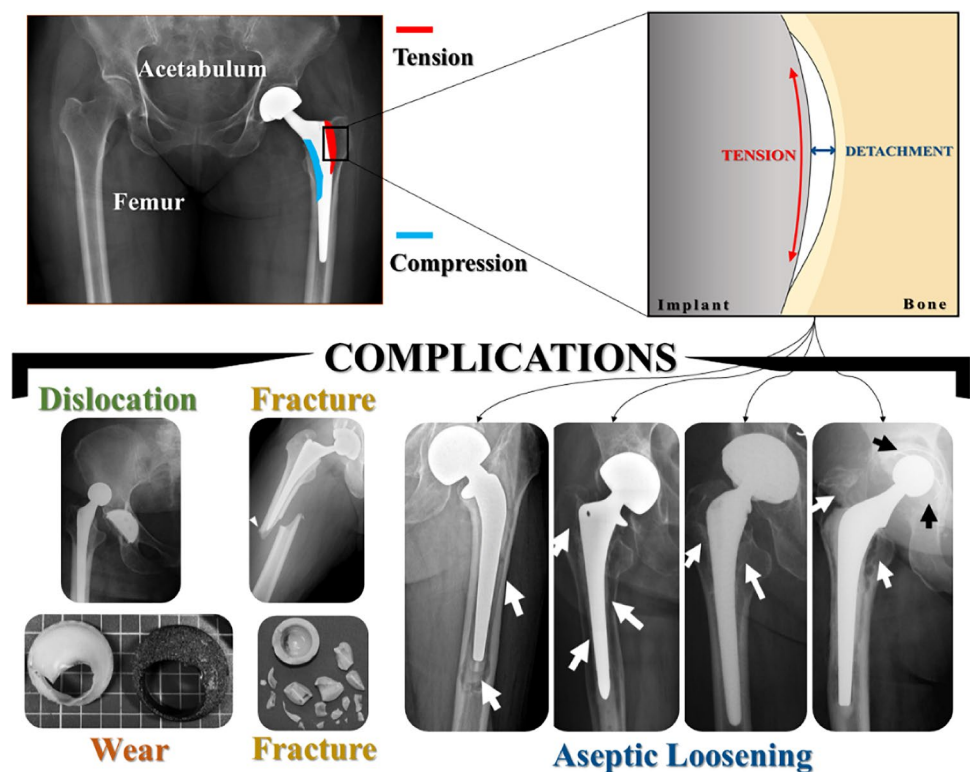
to the bone. Currently, cemented, cementless, and hybrid approaches are used, but stability remains a challenge.

Dislocation, as shown in Fig. 3, is a common complication that often occurs within the first two years [2–8]. It can be attributed to two factors: patient-related and surgical factors [98]. The surgical factors include the type of implant and the surgical approach chosen by the surgeon. In the past, larger femoral heads were preferred as they provided better stability [99]. However, there is now a growing interest in dual mobility cups, which offer a greater range of motion and potentially enhanced stability [100].

2.2 Periprosthetic fracture

Periprosthetic fractures, as depicted in Fig. 3, are primarily associated with the fixation of the implant, specifically in cases of cementless fixation [101, 102]. Moreta et al. [102] identified cementless fixation in almost 80% of the cases, regardless of patient sex, age, and stem design, as part of multiple risk factors that can contribute to this type of fracture [103]. This complication is of utmost importance, as the mortality following a periprosthetic fracture has been on the rise [102]. Therefore, significant attention has been given to identifying and addressing the risk factors associated with such fractures.

The increasing need for hip implants in younger individuals often requires the selection of cementless fixation, which can increase the risk of periprosthetic fractures [104]. Additionally, patient age plays a significant role, as older patients are more likely to have poor bone quality and medical comorbidities, making them more susceptible to bone fractures [102]. While the surgical approach has been identified as a potential risk factor, Sershon et al. [103] concluded that it is the stem design, rather than the surgical approach itself, that contributes to the risk.

2.3 Periprosthetic osteolysis

Periprosthetic osteolysis is a complication that is extensively discussed in the literature, although it is not commonly mentioned in various reports on hip arthroplasty, as attributing implant failure to this specific problem can be challenging. However, due to its association with particle wear and aseptic loosening, these complications are more prominently addressed in annual reports. The incidence of osteolysis with conventional bearings has been reported to vary widely, ranging from 5 to 60% after 10 years postoperatively [3, 5, 105], as supported by recent literature.

Periprosthetic osteolysis is characterized by a progressive and active biological cascade triggered as a local immune response in periprosthetic tissue, leading to bone resorption [105, 106]. While there are multiple factors associated with this response, wear particles are considered the primary cause [106]. Evidence suggests that wear debris, with sizes ranging from 0.1 to 1.0 μm, can be phagocytosed by macrophages [107], which then become activated and release osteolytic factors, stimulating osteoclasts to resorb the surrounding bone [95]. Consequently, the popularity of metal-on-metal prostheses increased, given their minimal production of debris. However, the debris from these prostheses, in the form of nanoscale and nanometric particles, cannot effectively stimulate phagocytosis by macrophages, resulting in a significant accumulation of these particles in the periprosthetic tissue [108]. There is evidence to suggest that the inability to expel these metal nanoparticles may be associated with the presence of pseudotumors or cellular toxicity. The active corrosion process of the metallic surface and the release of particles [108] contribute to the generation of metal ions, which can be absorbed by cells [59]. Due to these concerns, ceramic-on-ceramic bearings are preferred over metal or polyethylene alternatives. However, their brittleness and susceptibility to fracture, as well as associated issues like groin pain and noise, make this type of implant less suitable [109].

2.4 Implant loosening

Implant loosening, as depicted in Fig. 3, can be preceded by osteolysis [61, 107, 110, 111], which is attributed to the presence of wear debris. However, the main cause of implant loosening is the mismatch in strain between the stiffness of the bone and the metallic implant. This occurs when non-uniform contact pressures between the bone and implant result in atypical load transfer, leading to varying degrees of bone resorption. During locomotion, the femur experiences compression primarily from axial loads [112–114], causing tensile strains on its lateral and anterior sides and compressive strains on the medial and posterior surfaces [113–115], as shown in Fig. 3. This uneven strain distribution contributes to localized bone density changes in response to the applied stimuli [116–118]. The regions experiencing tension undergo bone retraction, reducing mechanical stimulation at the bone-implant interface and increasing the risk of wear particles entering the interface space, thereby making it more susceptible to fracture. This reduction in mechanical stimulation results in varying degrees of bone resorption along the length of the implant [113, 116–118].

The bone stimulus theory, first proposed by Wolff's law, states that bone undergoes internal architectural changes and external conformational alterations in response to changes in form and function, following mathematical laws [119]. A century later, Harold M. Frost introduced the mechanostat theory, which not only confirmed Wolff's Law but also assigned numerical values to the stimulus responses. Frost proposed the concept of a "minimum effective strain" (MES), which represents the minimum threshold for a signal

to trigger bone architectural adaptation [117, 120]. According to this theory, there are MES values for bone remodeling, bone modeling, and bone repair [117], as represented in Fig. 4. The range between these thresholds defines different areas, and the type of bone adaptation depends on the specific region, strain/ΔBone mass, and applied load [117, 120]. As shown in Fig. 4, when strains are below the remodeling MES at trivial loading levels, bone remodeling is activated, and it is expected a net reduction in bone mass. When strains are above the remodeling MES and below the modeling MES, the physiological loading level is maintained, preserving bone conditions without significant changes in bone mass [117, 118, 120]. If strains exceed the modeling MES but remain below the repair MES, an increase in bone mass occurs at the overload level. Conversely, if strains surpass the repair MES at the pathological overload level, new woven bone is formed on the bone surfaces, which is weaker than mature mineralized lamellar bone [120]. Alternatively, massive resorption can occur, leading to a higher risk of fracture or marginal bone loss [118]. It is important to highlight that these reactions are mediated by specialized cells, such as osteoblasts derived from mesenchymal stem cells (MSCs) and osteoclasts, which activate mediators to induce bone formation or resorption, respectively [117, 121–124].

In the presence of a metallic implant, a phenomenon known as stress shielding occurs due to the mismatch in stiffness between the implant and the bone, resulting in the implant bearing the body loads that should be borne by the bone [59, 94, 125, 126]. This leads to a lack of mechanical loading on the surrounding bone tissue, particularly at the interfaces between the bone and the implant or bone cement [59, 94, 125, 126]. Micromotion, which refers to small movements at the bone-implant

interface, plays a crucial role in ensuring the primary stability of the implant [127, 128]. Nevertheless, there are minimum and maximum thresholds for micromotion that are conducive to osteointegration. It has been documented that osteointegration occurs when the micromotion at the bone-implant interface is below 40 μm and can be tolerated up to 150 μm [129, 130]. If the micromotion exceeds this upper threshold, it can lead to the formation of fibrous tissues and ultimately promote implant loosening [128–131]. This excessive micromotion, particularly on the bearing surfaces, also contributes to the generation of wear debris as a result of friction, leading to particle disease [61, 111], known as third-body wear [61, 110].

The reduction of bone marrow is another factor associated with implant loosening. During the insertion of the prosthesis, the surgeon needs to penetrate the bone, invading the marrow cavity and interfering with the growth of bone marrow. Since the bone marrow is involved in bone cell differentiation [132], its reduction leads to a decrease in blood flow within the medullary cavity [104], thereby inhibiting bone modeling and remodeling processes, ultimately contributing to implant loosening.

2.5 Occurrence rate and future projections

The importance of medical treatment can be observed through the number of procedures performed annually within a population [59]. Hip replacement surgery is one of the most performed and effective procedures worldwide. In 2019, countries such as Germany, Switzerland, Austria, Finland, and Belgium had the highest rates of hip replacement surgeries, as represented in Fig. 5 [16]. These countries have a THA incidence exceeding 280 procedures per 100,000 inhabitants per year, indicating a global annual THA procedure count of approximately one million. Between 2009 and 2019, this rate procedure increased by 22% [16]. This trend is expected to continue in the coming decades, as shown in Fig. 6 and Fig. 7 [16–19], due to the aging population and improved medical care in developing countries [16].

Commercially available hip implants have a limited lifespan and often require revision surgery, typically 15–20 years after the initial procedure [15]. Considering the statistics of THA procedures, the complications discussed earlier, the younger age of surgical candidates, and increasing life expectancy, it is predictable that the number of revision surgeries will also rise. Studies projecting the number of revision total hip arthroplasties in Germany [17] and in the United States of America [133] suggest that this procedure number could increase by 43 to 70% since 2020, represented in Fig. 8.

Consequently, hip implants are continuously undergoing research and development efforts aimed at improving their longevity and reducing the likelihood of complications and revision surgery. Advances in manufacturing techniques,
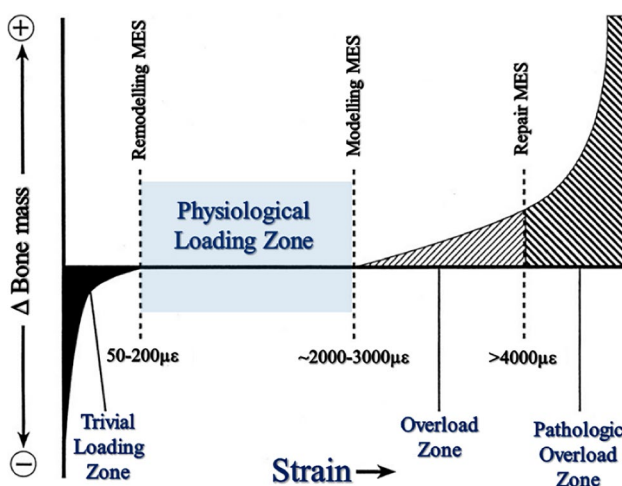
Fig. 4 Graphical illustration of the four mechanical usage zones of Frost's mechanostat theory (image adapted with permission from reference [265])

Fig. 5 Number of THA procedures performed per 100,000 habitants in the year 2019 (or the nearest year available) [16]
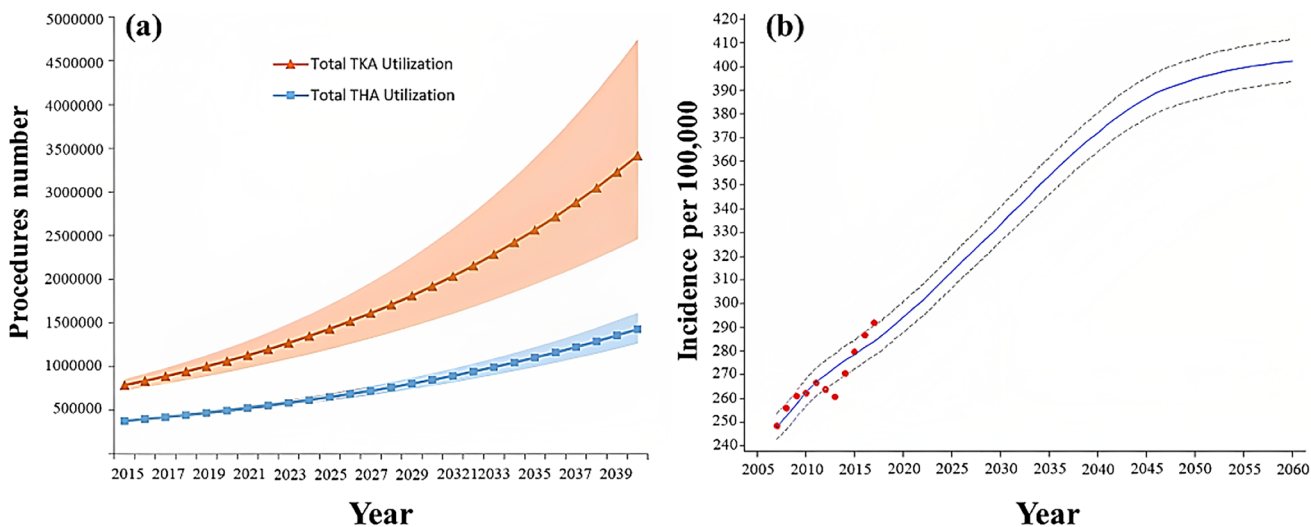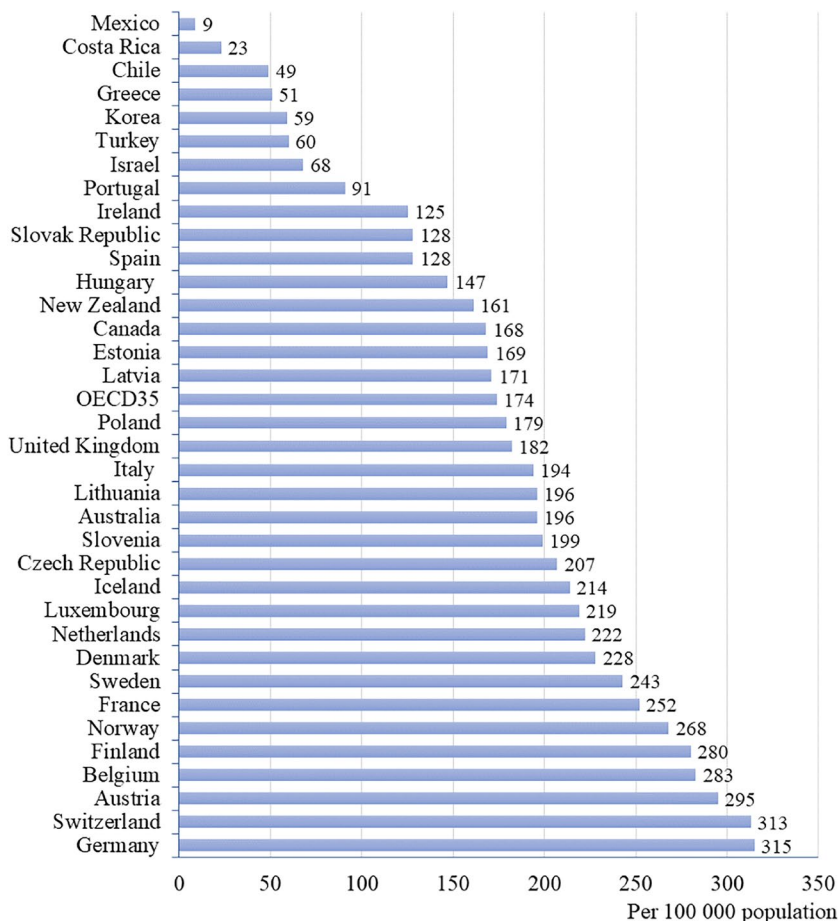
Fig. 6 (**a**) United States-projected annual THA procedures until 2040; (**b**) Germany-projected incidence of primary THA until 2060 (images redrawn and adapted from references [17, 19])

particularly AM, are being explored to create implants with lower Young's modulus and cellular structures. The goal is to design implants that closely mimic bone anatomy and behavior, thereby extending their lifespan. This approach addresses the primary cause of implant failure and ultimately leads to an improved quality of life for patients.

Fig. 7 United Kingdom-projected counts for THR until 2035 (image reproduced with permission from reference [18])
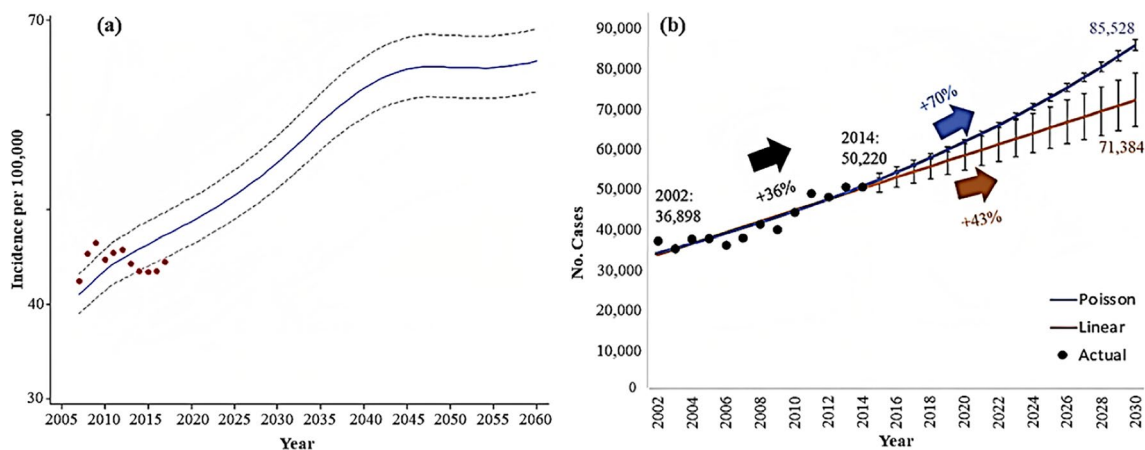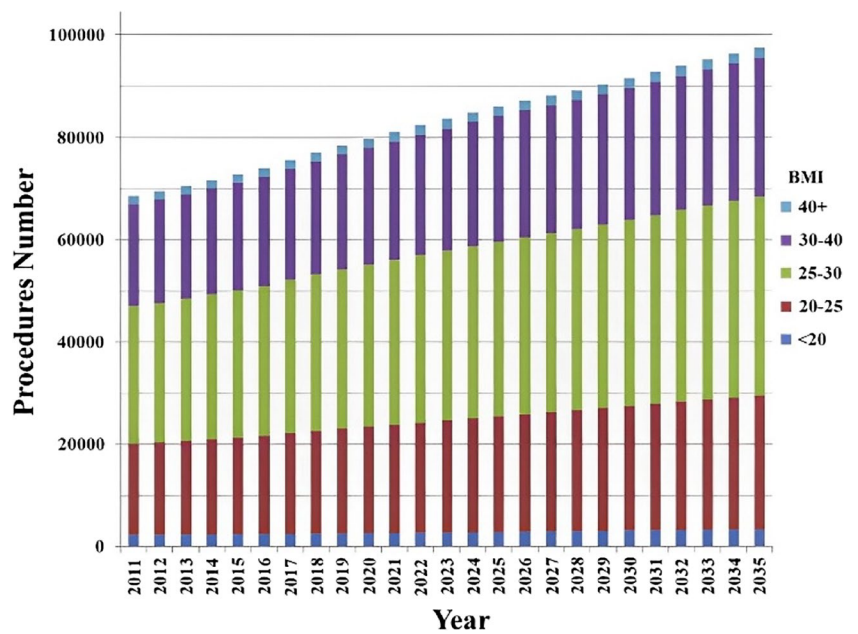
Fig. 8 (**a**) Germany-projected incidence of revision THA until 2060. (**b**) United States of America projections of revision THA to 2030 (images adapted from references [17, 133])

2.6 Preceding attempts: patents with cellular structures

The complications previously mentioned have been observed since the early attempts of prostheses implantation, and as the incidence of THA and revision THA has increased, researchers have focused on enhancing bone cell reactions to achieve better fixation and more favorable load distribution through the implant. From the outset, it has been believed that incorporating porous/cellular structures into implants would create a similarity to cancellous bone, promoting bone ingrowth within the pores. Tables 3 and 4 collect patents related to hip implants to assess the advancements made in integrating porous structures to enhance osteointegration.

Porous layers are typically applied to implants to create cellular structures, mainly in the external layers that meet the bone. Among the patents collected, the most common methods for obtaining these structures are coating processes [134–140], AM techniques [141–146], surface texturing [147–149], and some processes undefined or imperceptible [150–152]. Some patents provide ranges for the porosity percentage, which is known to enhance bone ingrowth.

Regarding the porosity of each implant, only three have a recommended porosity percentage: 40% [137], 45% [134], and 80% [140]. Other implants have a broader range of porosity, namely 20% [152], 30% [141], and 60% [142]. The porosity level will impact the structural strength, but this aspect is only considered in the US Patent No. 2021/0045880

Table 3 Patented structured or modified acetabular cups

Date	Patent No.	Features			Refs.
		Materials proposed	Structure/Modification	Schematic	
1991	US 5,004,476	CoCrMo	Porous coating		[134]
1996	EP 0 761 242 A1	Metal such as Ti	Porous coating		[135]
2003	EP 1 290 992 A1	Ti or Ti alloy OR Alu	Porous outer layer by surface finish or coating with HA coating		[136]
2006	EP 1 800 700 A2	Ti OR Ti alloys OR SS OR CoCr alloys OR Ta OR Nb	Lattice structure in the outer layer		[144]
2007	EP 1 820 475 A1	Ti OR Ti alloys OR SS OR CoCr alloys	Fully porous shell		[150]
2012	US 8,197,550 B2	SS OR Ti OR Ti alloys OR CoCr alloys OR other suitable metal alloys	Fully porous shell		[151]
2013	US 8,454,705 B2	Ti OR Ti6Al4V OR Co alloy	Lattice structured outer layer with the possibility of lattice structured internal layer		[143]
2015	US 2015/0012109 A1	Ti OR Ti alloy OR CoCr OR SS-based alloy	Lattice structured outer layer by SLS		[142]
2016	US 2016/0220376 A1	Nb OR Zr OR Ti OR Ta OR Co OR Mo OR Va OR Cr OR Al OR Mg OR combinations thereof OR Metal-based cermet OR Ceramic-based cermet OR Ceramic toughened by Zi OR Whisker OR Fibre	Fully porous shell		[141]
2022	US 2022/0039961	Imperceptible	Porous shell with protrusions		[145]

Table 4 Patented structured or modified femoral stems

Date	Patent No.	Features			Refs.
		Materials proposed	Structure/Modification	Schematic	
1967	US 3,314,420	Mixture of Alu, Sl, CaCO and MgCO	Porous surface		[152]
1983	US 4,406,023	Co-Cr alloy OR TiAlV alloy OR ceramic OR other suitable material	Surface texturized OR with a porous material		[147]
1985	US 4,514,865	CoCr alloy OR TiAlV alloy OR Ceramic OR other suitable material	Surface texturized or with a porous material		[148]
1987	US 4,644,942	Ti6Al4V with Copper or Iron OR other suitable metal alloys	Porous coating		[137]
1991	US 5,004,476	CoCrMo	Porous coating		[134]
1996	US 5,571,185	-	Porous coating (cover has an open-cell structure repeated)		[138]
2004	US 6,746,488 B1	-	Porous coating		[139]
2007	US 2007/0043446 A1	-	Roughened surface		[149]
2012	US 8,206,455 B2	Ta	Porous surface geometry		[140]
2021	US 2021/0095337 A1	Ti OR Ti alloys OR St OR CoCr OR Ta	Porous microstructure (at least by one lattice of cells)		[146]

A1 [146], where this feature is evaluated. E. Jones et al. [144] also proposed a porosity range but suggested an interesting characteristic, a gradient porosity. They attributed a lower porosity in the equatorial region of the shell compared to the polar region, creating a gradient from the inside to the outside of the shell, from the implant toward the bone.

Similarly, the inventors also consider different ranges of pore sizes. E. Jones et al. [144] and W. H. Harris [147, 148] recommend large intervals of 50 to 800 μm and 150 to 1000 μm, respectively, while Y. Li et al. [141] recommend a pore diameter range of 50 μm and 250 μm, which is smaller. However, these values cannot be directly compared as there is no description provided for each dimension, so it is uncertain if they correspond to the same parameter.

Likewise, a range of values is also recommended for layer thickness. E. Jones et al. [144] and P-E. Moreau et al. [142] mention thicknesses between 1000 and 2000 μm and 300 and 7000 μm, respectively. S. D. Cook [134] only suggests

values above 1000 μm. Additionally, the heights of the protrusions defined in the US Patent No. 2016/0220376 A1 [141] can be considered, as they represent the full thickness of the layer and vary from 50 to 2000 μm.

Among the selected patents, some stand out due to the presence of microstructures defined by lattice cells [143, 146] or meshes with nodes and struts [142]. However, Pressaco et al. [143] only mention that the cap is a lattice with open and intercommunicating cavities without providing specific dimensions or property values. On the other hand, P-E. Moreau et al. [142] state that the metallic outer layer consists of meshes defined by nodes and tapered struts rearranged with a uniform orientation. Each mesh has a parallelepiped shape with a rectangular base, preferably a cube shape. The recommended density is between 30 and 90%, and the thickness ranges from 300 to 7000 μm. These practical terms involve very wide ranges of values that will have implications for the mechanical behavior of the implant depending on the chosen dimension.

Conversely, Pasini et al. [146] provide a comprehensive explanation, beginning with the definition of the external surface, formed of porous microstructures, and at least one type of lattice cell. Each cell possesses a predetermined topology and multiple struts. The authors also selected a group of recommended cell topologies, including octet truss, tetrahedron, octahedron, body-centered cube (BCC), face-centered cube (FCC), rhombicuboctahedron, rhombic dodecahedron, or any combination of these and/or modified versions. Dimensions are mentioned, specifying that the struts should have a thickness ranging from 70 to 400 μm, with a corresponding pore size between 50 and 800 μm. The layer porosity is recommended to be between 30 and 80%, and the surface roughness falls within the range of 10 to 500 μm. What distinguishes this patent is the inclusion of experimental tests, which resulted in assigned structural strengths for specific porosity values. For instance, the porous microstructure demonstrated strengths greater than 190, 115, 100, and 60 MPa at porosities of 50%, 60%, 70%, and 75%, respectively. This information underscores the significance of this patent, as the results can represent a prediction of the mechanical behavior and longevity of the implant.

The main difference between the implant structures of each patent is the presence of a porous coating or fully porous shell, represented in Fig. 9. While the porous coating is a thin layer of material that contains interconnected pores or voids, usually applied on the surface of the structure, the fully porous shell is entirely porous throughout its entirety, based on unit cells or randomly distributed pores.

To establish connections between some patents featuring porous/cellular structures, both present and absent in Tables 3 and 4, and commercial hip implants, a survey was conducted. Although some patent applicants correspond to well-known brands such as Stryker [144], Biomet Manufacturing Corp. [153], now part of ZIMMER [139, 140, 150, 151, 154–156], SMITH&NEPHEW [145, 157], and DePuy Synthes [158], it was not possible to establish a direct connection between these patents and the currently available implants.

3 Additive manufacturing for hip implant fabrication

After the 3rd industrial revolution, mass production was achieved using electronics and technological information [159]. The most consumed or used products are manufactured using processes such as forming, injection moulding, casting, extrusion, stamping, and machining. Some of these processes are extensively used to produce prostheses or orthopedic implants [160, 161]. Each of these processes requires some form of tooling [162] and can result in material waste [163, 164]. For example, the machining process, especially when producing some complex geometries such as prostheses, can lead to significant waste. For this reason, achieving high levels of customization through conventional methods requires substantial economic [165, 166] and energetic costs [163]. The 4th industrial revolution, also known as Industry 4.0, follows the 3rd industrial revolution and is characterized by the integration of

Fig. 9 Difference between the porous layer and fully porous shell of the acetabular component (image adapted and redrawn from reference [266])
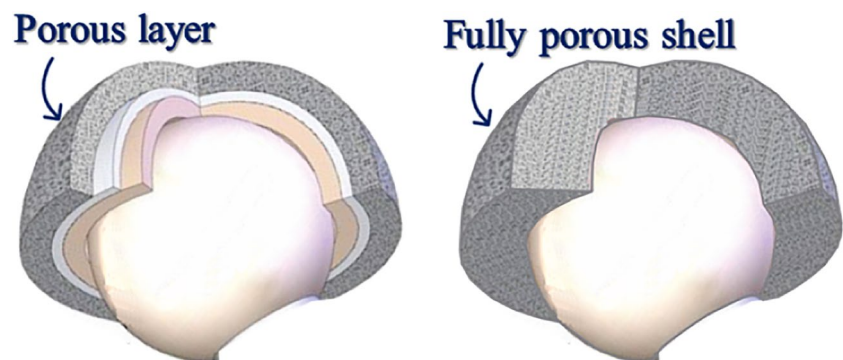
advanced technologies, such as 3D printing [159, 161], into current products and services. This integration aims to fulfill the customized requirements of consumers [161].

Additive manufacturing, commonly referred to as 3D printing, was initially developed in the 1980s through stereolithography technology. This technology involves solidifying thin layers of ultraviolet light-sensitive liquid polymer using a laser [160, 167]. The necessity for engineering structure optimization has emerged as a requisite for enhancing efficiency. AM enables the production of designs featuring topology optimization and cellular structures of unparalleled complexity, surpassing the limitations of conventional manufacturing methods. These capabilities extend to a wide range of materials such as polymers [168–170], ceramics [171, 172], metals [173, 174], and composites [175, 176]. The process is digitally controlled, utilizing a computer-aided design (CAD) model that is customized through software. The model is then printed layer by layer using AM equipment [177], and for that reason, since 2012, AM has been defined as "the process of joining materials to make objects from 3D model data, usually layer upon layer, as opposed to subtractive manufacturing methodologies"[178]. Commonly used AM methods include vat photopolymerization, material jetting, material extrusion, binder jetting, sheet lamination, direct energy deposition, and powder bed fusion [162, 179–183].

Additive Manufacturing is known for its precision, flexibility, customization, and versatility, allowing the fabrication of structures with intricate details, including cellular structures, while minimizing material impurities, unlike conventional manufacturing (CM) [164, 182, 184]. Cellular structures are currently undergoing thorough investigation to elucidate their mechanical and physical attributes [169], focusing on their integration into advanced applications such as biomedical [168, 176], aerospace [173], and automobile [185]. These structures have garnered substantial research attention due to their exceptional mechanical properties.

The appearance of AM technology has brought forth significant advancements and potential benefits for various industries. While it promises environmental advantages, including reduced energy consumption and efficient material usage throughout the supply chain [186], its implementation is not without challenges. Despite the technology's potential, there are drawbacks such as high costs, limited availability of necessary equipment outside academic institutions, and lengthy regulatory approval processes [186–188]. Furthermore, the current lack of long-term clinical data for 3D-printed implantable devices presents a challenge in evaluating their effectiveness and cost efficiency compared to traditional methods [187]. Nevertheless, it is crucial to highlight that the distinctive characteristics of cellular structures and implants require the utilization of AM techniques, currently the most viable means for their production. Besides, the continuous advancements and decreasing costs associated with 3D printing emphasize its growing influence and potential for substantial social and environmental transformation in diverse sectors.

3.1 AM potential for orthopedic

Powder bed fusion (PBF) is a preferred technique for producing biomedical applications, particularly prostheses or implants [166, 180, 189]. This technique involves importing CAD models into PBF software, which then slices the model into multiple layers [189]. Subsequently, successive layers of metal powder are deposited, corresponding to each slice of the model. Between the deposition of two consecutive powder layers, incising high energy, using the parameters previously defined, is sequentially applied, melting the layer selectively [161, 189]. PBF is divided into two techniques based on the energy source used: Electron Beam Melting (EBM), which utilizes an electron beam, and Laser Powder Bed Fusion (LPBF), which employs a high-power laser. Figure 10 illustrates both techniques. Additionally, these two techniques differ in terms of the printing environment, with

Fig. 10 Schematic representation of the PBF processes: (**a**) LPBF and (**b**) EBM (image adapted and redrawn from reference [162])
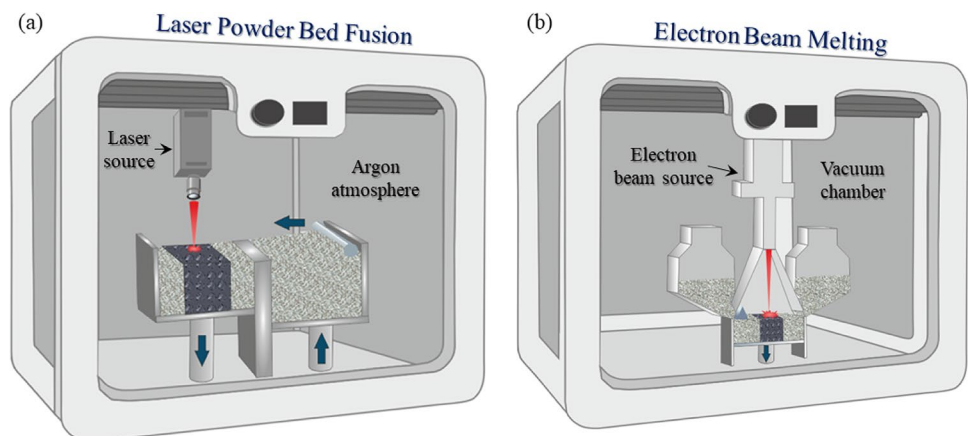
EBM being implemented in an inert gas chamber with a vacuum and LPBF in an argon or nitrogen environment [162, 180, 183, 190, 191].

Several parameters, such as the material used, equipment, and fabrication aspects, impact the final product quality [192, 193]. Key processing parameters that affect the quality of the fabricated product include layer thickness, laser/electron beam power, scanning speed and hatching space, scanning strategy, spot size, and platform pre-heating temperature [191]. While it is possible to adapt these parameters to attain the desired outcome, the complete resolution of both techniques remains a challenge. In the case of LPBF, major limitations include the time-consuming process, difficulty in scaling up for larger sizes, surface roughness, and high residual stress in the product, which is more pronounced compared to structures produced by EBM [191, 194]. Due to these limitations, the obtained products, especially in micrometric scales, may exhibit differences in porosity between the designed and measured values [22, 195–198]. Furthermore, within LPBF structures, the presence of supports is usually necessary to ensure efficient printing. Nonetheless, the production of these support structures, alongside the intended part, entails the consumption of valuable resources, specifically powder material and energy. Consequently, the production of support structures exerts a detrimental influence on both build time and cost [199].

Dense Ti6Al4V is still widely used as material for hip implants, resulting in an excessively high Young's modulus (YM) of approximately 110 GPa. When comparing this value with Young's modulus of cortical human bone, which ranges from approximately 10 to 30 GPa [182, 200], it becomes evident that current solutions are inadequate and lack development in achieving a closer mimicry of the mechanical behavior of human bone. Efforts to reduce the YM of implants are aimed at approaching the values of cortical human bone while preserving vital properties such as biocompatibility, biofunctionality, yield strength (YS), corrosion and wear resistance, and fatigue strength [190]. For this reason, a potential strategy involves creating metallic cellular structures with controlled porosity and shape using AM, thereby reducing the YM while maintaining implant strength [201, 202]. However, even though AM is the preferred method for producing cellular structures,

careful consideration must be given to all its parameters. For instance, the presence of residual stresses can lead to distortion, cracking, and delamination, potentially causing destructive effects on these structures. Therefore, optimization of process parameters is crucial to enhance the performance of the produced structures [191] and to assure that the sub-millimetric structures do not deviate significantly from the design of the CAD model [21, 22].

3.2 Cellular structures targeting orthopedic implants

Metallic biomaterials such as stainless steel, CoCr alloys, and Ti6Al4V have been extensively used as orthopedic biomaterials due to their exceptional mechanical and biological performance [22]. Among these materials, Ti6Al4V alloy is particularly emphasized due to its high strength-to-weight ratio, good biocompatibility, superior corrosion resistance, and lower Young's modulus compared to the aforementioned alloys [21]. Young's modulus is a critical parameter related to the mechanical performance of metallic implants [22]. In the case of the Ti6Al4V alloy, it tends to be approximately 110 GPa, significantly higher than the YM of human cortical and trabecular bone, which ranges from approximately 10 to 30 GPa and 0.8 to 5 GPa, respectively [21–24].

To bridge these differences, studies have been conducted on the development of cellular structures with customized properties that can exhibit mechanical behavior closer to that of bone.

Three-dimensional cellular structures are typically characterized by having high porosity. Typically, their main classification is based on the arrangement of their unit cells, such as stochastic (random) and non-stochastic (periodic) structures. Moreover, these structures can be subdivided into closed-cell and open-cell configurations based on pore interconnectivity [203, 204]. In other words, open-cell structures feature interconnected pores forming a porous network, while closed-cell structures contain isolated pores separated by plates; see Fig. 11. Stochastic cell structures, such as metallic and non-metallic foams, resemble the structure of sponges. Conversely, non-stochastic structures, referred to as periodic or lattice structures, involve the repeated arrangement of unit cells in a specific shape [204]. Both types

Fig. 11 Cellular structures characterization (image reproduced with permission from reference [204])
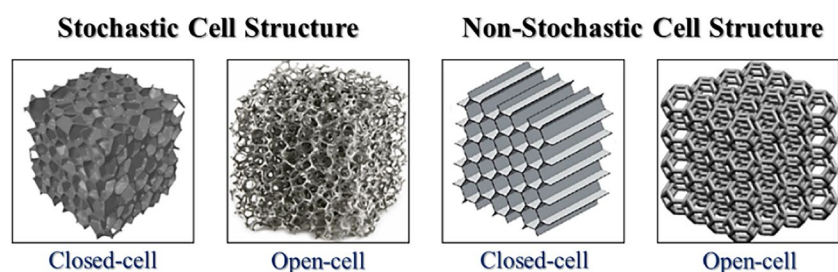
demonstrate notably lower weight than solid materials of equivalent volume.

An extensive range of cellular structures is addressed with unit cells including auxetic, body-centered, circle intersection, cubic, cuboctahedron truncated, diamond, dodecahedron, edge-centered, cube, face-centered, helix, honeycomb, Kelvin, octet, octahedron, rhombic dodecahedron, spider-web, tetrahedron, trabecular, triple periodic minimal surface gyroid, and triply arranged octagonal rings. These structures exhibit diverse characteristics, from negative Poisson's ratios to intricate geometries. Table 5 displays these features alongside the corresponding produced scaffolds. For example, the utilization of auxetic structures is justified by their ability to exhibit a negative Poisson's ratio under compressive and tensile loading conditions. This property results in higher shear modulus, indentation resistance, and fracture roughness, which are highly relevant characteristics for implant production [205–207]. However, none of the studies selected justified the chosen unit cell possessing different ones among each other, except for Bari et al. [208] and Liang et al. [209], who justified their use by mimicking the morphological shape of bone with bone-like structures.

Cellular structures possess the capacity to minimize weight, enhance relative strength, and improve stiffness through optimal material utilization [210]. These critical attributes play a vital role in the development of materials and structures intended for orthopedic applications. Consequently, several researchers primarily concentrated on assessing the impact of pore size and porosity on the mechanical and/or biological performance of scaffolds. The influence of using different unit cells was evaluated by a limited number of authors [197, 211–221]. The subsequent sections in this review discuss the mechanical behaviors of these scaffolds when composed of titanium or titanium-based alloys. To the authors' best knowledge, hip implants comprising lattice sections are commonly manufactured using titanium alloys, and it is known that implants made of pure titanium, titanium-based alloys, stainless steel, and cobalt-based alloys have demonstrated chemical and biological compatibility [164, 221–223]. Therefore, cellular structures and scaffolds composed of these materials were selected to evaluate the biological influence of lattice type and porosity.

3.2.1 Mechanical behavior

To assess the mechanical performance of cellular structures produced by LPBF or EBM, various tests were conducted, including compressive [22, 195–198, 205–209, 211, 214, 215, 217, 219, 232, 233], fatigue [195, 198, 233], and tensile [197] behavior evaluations.

Among the commonly assessed results in these studies, particular focus was given to Young's modulus and compressive/yield strength. In cases where fatigue behavior was evaluated, the studies focused on fatigue strength and the number of cycles until failure.

As previously mentioned, the primary goal of these scaffolds is to mimic the bone behavior as closely as possible. Some studies aim to replicate the behavior of cortical bone [22, 195–198, 205–208, 211, 214, 215, 217, 219, 232, 233], while others focus on trabecular bone [209, 221]. For that reason, the initial assessment typically involves determining Young's modulus, as it represents the key distinguishing property between hip implants and bone, with significant implications for implant longevity. However, there is no consensus among the selected studies regarding Young's modulus of cortical bone, with reported values ranging from 3 to 20 GPa [201], 3 to 30 GPa [208], 5 to 23 GPa [209], or 10 to 30 GPa [22, 196]. Similarly, the reported Young's modulus of trabecular bone varies, with some authors suggesting a range of 0.02 to 0.5 GPa [208], approximately 0.4 GPa [201], or 2 GPa [196]. Consequently, when analyzing the mechanical results of cellular structures in this chapter, the ideal range for cortical and trabecular Young's modulus is from the lower value to the higher value, namely 2 to 30 GPa and 0.02 to 2 GPa, respectively.

The focus is tailoring the type and dimensions of unit cells to achieve a lower Young's modulus, where all the studies achieved positive results. The evaluated scaffold's mechanical behavior involved various unit cell types, ranging from auxetic [219] to truncated cuboctahedron [211] (Table 6), and their dimensions were tailored based on the scaffold's pore size, porosity, and strut size (wall thickness), which are interdependent. The customization of these scaffold individual characteristics expresses their influence on the mechanical behavior. However, it is essential to evaluate their combined influence simultaneously.

Young's modulus Some studies have demonstrated that increasing porosity leads to a decrease in Young's modulus in structures with the same unit cell, which aligns with expectations. Almost every unit cell within the same study experienced this trend. Eldesousky et al. [219], Onal et al. [201], and Wally et al. [217] were the only exceptions. Eldesousky et al. [219] report a discrepancy in the behavior of auxetic cubic samples, specifically noting that a structure with approximately 84% porosity displays a higher Young's modulus compared to another sample with a nearly identical porosity level of approximately 83%. Although the authors do not offer an explicit explanation for this observation, it can be proposed that the slight difference between porosity and Young's modulus is of such minimal significance that it can likely be attributed to minor imperfections in the samples. The body-centered cubic cell behavior observed by Onal et al. [201] can be understood through the existence of a gradient structure, which does not uniformly bestow

Table 5 Cellular structures produced by LPBF or EBM and their unit cells (not provided as N.p.)

Cell Unit	Design/CAD Figures	Structures produced	Refs.
Auxetic			[206, 207, 219, 224]
Body-Centred			[197, 201, 221]
Circle intersection		N.p.	[24]
Cubic		N.p. N.p. N.p.	[24, 164, 195, 196, 208, 211, 213, 215, 221, 225-231]
Cuboctahedron Truncated			[211]
Diamond		N.p.	[197, 211, 215, 217, 218]
Dodecahedron	N.p.		[232]
Edge-centred cube			[227]
Face-centred		N.p.	[220, 222, 223, 227]
Helix		N.p.	[24]
Honeycomb			[218]
Kelvin		N.p.	[212]
Octet			[227]
Octahedron		N.p.	[214, 216]
Rhombic dodecahedron		N.p.	[220]
Spider-web			[217]
Tetrahedron		N.p.	[214, 216]
Trabecular			[209, 221]
Triple periodic minimal surface gyroid			[213]
Triply Arranged Octagonal Rings		N.p.	[212]
Others	N.p.	N.p.	[229, 233, 234]

Table 6 Cellular structures with different unit cell types produced by different AM technologies and their mechanical properties (obtained from compressive tests)

Unit cell	A.M	Samples' differences (same study)	Material	Porosity (%)	Y.M. (GPa)	Y. S. (MPa)	U.C.S. (MPa)	Refs
Auxetic cubic	EBM	Porosity and pore size (1500 μm)	Ti6Al4V	87.00[a]	0.20[b]	-	-	[219]
Auxetic cubic	EBM	Porosity and pore size (1500 μm)	Ti6Al4V	84.00[a]	0.35[b]	-	-	[219]
Auxetic cubic	EBM	Porosity and pore size (1250 μm)	Ti6Al4V	83.00[a]	0.25[b]	-	-	[219]
Auxetic cubic	EBM	Porosity and pore size (3800 μm)	Ti6Al4V	64.00[a]	4.90[b]	-	-	[219]
Auxetic cubic	EBM	Porosity and pore size (800 μm)	Ti6Al4V	58.00[a]	9.20[b]	-	-	[219]
Auxetic re-entrant	EBM	Porosity	Ti6Al4V	87.00[a]	0.05[b]	-	-	[219]
Auxetic re-entrant	EBM	Porosity	Ti6Al4V	82.00[a]	0.25[b]	-	-	[219]
Auxetic re-entrant	EBM	Porosity	Ti6Al4V	66.00[a]	1.00[b]	-	-	[219]
Auxetic re-entrant	EBM	Porosity	Ti6Al4V	63.00[a]	1.55[b]	-	-	[219]
Auxetic re-entrant	EBM	Porosity	Ti6Al4V	57.00[a]	2.40[b]	-	-	[219]
Body-centered cubic	LPBF	Unit cell and porosity	Ti6Al4V	90.16[a]	0.10	-	195.70	[197]
Body-centered cubic	LPBF	Porosity and strut size (400 μm)	Ti6Al4V	71.45±0.02	1.60±0.20	53.00±4.00	74.00±2.00	[201]
Body-centered cubic	LPBF	Porosity and strut size (600 μm)	Ti6Al4V	51.11±0.01	4.60±0.40	192.00±14.00	256.00±4.00	[201]
Body-centered cubic	LPBF	Strut size (400 μm) (gradient structure, dense-out)	Ti6Al4V	50.01±0.01	3.50±0.50	86.00±11.00	128.00±8.00	[201]
Body-centered cubic	LPBF	Strut size (610 μm) (gradient structure, dense-out)	Ti6Al4V	50.01±0.01	3.50±0.50	86.00±11.00	128.00±8.00	[201]
Body-centered cubic	LPBF	Strut size (820 μm) (gradient structure, dense-out)	Ti6Al4V	50.01±0.01	3.50±0.50	86.00±11.00	128.00±8.00	[201]
Body-centered cubic	LPBF	Strut size (400 μm) (gradient structure, dense-in)	Ti6Al4V	49.38±0.01	3.90±0.80	114.00±8.00	150.00±17.00	[201]
Body-centered cubic	LPBF	Strut size (610 μm) (gradient structure, dense-in)	Ti6Al4V	49.38±0.01	3.90±0.80	114.00±8.00	150.00±17.00	[201]
Body-centered cubic	LPBF	Strut size (820 μm) (gradient structure, dense-in)	Ti6Al4V	49.38±0.01	3.90±0.80	114.00±8.00	150.00±17.00	[201]
Body-centered cubic	LPBF	Porosity and strut size (800 μm)	Ti6Al4V	31.86±0.01	9.00±0.60	392.00±14.00	532.00±11.00	[201]
Bone-like	LPBF	Unit cell and porosity	Ti6Al4V ELI	74.00[a]	5.09	169.00	-	[208]
Bone-like	LPBF	Unit cell and porosity	Ti6Al4V ELI	61.00[a]	5.42	280.00	-	[208]
Bone-like	LPBF	Unit cell and porosity	Ti6Al4V ELI	55.00[a]	6.07	343.00	-	[208]
Cubic	LPBF	Porosity and pore size (700 μm)	Commercial Ti	90	1.00±0.10	10.90±0.30	-	[231]
Cubic	LPBF	Unit cell	Ti6Al4V	87.00	-	29.90±0.90	30.20±0.90	[211]
Cubic	LPBF	Unit cell	Ti6Al4V	76.00	-	63.30±2.20	76.60±2.30	[211]
Cubic	LPBF	Pore size (1000 μm) and strut thickness (500 μm)	Ti6Al4V	73.00	0.71	-	58.00	[226]
Cubic	LPBF	Unit cell	Ti6Al4V	72.00	-	65.60±12.30	110.50±17.40	[211]
Cubic	LPBF	Pore size (400 μm)	Commercial Ti	70	2.80±0.20	31.00±1.00	-	[231]
Cubic	LPBF	Pore size (900 μm)	Commercial Ti	70	3.50±0.80	47.40±1.30	-	[231]

Table 6 (continued)

Unit cell	A.M	Samples' differences (same study)	Material	Porosity (%)	Y.M. (GPa)	Y. S. (MPa)	U.C.S. (MPa)	Refs
Cubic	LPBF	Porosity and pore size (700 μm)	Commercial Ti	70	3.90±0.10	45.10±2.40	-	[231]
Cubic	LPBF	Unit cell	Ti6Al4V	65.00±1.10	2.60±0.10	96.00±5.00	-	[215]
Cubic	LPBF	Unit cell	Ti6Al4V	63.00	-	112.60±7.20	184.80±3.60	[211]
Cubic	LPBF	Pore size (800 μm) and strut thickness (600 μm)	Ti6Al4V	61.00	0.83	-	84.00	[226]
Cubic	LPBF	Pore size (712.00±7.00 μm)	Ti6Al4V	60.50±0.20	4.30±0.60	227.00±4.60	-	[213]
Cubic	LPBF	Pore size (616.00±5.00 μm)	Ti6Al4V	51.40±0.30	8.30±0.80	348.70±7.50	-	[213]
Cubic	LPBF	Pore size (600 μm) and strut thickness (700 μm)	Ti6Al4V	45.00	1.12±0.20	-	119.00	[226]
Cubic	LPBF	Pore size (495.00±6.00 μm)	Ti6Al4V	41.80±0.40	12.80±0.60	464.70±11.30	-	[213]
Cubic	LPBF	Porosity and pore size (700 μm)	Commercial Ti	40	12.90±1.10	184.80±0.90	-	[231]
Cubic-like	LPBF	Pore size and distance between pores	Ti6Al4V	73.30±0.72	19.00[b]	-	-	[196]
Cubic-like	LPBF	Unit cell	Ti6Al4V	64.80±1.20	1.80±0.50	49.00±2.00	-	[215]
Cubic-like	LPBF	Pore size and distance between pores	Ti6Al4V	62.00±0.55	28.00[b]	-	-	[196]
Cubic-like	LPBF	Pore size and distance between pores	Ti6Al4V	37.90±0.44	50.00[b]	-	-	[196]
Cubic-like	LPBF	Pore size and distance between pores	Ti6Al4V	32.40±0.01	65.00[b]	-	-	[196]
Cubic-like	LPBF	Pore size and distance between pores	Ti6Al4V	25.4±0.24	77.00[b]	-	-	[196]
Cubic-like	LPBF	Pore size and distance between pores	Ti6Al4V	19.90±0.14	95.00[b]	-	-	[196]
Diamond	LPBF	Unit cell and porosity	Ti6Al4V	90.27[a]	0.14	-	330.40	[197]
Diamond	LPBF	Unit cell	Ti6Al4V ELI	89.00	-	6.80±2.30	15.10±0.30	[211]
Diamond	LPBF	Unit cell and strut thickness (314.00±21.00 μm)	Ti6Al4V	82.90±0.70	0.70±0.20	16.00±4.00	-	[217]
Diamond	LPBF	Unit cell and strut thickness (333.00±22.00 μm)	Ti6Al4V	80.90±0.60	2.00±0.30	55.00±4.00	-	[217]
Diamond	LPBF	Unit cell	Ti6Al4V ELI	79.00	-	28.90±6.20	46.52±2.50	[211]
Diamond	LPBF	Unit cell and strut thickness (302.00±19.00 μm /433.00±20.00 μm)	Ti6Al4V	78.50±0.40	1.70±0.20	48.00±1.00	-	[217]
Diamond	LPBF	Unit cell	Ti6Al4V ELI	72.00	-	31.70±13.00	57.00±12.80	[211]
Diamond	LPBF	Struts side length through the layers: inner (200 μm), middle (300 μm), and outer (400 μm)	Ti6Al4V	66.82	4.72±0.03	126.81±3.88	170.53±2.36	[218]
Diamond	LPBF	Unit cell	Ti6Al4V	64.80±1.20	2.10±0.80	106.00±6.00	-	[215]
Diamond	LPBF	Unit cell	Ti6Al4V ELI	64.00	-	70.60±7.00	113.00±17.30	[211]
Diamond	LPBF	Unit cell and strut thickness (421.00±28.00 μm)	Ti6Al4V	56.90±1.00	3.30±0.60	147.00±10.00	-	[217]

Table 6 (continued)

Unit cell	A.M	Samples' differences (same study)	Material	Porosity (%)	Y.M. (GPa)	Y. S. (MPa)	U.C.S. (MPa)	Refs
Diamond	LPBF	Unit cell and strut thickness (414.00±23.00 μm/315.00±27.00 μm)	Ti6Al4V	56.70±0.80	3.40±0.40	147.00±31.00	-	[217]
Diamond	LPBF	Unit cell and strut thickness (412.00±22.00 μm)	Ti6Al4V	51.50±0.40	4.10±0.30	178.00±10.00	-	[217]
Diamond	LPBF	Struts sizes trough the layers: inner (200 μm), middle (300 μm), and outer (400 μm), and presence of supports	Ti6Al4V	51.37	10.07±0.09	350.09±3.27	419.81±11.64	[218]
Diamond	LPBF	Unit cell and strut thickness (422.00±11.00 μm)	Ti6Al4V	48.60±1.10	4.80±0.60	204.00±33.00	-	[217]
Dodecahedron	LPBF	Strut (120 μm) and pore size (500 μm)	Ti6Al4V ELI	84.22	0.55±0.07	15.80±1.20	19.40±0.30	[232]
Dodecahedron	LPBF	Strut (170 μm) and pore size (500 μm)	Ti6Al4V ELI	77.68	1.40±0.03	34.80±3.40	42.80±3.50	[232]
Dodecahedron	LPBF	Strut (170 μm) and pore size (450 μm)	Ti6Al4V ELI	71.20	2.62±0.02	67.80±3.00	78.70±2.20	[232]
Dodecahedron	LPBF	Strut (230 μm) and pore size (500 μm)	Ti6Al4V ELI	68.45	3.49±0.02	91.80±2.70	117.20±1.10	[232]
Honeycomb	LPBF	Struts sizes trough the layers: inner (200 μm), middle (300 μm), and outer (400 μm)	Ti6Al4V	67.05	3.79±0.07	110.85±4.07	162.96±6.29	[218]
Honeycomb	LPBF	Struts sizes trough the layers: inner (200 μm), middle (300 μm), and outer (400 μm), and presence of supports	Ti6Al4V	52.67	10.99±0.57	423.82±8.83	536.90±8.66	[218]
Kelvin	EBM	Unit cell width (4200 μm) and porosity	Ti6Al4V ELI	95.00	0.05	2.00	1.00	[212]
Kelvin	EBM	Unit cell width (2800 μm) and porosity	Ti6Al4V ELI	90.00	0.33	12.30	6.30	[212]
Kelvin	EBM	Unit cell width (1900 μm) and porosity	Ti6Al4V ELI	80.00	3.90	46.40	37.30	[212]
Octahedron	LPBF	Unit cell and pore size (1000 μm)	Ti6Al4V	77.01	2.57±0.21	81.16±3.31	-	[216]
Octahedron	LPBF	Unit cell and pore size (500 μm)	Ti6Al4V	62.87	5.51±0.24	228.42±1.17	-	[216]
Octet	LPBF	Pore size (280.00±6.00 μm)	Ti6Al4V	60.70±0.10	6.40±0.20	366.30±7.40	-	[213]
Octet	LPBF	Pore size (226.00±3.00 μm)	Ti6Al4V	51.40±0.20	10.40±0.30	494.00±9.50	-	[213]
Octet	LPBF	Pore size (196.00±4.00 μm)	Ti6Al4V	41.20±0.40	16.50±0.50	635.70±16.50	-	[213]
Octet truss	LPBF	Unit cell and porosity	Ti6Al4V	75.00[c]	1.20±0.40	34.00±11.00	39.00±3.00	[214]
Octet truss	LPBF	Unit cell and porosity	Ti6Al4V	70.00[c]	1.40±0.20	31.00±2.00	31.00±2.00	[214]
Octet truss	LPBF	Unit cell and porosity	Ti6Al4V	60.00[c]	3.40±0.30	119.00±22.00	145.00±34.00	[214]
Octet truss	LPBF	Unit cell and porosity	Ti6Al4V	50.00[c]	4.60±0.20	172.00±8.00	228.00±10.00	[214]
Spider-web	LPBF	Unit cell, pore size, and strut thickness	Ti6Al4V	68.60±1.50	6.00±0.40	224.00±7.00	-	[217]

Table 6 (continued)

| Unit cell	A.M	Samples' differences (same study)	Material	Porosity (%)	Y.M. (GPa)	Y. S. (MPa)	U.C.S. (MPa)	Refs
Tetrahedron	LPBF	Unit cell and pore size (1000 μm)	Ti6Al4V	84.03	1.31 ± 0.04	31.78 ± 3.68	-	[216]
Tetrahedron	LPBF	Unit cell and porosity	Ti6Al4V	75.00[c]	1.90 ± 0.10	68.00 ± 3.00	68.00 ± 3.00	[214]
Tetrahedron	LPBF	Unit cell and porosity	Ti6Al4V	70.00[c]	2.90 ± 0.10	120.00 ± 4.00	120.00 ± 4.00	[214]
Tetrahedron	LPBF	Unit cell and pore size (500 μm)	Ti6Al4V	67.00	4.66 ± 0.04	135.58 ± 1.43	-	[216]
Tetrahedron	LPBF	Unit cell	Ti6Al4V	65.30 ± 1.10	4.40 ± 0.30	107.00 ± 3.00	-	[215]
Tetrahedron	LPBF	Unit cell and porosity	Ti6Al4V	60.00[c]	3.10 ± 0.40	136.00 ± 23.00	136.00 ± 23.00	[214]
Tetrahedron	LPBF	Unit cell and porosity	Ti6Al4V	50.00[c]	4.30 ± 0.10	219.00 ± 8.00	219.00 ± 8.00	[214]
Trabecular-like	LPBF	Pore size and irregularity (0.50)	Ti6Al4V ELI	74.28	1.93	44.90	-	[209]
Trabecular-like	LPBF	Pore size and irregularity (0.50)	Ti6Al4V ELI	63.95	3.22	123.00	-	[209]
Trabecular-like	LPBF	Pore size and irregularity (0.50)	Ti6Al4V ELI	63.51	3.50[b]	125.00[b]	-	[209]
Trabecular-like	LPBF	Pore size and irregularity (0.25)	Ti6Al4V ELI	62.65	3.57	105.80	-	[209]
Trabecular-like	LPBF	Pore size and irregularity (0.06)	Ti6Al4V ELI	61.49	3.92	158.00	-	[209]
Trabecular-like	LPBF	Pore size and irregularity (0.50)	Ti6Al4V ELI	48.83	5.24	237.50	-	[209]
Triple periodic minimal surface (TPMS) gyroid	LPBF	Pore size (572.00 ± 7.00 μm)	Ti6Al4V	61.20 ± 0.30	8.80 ± 0.60	476.30 ± 7.40	-	[213]
Triple periodic minimal surface gyroid	LPBF	Pore size (339.00 ± 4.00 μm)	Ti6Al4V	51.40 ± 0.30	15.30 ± 1.00	608.00 ± 9.50	-	[213]
Triple periodic minimal surface gyroid	LPBF	Pore size (172.00 ± 5.00 μm)	Ti6Al4V	42.20 ± 0.20	21.70 ± 0.50	762.70 ± 9.70	-	[213]
Triply arranged octagonal rings	EBM	Unit cell width (4200 μm) and porosity	Ti6Al4V ELI	95.00	0.11	4.50	2.80	[212]
Triply arranged octagonal rings	EBM	Unit cell width (2800 μm) and porosity	Ti6Al4V ELI	90.00	0.74	30.20	22.00	[212]
Triply arranged octagonal rings	EBM	Unit cell width (1900 μm) and porosity	Ti6Al4V ELI	80.00	10.56	131.10	114.80	[212]
Truncated cuboctahedron	LPBF	Unit cell	Ti6Al4V ELI	83.00	-	41.40 ± 2.00	55.50 ± 1.70	[211]
Truncated cuboctahedron	LPBF	Unit cell	Ti6Al4V ELI	80.00	-	49.90 ± 18.90	62.20 ± 10.40	[211]
Truncated cuboctahedron	LPBF	Unit cell	Ti6Al4V ELI	73.00	-	66.10 ± 4.00	94.80 ± 6.90	[211]
Truncated cuboctahedron	LPBF	Unit cell	Ti6Al4V ELI	64.00	-	110.10 ± 10.40	147.20 ± 3.70	[211]

[a]Value obtained through relative density

[b]Value identified through the graph presented

[c]Design value

A.M., additive manufacture; Y.M., Young's modulus; C.S., compressive strength; U.C.S., ultimate compressive strength

resistance throughout its entirety. The structure with nearly 51% porosity has a uniform porosity distribution, while the approximately 50% porosity structure exhibits a gradient porosity distribution, denser on the edges and gradually increasing inwards, as depicted in Fig. 12a. Notably, the latter structures, despite possessing an overall reduced porosity, exhibit regions characterized by diminutive struts and elevated porosity, thereby imparting a susceptibility to structural weakening. Similarly, Wally et al. [217] reported a higher Young's modulus within a diamond cell featuring
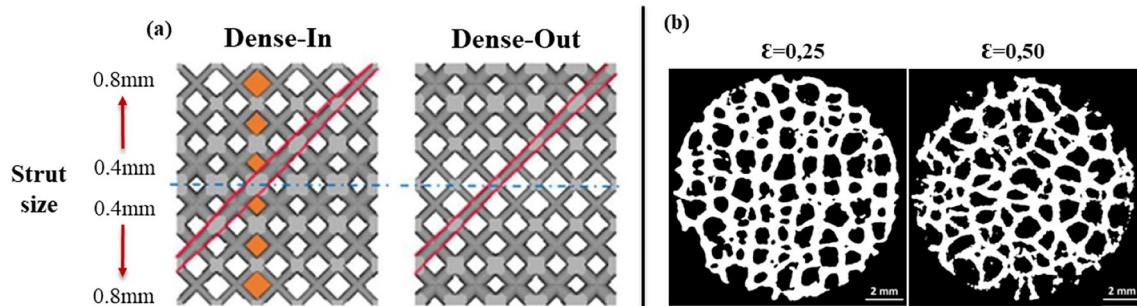
Fig. 12 (**a**) CAD model of the gradient BCC structure and (**b**) difference in the irregularity (ε) between samples of set 1 (images adapted from references [201, 209])

a higher porosity level, nearly 80%, as compared to a sample with approximately 78% porosity. This outcome can be attributed to the gradient structure inherent in the latter sample, represented in Fig. 12a, analogous to the observations made by Onal et al. [201], wherein certain regions are marked by diminutive struts and heightened porosity, consequently rendering the structure more susceptible to structural vulnerability. Despite this distinction, the authors of the study disregard this variation and assert that Young's modulus of both regular and graded scaffolds remains analogous among samples sharing the same design.

Concerning the identical unit cell discussed across various studies, a greater degree of disparity in outcomes becomes evident. Specifically, when comparing the cubic unit cell with 73% porosity, as presented by Dhiman et al. [226], with the cubic 90% porosity unit cell in Zhang et al. [231], a notable variance in Young's modulus is observed. Notably, despite the lower porosity in the former, one salient parameter deserving attention could be the considerably larger pore size. This variation in pore size may substantially influence structural resistance and contribute to the observed discrepancy. A parallel pattern is discerned in the remaining specimens documented by Dhiman et al. [226]. Each of these exhibits a marked decrease in Young's modulus when contrasted with those possessing approximately similar porosity levels. The cubic unit cell described by Deng et al. [215] exhibits a significantly diminished Young's modulus compared to the samples studied by Bartolomeu et al. [196]. This contrast can be assigned to discrepancies in the structural parameters, such as variations in strut and pore dimensions, powder characteristics, and inter-pore spacing.

The diamond unit cell stands as one of the extensively explored cellular structures. Nevertheless, it is noteworthy that among the studies conducted, only Xiong et al. [218] reported notably elevated values of Young's modulus compared to the collective findings. This deviation may be attributed to the functional grading of the samples, resulting in denser layers within the structure that confer enhanced structural resistance. Notably, the sample with approximately 51% porosity displays an augmented Young's modulus due to the presence of structural supports that confer substantially increased strength to the unit cell.

For the tetrahedron unit cell, both samples from Deng et al. [215] and Zhao et al. [216] with approximately 65% and 67%, respectively, exhibited a higher Young's modulus compared to the sample with 60% and 50% porosity from Arabnejad et al. [214]. Additionally, it must be highlighted that Deng et al. [215] approximately 65% of porosity samples have a lower Young modulus compared to Zhao et al. [216]. Both discrepancies are likely due to differences in strut and pore sizes.

Yield and ultimate compressive strength The general trend, just like the case of Young's modulus, is an increase in the yield strength and ultimate compressive strength as porosity decreases. In general, nearly every unit cell examined within the same study exhibited an enhancement in YS and UCS as porosity decreased. This effect can be justified by the high porosity, which is often associated with thin walls, requiring less force to collapse. Similar to Young's modulus, some studies challenge this statement. Onal et al. [201] body-centered cubic cells with approximately 51% porosity exhibited yield strength and ultimate compressive strength significantly higher than that of their samples with approximately 50%. This variation was detected during the evaluation of Young's modulus, supporting the hypothesis that structures with gradient designs, although displaying an overall reduced porosity, may contain regions with smaller struts and higher porosity. Consequently, this structural configuration makes them vulnerable to potential weakening.

Zhang et al. [231] presented cubic samples with 70% porosity, and their yield strengths exhibited slight variations among them. These observations align with Young's modulus findings for these samples. Notably, the sample characterized by a pore size of 900 μm displayed a higher yield strength compared to those with a pore size of 700 μm, in contrast to Young's modulus, where the former was lower

than the latter. While the authors did not provide an explicit explanation for this discrepancy, they did acknowledge that, overall, the values were quite similar, and these differences were deemed statistically insignificant.

The diamond cell with approximately 80% porosity obtained by Wally et al. [217] demonstrates a higher yield strength compared to the sample with 79% porosity, which is consistent with Young's modulus findings. As elucidated previously in the context of Young's modulus, this outcome can be assigned to the gradient structure. However, the authors do not further address this discrepancy.

Octet truss and tetrahedron cellular units from Arabnejad et al. [214] are worth analyzing. In this study, the parameter evaluated was the type of unit cell. The authors found that both samples followed the trend of strength increase with porosity decrease. Even though the octet truss unit cells with 75 and 70% porosity show, according to the authors, no increase in strength, respectively. The authors attribute this occurrence to the smaller average strut dimensions, as previous studies have indicated a dependency on strut thickness. It has been shown that structures with thinner struts tend to have lower strength, even when the porosity remains constant [235]. But, the main variation observed was the significant increase of the yield and ultimate compressive strength from the octet truss with 70 to 60% porosity and the tetrahedron with 75 to 70% porosity; see Table 6. The authors also concluded that the lower porosity octet truss is stronger than the tetrahedron, but with the increase of porosity, the tetrahedron roles are reversed. These major variations may be assigned to manufacturing defects that could potentially modify the deformation mechanism of the unit cells, with manufacturing limitations being more evident in the octet truss lattice.

The trabecular-like unit cell from Liang et al. [209] also shows a slight discrepancy between the samples with porosity of 62.65% and 63.52%. Interestingly, the yield strength exhibits a reduction from the condition of highest porosity to that of lowest porosity, in contrast to the initially anticipated trend. This behavior can be explained by the difference in irregularity between the samples (0.25 and 0.50, respectively), as shown in Fig. 12b, which significantly influences the distribution and size of the pores and ultimately affects the Yield strength.

When comparing structures from different studies, more significant variations can be observed. Even though Amin Yavari et al. [211] and Wally et al. [217] diamond cells follow the trend, the former demonstrates significantly lower yield strength compared to the latter despite having similar porosity levels. Within the same unit cell, Xiong et al. [218] is the study with the highest strength values comparing between samples with similar porosities, possibly due to the lower strut sizes and the presence of dense supports.

Regarding the tetrahedron unit cell, Deng et al. [215] exhibit an approximately 65% porosity sample with a yield strength lower than the 67% porosity sample from Zhao et al. [216]. These values are equivalent to the ones obtained for the Young's modulus of these samples. However, in the case of the sample with 60% porosity from Arabnejad et al. [214], the yield strength is not lower than the one from the previous studies.

Failure modes From all the assembled studies, only 5 evaluated and described their structures' failure modes. Eldesousky et al. [219] observed a layer-by-layer crushing on the struts, resulting in a shear plane at a 45° angle for the cubic samples. Similarly, Distefano et al. [212] reported the occurrence of macroscopic failure, characterized by the presence of an inclined shear plane inclined at a 45° angle, for all their specimens, meaning triply arranged octagonal rings (TAOR) and Kelvin unit cell. Despite observing the same failure model, the latter authors detected different fracture mechanisms, represented in Fig. 13. Specifically, they noted sliding as the primary mechanism for the TAOR cell and identified brittle fracture, often coinciding with a notch effect, in the Kelvin unit cell [212]. The scaffold H, a honeycomb-like unit cell from Xiong et al. [218], also presented a diagonal crush band inclined at a 45° angle.

There are structures that present layer-by-layer collapse along the applied force, such as the scaffold diamond-like (D) and Schwartz diamond-graded porous structures (SDGPS), from Xiong et al. [218] and Yang et al. [236], respectively. The behavior of the latter structures was
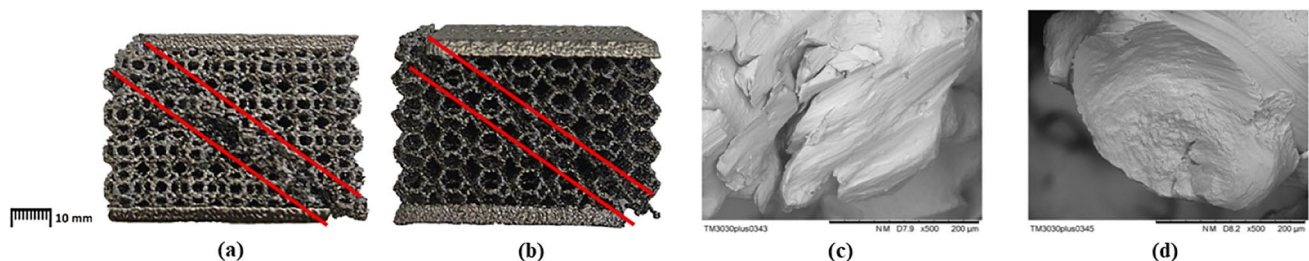

Fig. 13 Failure modes and fracture mechanism, respectively: (**a**, **c**) triply arranged octagonal rings (TAOR) and (**b**, **d**) Kelvin unit cell (images reproduced with permission from reference [212])

characterized by a predominant collapse occurring in the layer with the lowest volume fraction and thinnest struts since it is considered as the location with the highest degree of stress concentration. The collapse will occur layer by layer, one at a time, which the authors believe is quite distinct from the uniform porous structures [236]. Likewise, the re-entrant structures from Eldesousky et al. [219] present two failure modes already discussed: a layer-by-layer collapse, characterized by the vertical struts buckling, and the protrusion of vertical struts through the adjacent unit cells, as depicted in Fig. 14a.

Conversely, Wally et al. [217] documented different failure modes not based on the specific unit cell structures but rather on the density of the structure core. Structures without dense cores experienced a plastic lattice breakdown starting from the top and bottom sides, leading to structural collapse. On the other hand, core-base structures exhibited core buckling followed by lattice strut failure until structural collapse, as illustrated in Fig. 14b. Likewise, Xiong et al. [218] observed a deflection behavior of the scaffold diamond-like with support (DS) characterized by the formation of

a V-shaped shear band that propagated through the central region of the sample. The scaffold honeycomb-like unit cell with support (HS) exhibited a prominent distensible crack-oriented parallel to the compressive axis, extending across its lower portion. Notably, the deformation responses exhibited by scaffold H, scaffold DS, and scaffold HS closely resembled those observed in bulk metallic materials, which the authors believe is an indicator of the Functionally Graded Materials (FGM) structures' high toughness.

Fatigue behavior Concerning fatigue behavior, only three studies, namely Amin Yavari et al. [211, 232] and Zhao et al. [216], among those listed in Table 6, evaluated the fatigue performance of the samples. From Figs. 15 and 16, it becomes evident that the fatigue behavior is highly dependent on pore geometry and the resulting porosity. Zhao et al. [216] achieved this conclusion by demonstrating that scaffolds with a pore size of 500 µm exhibited superior fatigue properties compared to those with a pore size of 1000 µm. In addition to porosity, the type of unit cell also impacts the fatigue performance of the scaffolds, as those based on
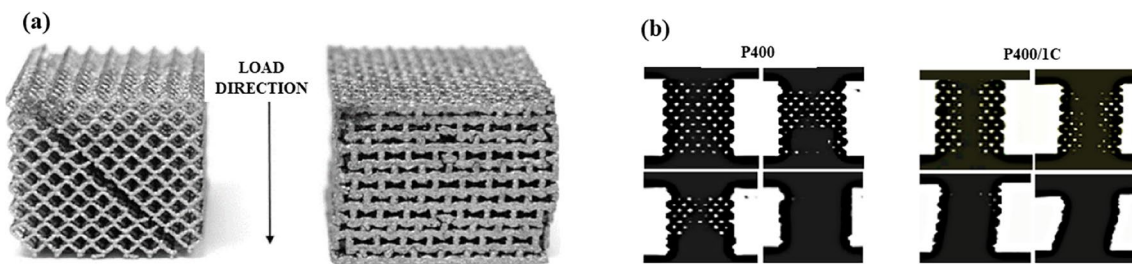
Fig. 14 (**a**) The failure mode of samples with small strut thickness, cubic (left), re-entrant (right). (**b**) The failure mode of the variable LPBF Ti6Al4V lattices; P400 and P400/1C, sequence: top left (before the test began), top right, bottom left, and bottom right (at the end of the test) (images reproduced with permission references [217, 219])
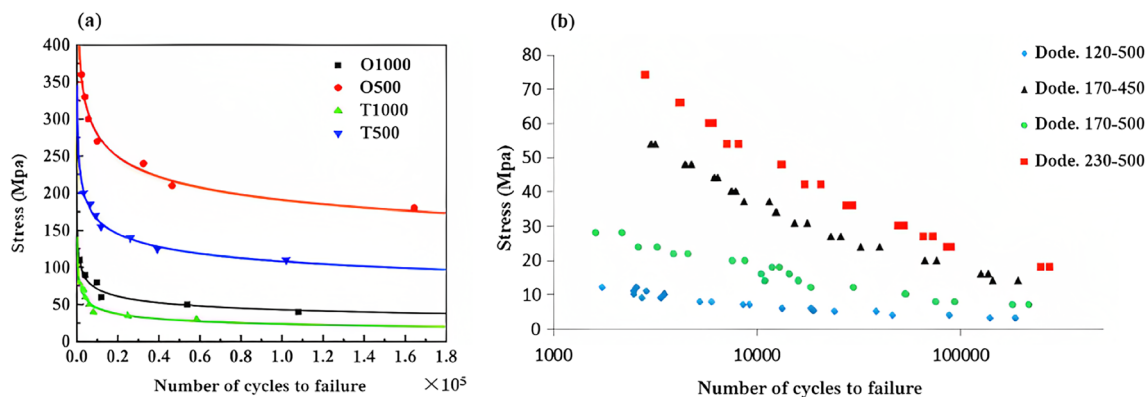

Fig. 15 S–N curves obtained by compression-compression fatigue testing of (**a**) octahedron and tetrahedron structures with 500 µm and 1000 µm of pore size. (**b**) Dodecahedron structures with 120 µm, 170 µm, and 230 µm strut sizes and 450 µm and 500 µm pore sizes (image reproduced with permission from references [216, 232])

Fig. 16 S–N curves obtained by compression-compression fatigue testing of (**a**) diamond structures with 64%, 72%, 79%, and 89% of porosity and (**b**) truncated cuboctahedron with 64%, 72%, 79%, and 89% of porosity (images reproduced with permission from reference [211])
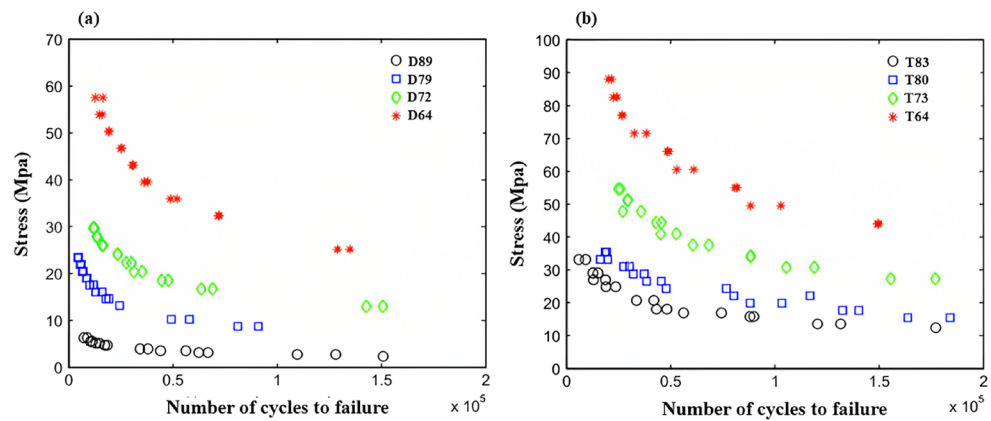
the octahedron unit cell demonstrated longer fatigue lives than those based on the tetrahedron unit cell. The authors attribute this to the stress distribution in the bearing struts and the effect of loading direction. Specifically, the compressive stress in each diagonal strut of the octahedron unit cell is lower than that of the tetrahedron unit cell, leading to improved fatigue behavior.

In Fig. 15b, besides pore size, the size of the struts also proves to be relevant. Among structures with the same pore size, the scaffold with a strut size of 230 µm exhibits the best fatigue behavior. Notably, this scaffold also has lower porosity in the Amin Yavari et al. study [232], emphasizing that both pore geometry and porosity significantly influence fatigue behavior. Figure 16a,b illustrates the fatigue behavior of diamond and truncated cuboctahedron lattices from the Amin Yavari et al. study [211]. The results indicate that the fatigue behavior of these scaffolds is highly dependent on both porosity and unit cell type. In both types of unit cells, higher porosities result in shorter fatigue lives for the same level of applied stress, as depicted in Fig. 16a,b. Although this figure only presents results from the diamond and truncated cuboctahedron lattices, the cubic lattice yields remarkable results as well. The authors believe that regardless of their porosity, these cellular structures do not fail under fatigue after 10^6 loading cycles, even when the maximum applied stress reaches 80% of their yield strength.

Based on the analysis of the previous information and the data provided in Table 6, a comparison was made between the mechanical behavior of the cortical and trabecular bone, which the researchers aim to achieve, and the mechanical performance obtained from each unit cell. Based on this comparison, structures with Young's modulus falling within the range of trabecular bone (0.02 to 2 GPa) and cortical bone (2 to 30 GPa) values were selected and depicted in a graph, as shown in Fig. 17. To the best of the authors' knowledge, these structures have the potential to mimic bone properties and mitigate current complications associated with arthroplasty.

3.2.2 Biological response

To evaluate the cytotoxicity and the ability of cells to grow and colonize, the samples were directly seeded with cell lines using established procedures [200, 209, 216, 217, 221, 223, 225, 228, 229, 234] or harvested directly from rats [231]. The cell lines employed vary among osteosarcoma [209, 229, 230], osteoblasts [201, 216, 217, 221, 223, 225, 237], periosteum-derived cells [234], fibroblasts [200, 228], and bone marrow-derived stem cells (BMSCs) [231].

Zhang et al. [231] and Xu et al. [237] conducted both in vitro and in vivo investigations, whereas Deng et al. [215], Arabnejad et al. [214], and Yu et al. [238] conducted extensive in vivo investigations utilizing different scaffold types. These scaffolds exhibited diverse cell structures, such as cubic, hollow hexagonal prism, hollow triangular prism, diamond, tetrahedron, cubic-like, tetrahedron, octet truss, and dodecahedral crystal. The studies involved implanting these structures in rats and rabbits and evaluating their osteointegration over specific intervals through a range of assessment techniques, including histological examination, micro-CT 3D reconstruction, scanning electron micrograph (SEM) analysis, X-ray examination, and push-out tests. These in vivo setups are illustrated in Fig. 18.

The biological response of bone growth is significantly influenced by various factors, including the porosity of structures determined by the size, number, and shape of pores, as well as surface energy closely associated with porosity. Additionally, the type of unit cell employed also contributes to this process. Despite their collective impact, the exact contribution of each factor is not yet clearly defined, resulting in ongoing debates within the field.

Permeability The permeability of cellular structures is closely associated with their porosity. High permeability is equivalent to high porosity and vice-versa, and it affects the efficiency of cell seeding. Impens et al. [239] proposed that high permeability reduces resistance to the cell suspension, resulting in higher fluid velocities that hinder cell attachment
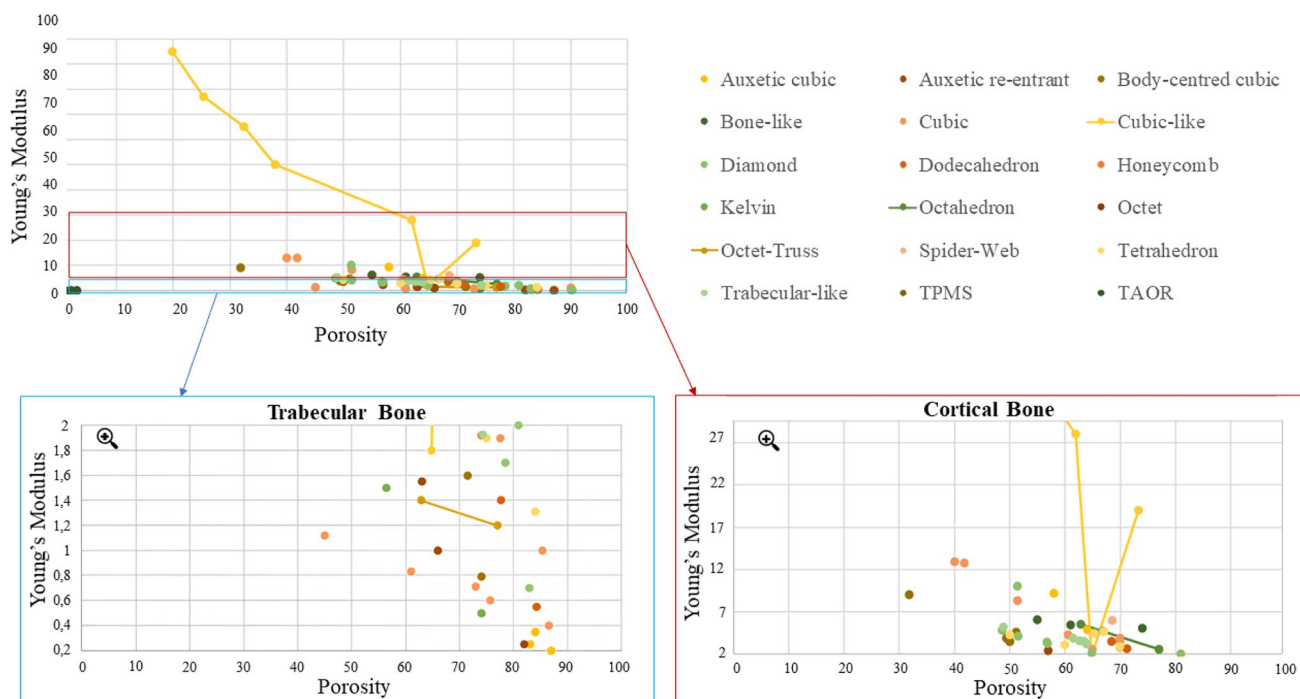
Fig. 17 Cellular structures with Young's modulus values capable of mimicking the trabecular and/or cortical bone (graphs derived from the data gathered in Table 6)

Fig. 18 Deng et al. [215] in vivo test setup starting with the exposure of the distal lateral condyle of the femur (**a**), then drilling a defect (5 mm in diameter and 8 mm in depth) from the lateral femoral condyle of the rabbit at low speed (**b**) and finally implanting a titanium scaffold into the bone defect (**c**). (**d**) Arabnejad et al. [214] in vivo test setup with scaffolds implantation in dogs healthy femurs (images reproduced with permission from [214, 215])
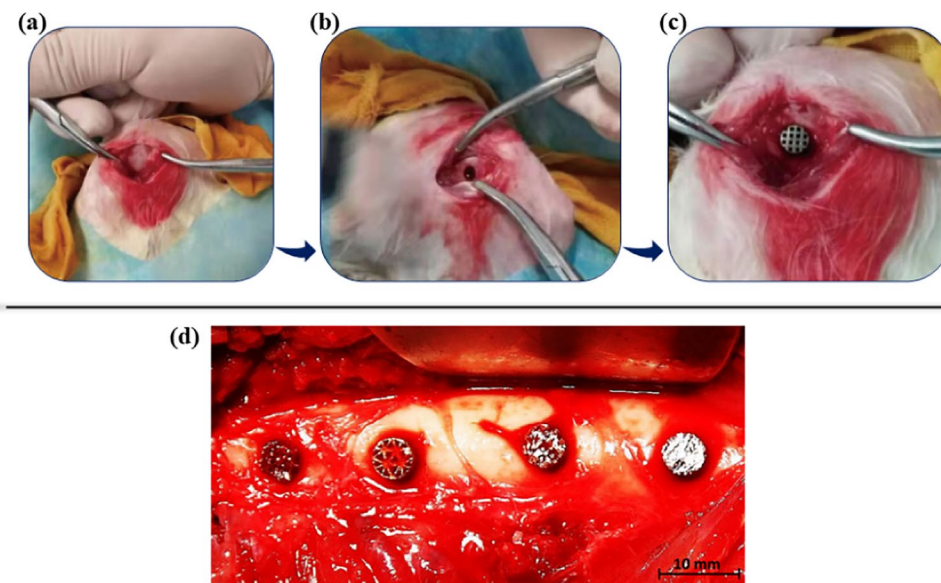
to the surface. This theory was confirmed by Van Bael et al. [234], who observed that lower permeability in the seeding direction increased the number of cells attached after 1 day of in vitro culture.

In contrast, Li et al. [223] demonstrated higher cell adhesion in the FBCCZ (face-centered cubic unit cell with longitudinal struts) unit cells, which had lower porosity compared

to the FCCZ (face and body-centered cubic unit cell with longitudinal struts). Although the cell viability was similar in both structures and comparable to the control, this highlights the excellent biocompatibility of these cellular structures, which could be attributed to the different unit cells. On the other hand, Zhao et al. [216] believe that structures with larger pores enable more cell adhesion, resulting in greater

bone ingrowth. This finding aligns with the conclusion of Liang et al. [209], who showed that among the three produced trabecular-like surfaces with the same irregularity but different porosities, the two with higher porosity promoted better osteoblast proliferation and differentiation.

Pore size and geometry influence Permeability is dependent on the pore size, which plays a crucial role in cell growth. It characterizes the mass transportation within the scaffold [209] and therefore affects the scaffold's ability to transport mass. Pore size is associated with the sustainability of cell viability and proliferation due to the passage of cell supplies, nutrient and oxygen supply, and metabolic waste release. Larger pores facilitate these processes more effectively [209]. Additionally, pore size can influence cell adhesion. In larger pores, cells attach to a single strut, while in smaller pores, they can attach to multiple struts [234]. This difference affects the stimuli experienced by the cells, leading to distinct biological responses in terms of attachment and proliferation.

Zhang et al. [231] found that scaffold characteristics, particularly a pore size of 700 μm and porosities between 70 and 90%, facilitated the highest cell viability. Interestingly, pores were observed transforming from rectangular to circular due to pore occlusion by corner bridging. Gene expression was highest with 70% porosity, while ALP activity peaked at 90% porosity. The in vivo results suggest that a pore size of 600–700 μm with 70–90% porosity fosters optimal bone defect repair. The authors believe that the increased pore size and subsequent higher permeability facilitated cell suspension and medium permeation within the scaffold. This allowed for ample space for cell growth and aggregation as well as enhanced blood vessel formation and oxygen supply, thereby promoting osteogenesis. Yu et al. [238] also observed that scaffolds with a porosity of 90% and a pore size of 650 μm enhanced the quantity, quality, and biomechanical properties of peri-implant bone with increasing healing time.

Figure 20f shows that triangular, hexagonal, and rectangular-shaped scaffolds with 500 μm pores exhibited higher occlusion rates, particularly the hexagonal pores, which show the highest level of occlusion. This can be attributed to pore geometry, as the authors observed that structures with obtuse-angled pores, such as hexagonal pores, tend to exhibit more occlusion compared to structures with acute-angled pores, such as triangular pores [234]. Xu et al. [237] found similar results when evaluating the biological performance of two different scaffold types with an overall porosity of 60%, a hollow hexagonal prism (group A) and a hollow triangular prism (group B) unit cell with ~ 50 μm pore sizes. The authors found that the surface area of group A scaffolds potentiates superior cell adhesion compared to

group B. This results from the reduced surface area on the underside of group B scaffolds, leading to increased cell adhesion within the scaffolds or at the orifice plate's base. Moreover, quantitative ALP staining results indicated the stronger bone differentiation promotion ability of group A scaffolds in comparison to group B. However, the authors assign the improved potential of the hexagonal prism unit structure in promoting bone differentiation and integration compared to the triangular prism unit structure to errors and spatial resolution. This may be due to the surface shape of the hexagonal prism unit structure closely resembling a circle and the included angle between the beams being circular, facilitating cell attachment and spreading. Furthermore, its larger surface area enhances cell adhesion and allows for increased acceptance of mechanical stimulation. On the other way, some authors believe that pores smaller than 100 μm are responsible for pore occlusion, as shown by Zhao et al. [216], where samples with pore sizes of 500 μm and 1000 μm did not exhibit occluded pores. For this reason, Van Bael et al. [234] advocate for graded scaffolds that combine small pores for initial cell attachment and larger non-circular pores to prevent pore occlusion. Similarly, Liang et al. [209] propose a graded porosity with a combination of small and large pores of varied shapes, as depicted in Fig. 19a. It is worth noting that although the graded structures have lower total porosities (48.83% and 63.51%), they achieved better viability and proliferation results, as shown in Fig. 19b.

In line with the findings of Van Bael et al. [234] and Liang et al. [209], Pagani et al. [225] conducted a preliminary evaluation and established that graded scaffolds exhibited improved biocompatibility results. However, they also demonstrated that both uniform and graded porosity scaffolds provided an environment suitable for osteoblast adhesion and proliferation. Figure 20a illustrates a predominantly regular distribution of cells, occasionally interrupted by small empty areas, over time, indicating good cell adhesion. Upon closer examination in Fig. 20, intricate organization of osteoblasts can be observed on the top surface (Fig. 20d) and around the pores (Fig. 20e). Although cell adhesion is primarily observed on the most superficial layer of the samples, a uniform layer of cells can be seen, attempting to fill the pores (Fig. 20b,c). These observations were further confirmed through SEM images, which revealed cells on the top surface and inside the pores. Consequently, a comparison of scaffolds with different porosities led to the conclusion that graded porosity scaffolds exhibited slightly more pronounced cellular colonization at deeper visible levels [225].

Surface energy impact The permeability of the structures is also influenced by the surface energy, which is another factor in cell adhesion. Cell binding shows a linear increase in surface hydrophilicity [200] which typically tends to increase
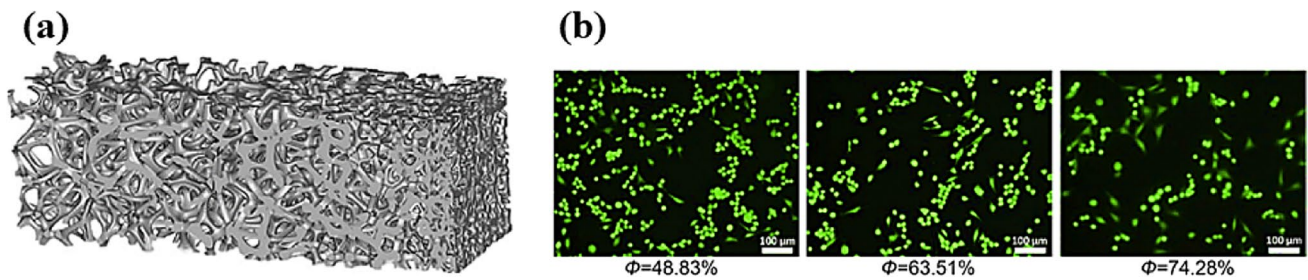
Fig. 19 On the left is (**a**) a trabecular-like cellular structure with porosity gradient, and on the right is (**b**) viability and proliferation of MG63 cells on porous Ti-6Al-4 V scaffolds with different porosities: fluorescence microscopy images after being cultured for 1 day (live cells appeared as bright green dots) (images reproduced with permission from reference [209])
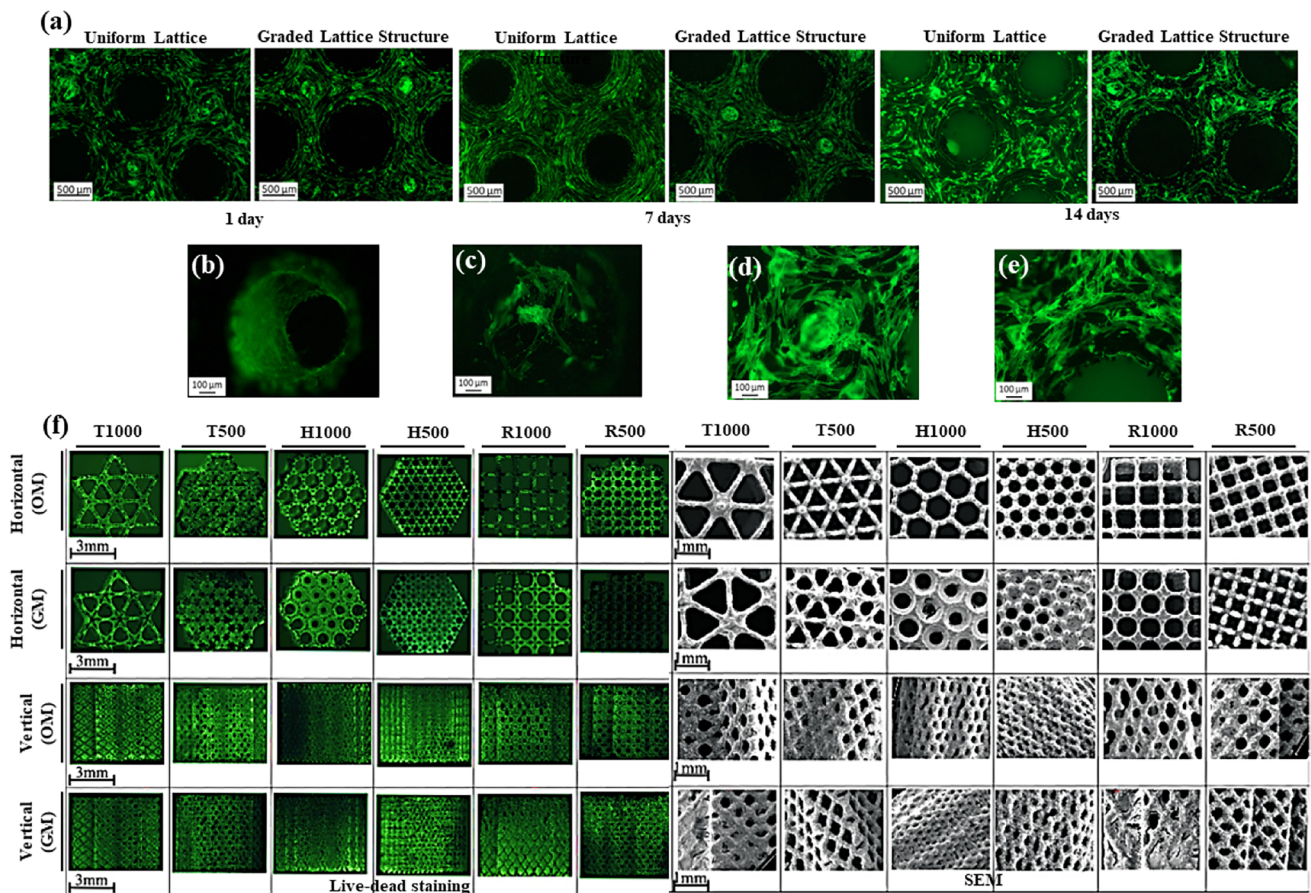

Fig. 20 Above are (**a**) images of normal human osteoblast cells (NHOst) labeled with fluorescein isothiocyanate, on scaffolds' surfaces at 1 day, 7 days, and 14 days after seeding with a magnification 4×and scalebar of 500 μm. In the middle are details of cell organization on both cellular structures: NHOst forming cell layer on a pore (**b**) and cell–cell connection inside a pore (**c**); dense NHOst culture on scaffold surface (**d**) and contouring a pore edge (**e**) with a magnification of 10×and a scale bar of 100 μm. Below are (**f**) representative images of live/dead staining and SEM images in the horizontal and vertical plane of human periosteum-derived cells on the six porous Ti6Al4V scaffold designs. The Ti6Al4V scaffolds were cultured for 14 days in an osteogenic medium or growth medium. Green fluorescence indicates living cells (image reproduction with permission from references [225, 234])

with porosity. In the study conducted by Costa et al. [200], wettability tests were performed, and it was concluded that all the produced cellular structures exhibited hydrophilic behavior. The authors were unable to measure the static contact angle between water or phosphate-buffered saline (PBS) and the lattice structure without bioactive material, as the drops quickly spread on the surface and throughout the specimen's porosity, as depicted in Fig. 21. Similarly,

Fig. 21 (**a**) Hydrophilic and (**b**) Super hydrophilic behavior of Ti6Al4V LPBF cellular structures, respectively (images reproduced with permission from references [200, 228])
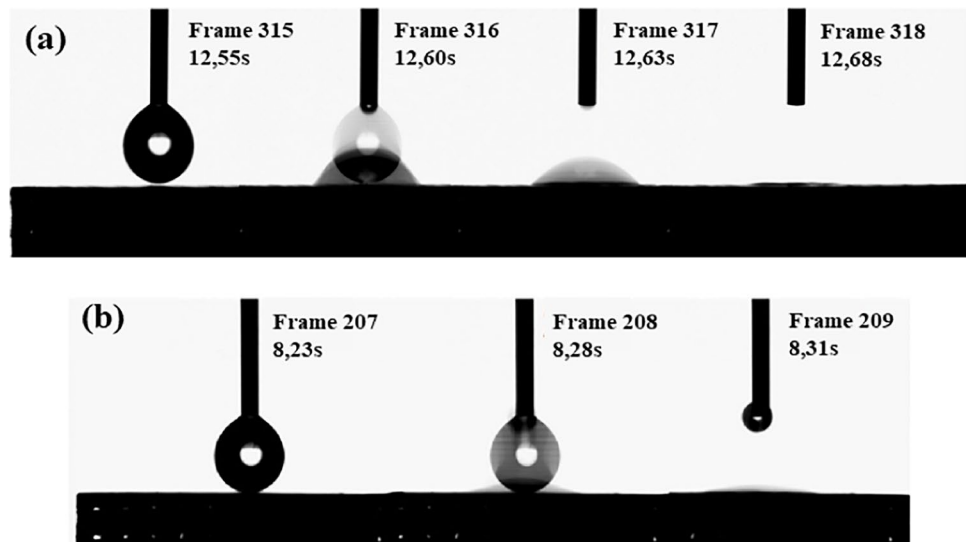
Melo-Fonseca et al. [228] conducted wettability tests using both water and a representative biological fluid, PBS. They reported that the lattice structure without any bioactive material exhibited hydrophilicity, as they were unable to determine the static contact angle. The spreading velocity of the drops was much higher compared to the study by Costa et a. [200], as shown in Fig. 21b, indicating a super hydrophilic behavior. Both of the studies [200, 228] attributed the hydrophilicity to the open-cell geometry and low surface roughness of the structures, emphasizing the importance of this property for biocompatibility. They defend that enhanced interaction between the implant and tissues can be achieved as a result [228].

Unit cell effect The type of unit cell also significantly influences cell growth. According to Zhao et al. [216], the octahedron unit cell was found to be more suitable for cell proliferation compared to the tetrahedron unit cell, considering that there were no differences in material and surface topography. The cell adhesion and migration showed the presence of pseudopodia. Pseudopodia, or protrusions, represented in Fig. 22, are organelles used by cells to extend their leading edge in various directions during cell migration [240, 241]. These membrane protrusions, including filopodia, among others [242], play a crucial role in communication with the extracellular matrix and other cells. The anchoring of cells on the surface of materials is highly relevant for cell adhesion. Therefore, the presence of pseudopodia on the structure surface indicates that cells are interacting with the substrate, suggesting a suitable surface for cell proliferation [216].

In the study conducted by Dallago et al. [229], where six different unit cell topologies were tested, it was concluded that the cubic structure is more suitable for bone ingrowth. Similarly, Costa et al. and Melo-Fonseca et al. [200, 228]
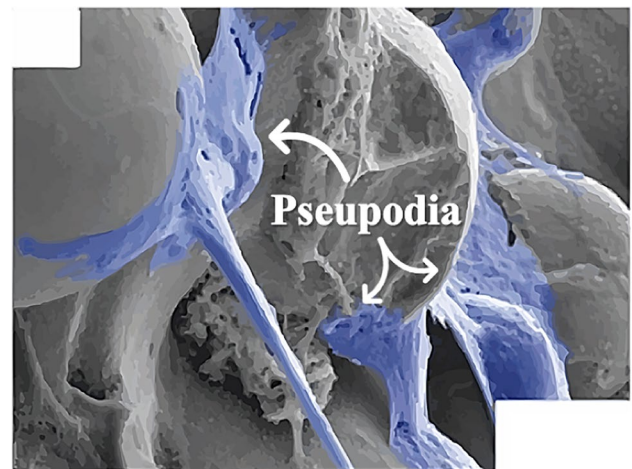
Fig. 22 Representation of pseudopodia in blue (adapted and redrawn from reference [216])

also employed cubic-like structures and found that these structures exhibited a hydrophilic behavior, promoting cell impregnation and proliferation. These studies not only evaluated the mechanical and biological performance of the cellular structures but also assessed their performance when impregnated with bioactive materials [200, 228].

Wally et al. [217] examined both a common unit cell, diamond structures with different pore sizes, and a non-common unit cell, the spider-web. They concluded that the pore size and shape did not significantly impact cell proliferation, and both diamond and spider-web structures supported cell viability and mineralization. Similarly, Xu et al. [237] evaluated the in vitro biocompatibility of scaffolds with different unit cells, a hollow hexagonal prism (group A) and a hollow triangular prism (group B), and concluded that there was no significant statistical difference in the proliferation

of the cells and that they showed good biocompatibility, good cell morphology, and no cytotoxicity. However, the in vivo findings suggest that the porous scaffold's hollow hexagonal prism structure was more effective in fostering bone differentiation and integration than the triangular prism structure. Besides, the in vivo tests showed that all scaffolds maintained their structural integrity post-implantation, with no evident inflammatory response or infection observed in the adjacent tissues.

In the study by Deng et al. [215], four structures with the same porosity and different unit cells were implanted in rabbits' femurs. Over time, it was observed that the amount of bone tissue within the pores of all scaffolds gradually increased, as shown in Fig. 23. Notably, this figure depicts the actual biological response of bone cells to the cellular structures, as this is one of the in vivo studies included in this article. The diamond lattice demonstrated the highest level of bone growth, while the cubic structure with circular pores exhibited the lowest bone growth. Furthermore, in terms of fluid flow simulation within the scaffold, the diamond lattice was found to be the most favorable. It exhibited the smallest internal fluid flow velocity difference, facilitating cell attachment to the surface. Additionally, it provided the longest fluid flow trajectory, enabling the transport of nutrients and oxygen to more areas of the scaffold. These factors contributed to increased bone growth [215].

3.2.3 Mechano-biological interplay

According to the literature, the mechano-biological performances of cellular structures are influenced by three main features: Young's modulus, p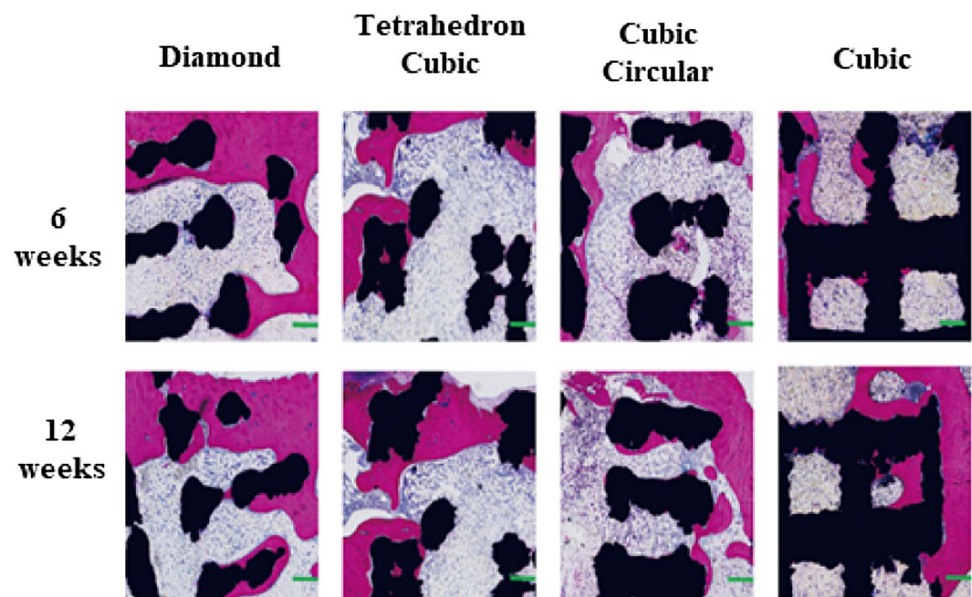orosity, and pore size. Young's modulus is considered suitable between 2 and 30GPa, taking natural bone properties as a reference [22, 196, 201, 208, 209]. Porosity is inversely proportional to Young's modulus and typically ranges between 30 and 80% for the mentioned modulus range. Additionally, pore size plays a crucial role in the biological response and the ability of cells to grow and proliferate. Structures with pore sizes ranging from 100 to 1000 μm are reported to enhance a better biological response by facilitating mass transportation within the scaffold and preventing pore occlusion [209, 216, 231, 234, 237].

In the author's opinion, the interplay between Young's modulus, porosity, and pore size defines the optimal domain of cellular structures that can be applied in orthopedic implants. To illustrate this, Fig. 24 provides an engineering tool showcasing various examples of different types of cellular structures within the mentioned optimal domain. These structures include the auxetic cubic and re-entrant [219], body-centered cubic [201], cubic [213, 231], cubic-like [196], diamond [217, 218], honeycomb [218], octahedron [216], octet [213], octet-truss [214], spider-web [217], tetrahedron [214, 216], and TPMS [213], as represented in Fig. 24.

4 Cases of study

At the frontline of modern manufacturing, Powder Bed Fusion has gathered considerable attention owing to its unparalleled precision, flexibility, and capacity to fabricate highly intricate and individually tailored structures, such as high complex cellular designs [164, 182, 184]. The development of hip implants incorporating cellular structures heavily relies on PBF's capability to minimize material

Fig. 23 Stained histological sections of dehydrated, embedded samples of the bone scaffolds obtained at 6 weeks and 12 weeks. Pink represents the bone tissue, and black represents the scaffold. Original magnification: 10.0; scale bar: 1 mm (image reproduced with permission from reference [215])
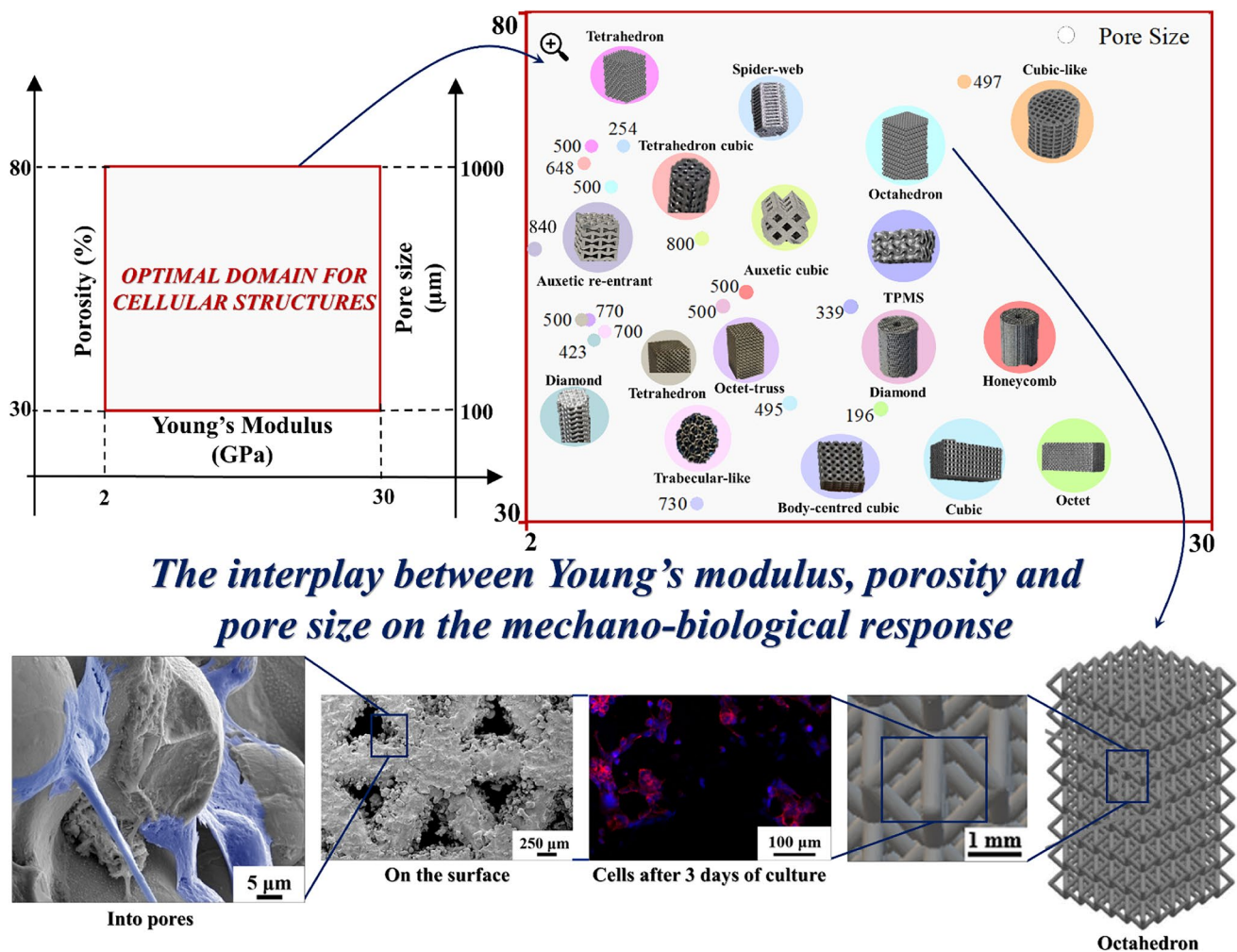
Fig. 24 The interplay between Young's modulus, porosity, and pore size on the mechano-biological response of cellular structures targeting the orthopedic field (adapted and schematized from references [196, 209, 213–219])

impurities while ensuring the production of intricately designed components.

This chapter provides an extensive overview of the full-scale prototypes of hip implants integrating cellular structured features. However, there remains a lack of evidence regarding the biological evaluation and clinical outcomes in the case of the study, emphasizing the need for further research in the clinical application of implants integrating cellular structures. Table 7 presents the specifics of these implementations for further clarification.

4.1 Case of study 1

Three types of unit cells, namely the body-centered cubic, diamond, and rhombic dodecahedron, were chosen to design meta-implants for deformable acetabular cups. These selections were based on the unit cell's relatively high Poisson's ratio and low Young's modulus. A graded relative density

was proposed in three steps, ranging from 10% on the inside to the minimum printable density determined by the minimum printable strut diameter of 200 μm. The relative density values varied depending on the unit cell, with 2% for the diamond and body-centered cubic and 10% for the rhombic dodecahedron.

A total of 27 specimens were fabricated using the DMP 320 (now known as DMP Flex 350) equipment and CP-Ti powder. To assess the mechanical behavior of the specimens, 27 moulds were prepared using a bone-mimicking material that exhibited common shape features of the natural acetabulum (Fig. 25), particularly the Paprosky Type 2B defect. These moulds accommodated the displacement of all the samples.

For the experimental setup, a compressive load was applied in an axial direction using a static test machine equipped with a 20 kN load cell (Fig. 25). To simulate the loading conditions in the human acetabulum, a 25-mm steel

Table 7 Cases of study of hip implant components, acetabular and femoral, including cellular structures (N.p. as not provided)

Case of Study	Unit Cell	Manufac. Tech.	Equipment	Material	Implant	Refs.
	Body-Centred Cubic					[243]
1	Diamond	LPBF	DMP Flex 350	CP-Ti powder		[243]
	Rhombic Dodecahedron					[243]
2	Vintile	LPBF	SLM-125	Ti6Al4V		[244]
3	Undefined	LPBF	Concept laser M2	Type 4 titanium alloy		[245]
4	Cubic	LPBF	EOS M280	Ti6Al4V		[246]
5	Diamond cubic	LPBF	EOSINT M280	Ti6Al4V		[247]
6	Diamond cubic	LPBF	EOSINT M280	Ti6Al4V		[248]
7	Hybrid Structure: Auxetic and conventional	LPBF	N.p.	Ti6Al4V-ELI		[249]
8	Rhombic dodecahedron	EBM	N.p.	Ti6Al4V		[250]
9	Rhombic dodecahedron	EBMP	N.p.	Titanium alloy		[251]
10	Stochastic	LPBF	EOSINT M 280	Titanium Ti64		[252]
11	Tetrahedron	LPBF	Renishaw AM250	Titanium		[253]
12	Vintile	LPBF	EOS-M290	Ti6Al4V		[263]

Fig. 25 (**a**) Body-centered cubic (left) and diamond (right) acetabular components. (**b**) Rhombic dodecahedron acetabular component (left) and mould fabricated with bone-similar material (right). (**c**) The experimental setup used to evaluate the deformation and space-filling of the samples produced (images reproduced with permission from [243])
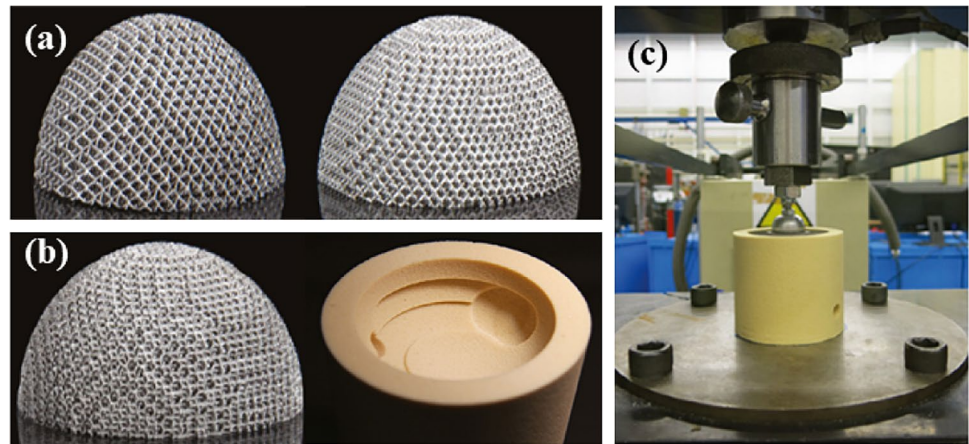
ball exerted a constant displacement of 0.5 mm/min on the inner hemisphere of the cellular cup until a maximum displacement of 5 mm was reached. The mechanical results, such as Yield strength, Young's modulus, Ultimate Compressive strength, and others, were not achieved, and the mechanical behavior evaluated focused on the deformation that the implant would suffer as well as the deformation it would cause in the implant-bone interface.

The authors concluded that the functionally graded designs could produce the desired deformation pattern in the mould, with the struts surrounding the solid hemisphere remaining intact while the unit cells in direct contact with the mould deformed into the defects. Among the three designs, the diamond-FG structure exhibited the most promising deformability and space-filling properties.

4.2 Case of study 2

Using CT (computed tomography) images, a 3D acetabular cup was reconstructed, and the selected unit cell was applied to create structures with different sizes, porosities, and optimization (variable density).

These structures were fabricated using the SLM-125 equipment with a 200 WCW ytterbium fiber laser in an argon atmosphere. The resulting structures closely resembled the CAD design, with circular beams in the cross-sectional area and spherical cores, as shown in Fig. 26. Although the morphology did not exhibit a balling effect in the beams, cracks measuring approximately 15 μm in length and less than 0.5 μm in width were observed. Bonded particles, which were not fully melted, were also present on the surface of the beams. The authors attributed this phenomenon to the partially melted metallic powder at the boundary of the beams, as the powder had a similar size to these particles.

To validate the simulation results, compression tests were conducted following the ASTM standard D1621-10. The compressive load was applied along the build orientation with a strain rate of 0.1 mm/min until a plastic deformation range of 20 mm was reached. As anticipated, the Yield strength, Young's modulus, and Ultimate Compressive strength exhibited a linear decrease with an increase in unit size and porosity.

The study demonstrated that the acetabular cup with the vintiles lattice topology possessed high porosity, good interconnectivity, and sufficient stability to withstand normal loads. Young's modulus of both optimized AC cellular implants ranged between 5 and 13 GPa, which fell within the range of Young's modulus of human bone (estimated to be between 0.3 and 20 GPa, according to the authors). The optimized structures also exhibited lower porosity and pore size compared to the non-optimized structures, thereby enhancing the mechanical performance and stability of the implants.

4.3 Case of study 3

This case differs from the others analyzed as the authors did not print an initial acetabular implant but rather an acetabular revision endoprosthesis. They utilized an Ultimaker2Go printer to create a PLA acetabulum prototype based on multislice-computerized tomography results of acetabulum defects in four patients. These 3D models were generated to verify the optimal positions of screw holes and the resulting fixation of the device.

For the prosthesis, the acetabular device was fabricated using type 4 titanium alloy on a concept laser M2 printer, as shown in Fig. 27. It was determined that in cases with subtotal defects of the acetabulum, a hemisphere shape was the optimal choice for the implant, designed based on geodesic dome principles. For cases with total defects of the acetabulum, the implant shape corresponded to the shape of the missing parts in the acetabulum. The external surface of the implant featured a lattice structure to enhance osteointegration properties, while the internal surface was rough to allow for the use of cement in the individually prepared implant.

Similar to the first study, although the focus was different, the mechanical properties of the implants such as Yield strength, Young's modulus, and Ultimate Compressive strength were not assessed. The main objective was to evaluate the use of AM in the fabrication of implants, specifically examining patients with additively manufactured implants.

The authors concluded that the personalized approach in the reendothelization of hip joints with severe bone defects resulted in the complete filling of acetabular defects and successful endoprosthetization of the hip joint, with the
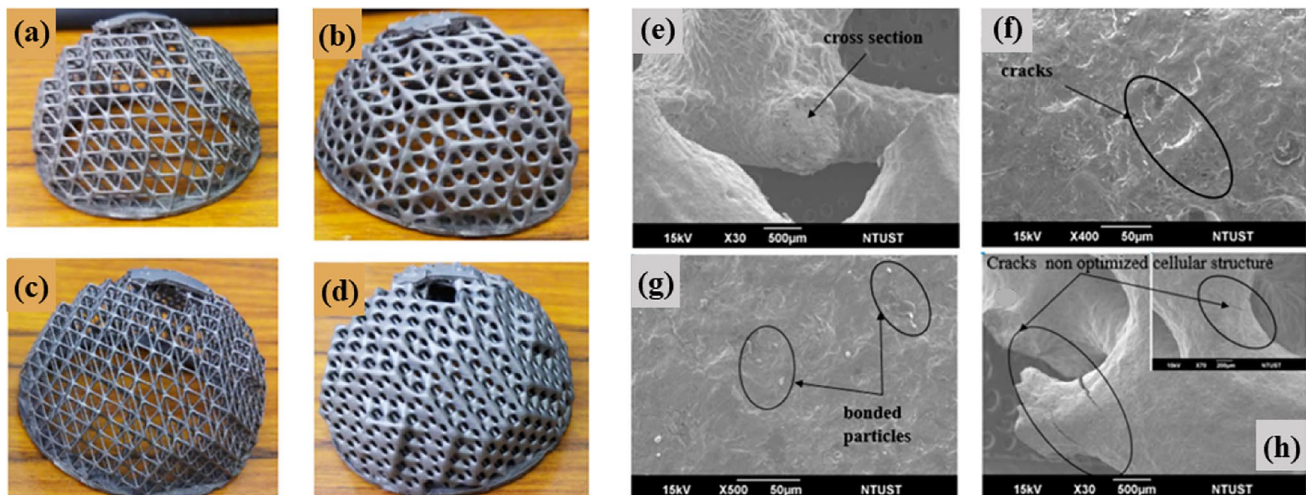
Fig. 26 On the left are cellular implants (AC) with vintiles structures built by the LPBF process: (**a**) non-optimized with 5×5×5 mm unit size, (**b**) optimized with 6×6×6 mm unit size, (**c**) non-optimized with 5×5×5 mm unit size, and (**d**) optimized with 5×5×5 mm unit size. On the right are SEM images of (**e**) the cross-section cellular implant with a vintiles cell size of 4×4×4 mm, (**f**) the cracks on the surface of the beam, (**g**) bonded particles on the surfaces of the beams, and (**h**) cracks on the non-optimized surface (images reproduced with permission from reference [244])

Fig. 27 (**a**) Acetabular component and (**b**) 3D bone model with the acetabular device implanted (images adapted from reference [245])
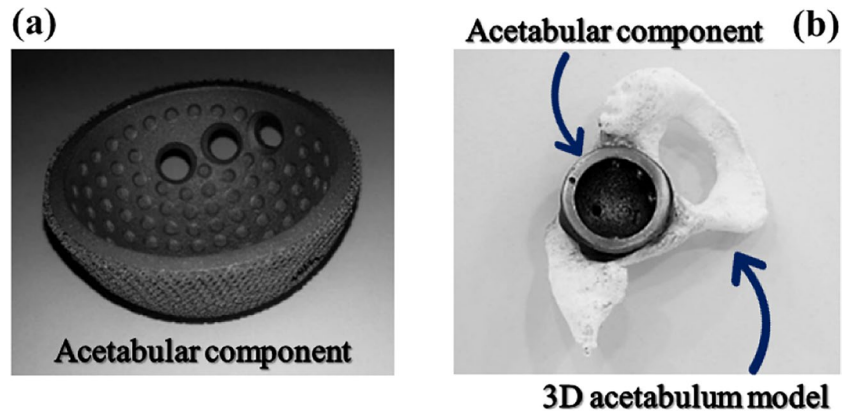
maximum restoration of the biomechanical axis and limb support function using a relatively safe technique. However, the cost of the technology, including preliminary computations for personalized treatment, imposes limitations on the widespread use of these techniques. Additionally, the development of supply and equipment bases, as well as the need for experienced and highly qualified specialists, would also entail significant costs.

4.4 Case of study 4

The authors defined the geometry of their implants on a survey conducted with expert surgeons and academicians working at different hospitals and universities. The unique geometry involved linking the outer and inner regions of the implant. The outer regions featured semi-spherical pores with cylindrical and cell channel shapes.

Nine specimens were built using the EOS M280 equipment: three solid implants (T1, T2, T3), three large pore implants with a pore diameter of 0.6 mm (BG1, BG2, BG3), and three small pore implants with a pore diameter of 0.3 mm (KG1, KG2, KG3). The specimens were sandblasted after production, and a reference implant (O) was produced by machining.

To assess the fatigue behavior of the samples, a servo-hydraulic fatigue test machine, Instron 8872, was used

with a 25 kN load and a 100 N torque capacity. During the compression test, an acrylic-based bone cement block was used to fix the implant in the defined position, as shown in Fig. 28. The stems of the implants were positioned to experience maximum loading in the proximal femur region. Sinusoidal compressive loads with a frequency of 15 Hz and limits ranging from 300 to 2300 N were applied to the implants, and the vertical displacements were measured using a displacement sensor connected to an actuator in the test machine after every 50,000 load cycles.

The authors concluded that, as expected, the displacements are directly proportional to the pore diameters. The reduction in cross-sectional area due to the increase in pore diameters resulted in higher displacements. They also highlighted that the deformation of the implants remained within the elastic region, and the maximum stresses occurred in the neck region of all implants. Despite the higher equivalent stress in the lightened implants, all implants were found to be successful after 5 million load cycles, leading the authors to conclude that the fatigue life for all the produced implants was infinite.

4.5 Case of study 5

The diamond lattice structure was selected due to its increased compliance compared to its cube or

Fig. 28 All specimens produced (**a**) and experimental setup (**b**) (images reproduced with permission from reference [246])

octahedron-based lattice counterparts, as observed in the mechanical tests in the studies by Ahmadi et al. [255], Zadpoor et al. [256], and Dumas et al. [257]. The authors used the EOSINT M280 system for fabricating the prototypes, and the unmelted powder was subsequently removed through a vibrating table and compressed air flow. However, the number of samples used was not disclosed. Afterward, the prototypes underwent thermal stress release and were blasted with aluminum oxide media to achieve the desired overall finish.

To assess the mechanical behavior, the stem was positioned and fixated to an aluminum tube filled with embedding medium, a positioning similar to that used in the fourth case of study (see Fig. 29). These tests were conducted using an MTS Alliance RF/200 testing machine equipped with a ± 10 kN load cell from the same manufacturer. The authors employed a different approach to force evolution in mechanical testing compared to the previously analyzed case studies. The tests were divided into two phases: incremental testing up to a maximum force of 1500 N (preconditioning), followed by constant-force testing for 3 cycles per field of view (FoV). The maximum force was chosen to ensure that the stems remained undamaged for subsequent studies. The experimental displacement maps were acquired using digital image correlation (DIC) with an ARAMIS 5 M stereoscopic camera system. Since a continuous 3D surface is required to construct a strain map using this technique, the asperities of the porous window of the stem were filled with hot glue before applying the spray of white background coating and black random speckle pattern.

When comparing the experimental results with the numerical ones, the authors identified relative differences between the full dense and porous stems of 8.1% and 7.1%, respectively. They attribute these variances to disparities between the numerical simulation and real boundaries. The stiffness of the fully dense stem was determined to be 2043 N/mm and 2222 N/mm in the numerical and experimental results, respectively. Similarly, the stiffness of the porous stem was evaluated at 1525 N/mm and 1417 N/mm, respectively.

Additionally, the authors analyzed two properties that were not previously mentioned in the studies: the surface-to-volume ratio (STVR) and the strength-to-stiffness ratio (STSR). They believe that the implant will provide a secure bone fixation if the STVR approaches that of the bone, which typically falls within the range of 3–5 mm^{-1}. The STVR depends directly on pore size, strut thickness, and porosity. The STSR, on the other hand, corresponds to the ratio of Yield strength to Young's modulus and is plotted as a function of porosity. A higher STSR is desired as it combines low stiffness with high strength, thereby potentially reducing stress shielding and increasing fatigue life.

When comparing the diamond lattice structure (with 800-μm pore size and porosity of 58%) to the stochastic cellular structure from another study [252] and to human bone, the authors discovered that the diamond structure exhibited an STVR close to that of bone, lower than the stochastic structure, and a higher STSR that was closer to bone and much higher than the stochastic structure.
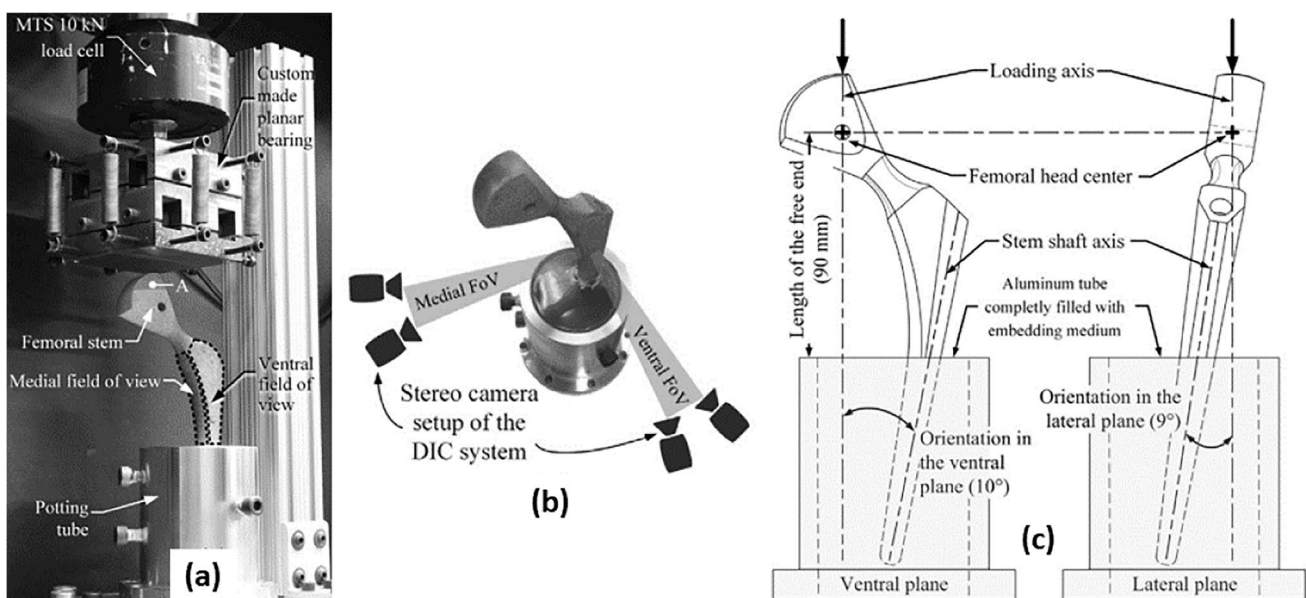
Fig. 29 (**a**) Experimental setup used for mechanical testing, (**b**) FoVs of the DIC setups, and (**c**) drawing of the specifications of the stem support (images reproduction with permission from reference [247])

The authors believe that the results of the correlation and deviation analysis between the numerical and experimental displacement and strain fields support and validate the numerical model. They defend that the analysis of STVR and STSR metrics should be combined with the analysis of Yield strength and Young's modulus. The authors suggest utilizing pore size and strut thickness gradients in specific locations within the femoral stem, as they believe this controlled transition would facilitate biological fixation and achieve optimal mechanical strength.

4.6 Case of study 6

The authors conducted mechanical testing on structures with three different configurations: an intact femur, a femur implanted with a fully dense stem, and a femur implanted with a stem incorporating a diamond cubic lattice structure. The choice of the diamond cubic lattice as the unit cell was based on several advantages perceived by the authors. These include quasi-isotropic mechanical properties, a self-supporting geometry suitable for LPBF, and an STVR similar to that of human bones. The porous stem was designed with a hollowed structure, and its core was filled with the diamond cubic lattice, as depicted in Fig. 30. All stems were fabricated using EOSINT M280 equipment.

The intact femur and the femurs used for stem implantation were obtained from SAWBONES® and belonged to the "model 3406," representing a large left composite femur. The femoral head was resected, and the stem was implanted and positioned according to the surgical protocol provided by the manufacturer, Stryker®. The femur orientation followed the guidelines outlined in the ISO 7206–4 (2010)

standard, which was developed for assessing the fatigue life of femoral stems. To ensure the alignment with the CAD model's orientation planes, both the intact and resected femurs were embedded in resin (AdTech Marine Systems ProBuild Epoxy Resin), as shown in Fig. 30. After allowing 24 h for the resin to solidify, one of the resected femurs was implanted with the fully dense stem, while the other one was implanted with the porous stem (Fig. 30).

Similar to studies 4 and 5, the femurs, both intact and with the stems, were secured within a tube embedded in a resin medium. To replicate the mechanical testing, an MTS Alliance RF/200 testing machine equipped with a $\pm$ 10 kN load cell from the same manufacturer as in study 5 was utilized. Full displacement fields were recorded using an ARAMIS 5 M stereoscopic camera. The testing procedure involved two phases: Initially, the load was incrementally increased up to a maximum of 3 kN. Subsequently, two cycles of loading and unloading were applied at the maximum force of 3 kN. This force was determined based on the maximum bodyweight force factor on the femoral head during daily activities [258], considering the corresponding body mass of 90.8 kg for the actual femur. The intact femur exhibited higher overall stiffness compared to its implanted counterparts.

The authors concluded that the comparison between the calculated and measured force–displacement diagrams, along with the finite element analysis (FEA) and experimentally measured (DIC) displacement and strain fields, demonstrated an acceptable agreement for all three construct configurations. Furthermore, they found that the porous stem reduced the surface ratio of bone resorption when compared to the bone remodeling onset of its dense counterpart. This

Fig. 30 (**a**) Fully dense femoral stem. (**b**) Implanted test constructs of the current study. (**c**) Femoral stem incorporating the cellular structure and showing a cutaway view of the internal structure in the distal part (image reproduction from reference [248])

(a)   (b)   (c)
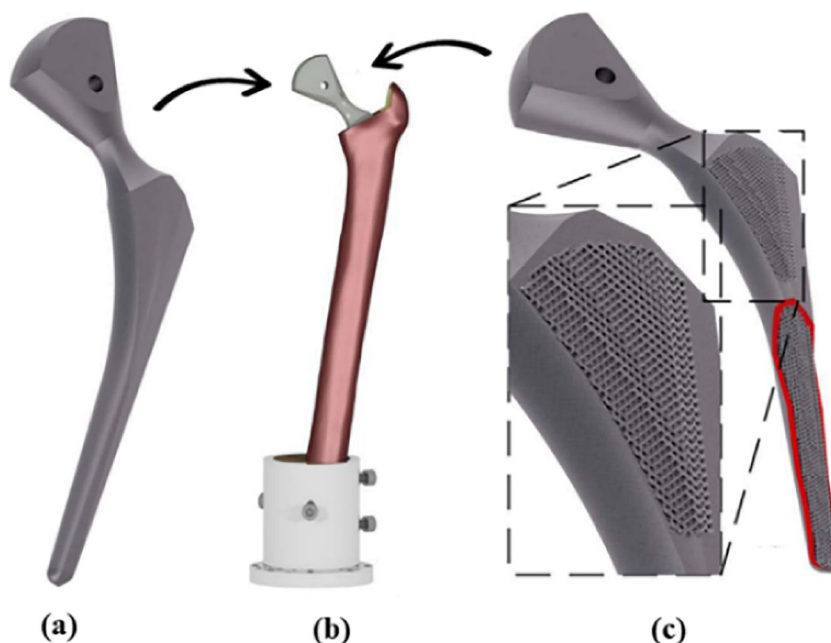
conclusion was drawn by comparing the numerically predicted equivalent strain fields of the implanted femurs to that of the intact femur, with a threshold level of $s = 0.6$. The chosen threshold value allowed a successful comparison of the numerically predicted bone mass redistribution in the implanted femurs with corresponding clinical dual-energy X-ray absorptiometry images.

4.7 Case of study 7

After conducting mechanical tests and observing a consistent bilateral compression profile extending along both borders, a new unit cell design was selected. This design involved a hybrid meta-biomaterial combining re-entrant and conventional hexagonal unit cells without a transitional region. The unit cell was implemented in three different ways, resulting in three hybrid implants: The first with a 50/50 cell ratio (H1), the second with a 50/50 cell ratio and a solid core (H2), and the third with a 70/30 cell ratio (H3). Two control implants were also used, consisting of a conventional design (C1) and an auxetic design (C2). All implants were manufactured using LPBF equipment. Subsequently, the samples were removed from the build plate, immersed in 96% ethanol, and subjected to ultrasonic cleaning for 10 min to remove excess powder.

To evaluate the performance of the implants, the authors aimed to simulate the implant-bone contact after surgery. The samples were enclosed on the medial and lateral sides in a bone-mimicking material, while the tip of the sample was clamped in an aluminum plate. This experimental setup, as depicted in Fig. 31, closely resembled the setup used in studies 4, 5, and 6, with the difference lying in the enclosed implant amount. For the compression test, a static testing machine with a 10 kN load cell was utilized, applying a maximum deformation of 1.5 mm to the femoral head at a rate of 0.5 mm/min. However, the mechanical results of the implants, such as Yield strength, Young's modulus, and Ultimate Compressive strength, were not obtained.

All implants exhibited compressive strains on the medial side, while the hybrid implants, where the auxetic and conventional unit cells were combined, demonstrated compression at the lateral implant-bone interface. The presence of a solid core surrounding the neutral axis appeared to amplify the expansion created by the unit cells, as the authors believed it affected the stiffness of the implants. Among all the implants, the H2 implant outperformed the others by generating a consistent compression profile along both defining lines of the implant. The bone interface is also illustrated in Fig. 31.

The authors claim to have discovered a novel meta-implant design that induces compression on both sides of the contact lines with the surrounding bone. This design aims to reduce the risk of bone-implant interface failure according to Hoffman's criterion, prevent the entry of wear particles into the interface space, minimize stress shielding, and enhance bone ingrowth.
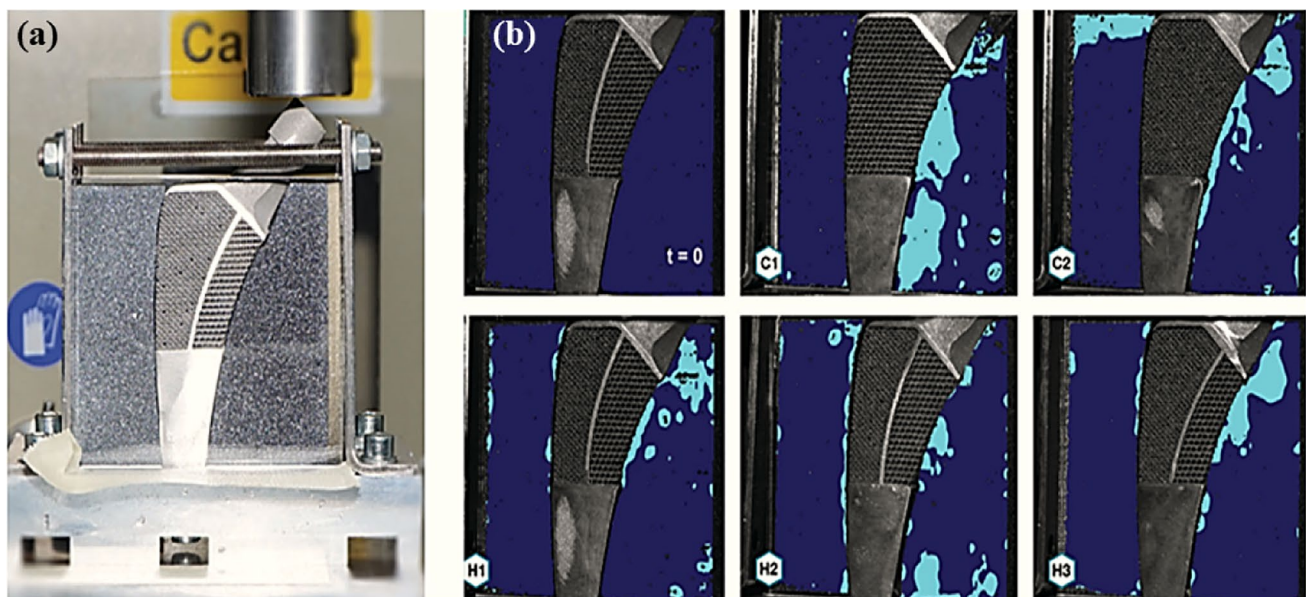
Fig. 31 (**a**) Experimental setup and (**b**) horizontal strains in the bone-mimicking materials surrounding the meta-implants at $t = 0$ and $t = 180$ s at 1.5 mm displacement for C1, C2, H1, H2, and H3 (image reproduction with permission from reference [249])

4.8 Case of study 8

After conducting and evaluating various mechanical tests on a group of different unit cell structures, the authors selected the dodecahedron rhombic unit cell for the femoral implant design. Solid necks were retained in the design to ensure compatibility with femoral heads and maintain a stable head-to-implant interface. Three types of implants were manufactured: solid, rhombic meshes, and stems with holes, as depicted in Fig. 32. These implants were all tested using the same experimental setup, where the distal end of the stem was anchored, and a load was applied to the stem neck at a rate of 1.27 mm/min, as shown in Fig. 32.

Unfortunately, specific mechanical results such as Yield strength, Young's modulus, and Ultimate Compressive strength were not obtained. However, the mechanical behavior of the implants is illustrated in a linear load–displacement relationship graph displayed in Fig. 32. The relative load/displacement ratio, compared to the solid stem, was quantified as 1.16 for the stem with holes and 2.38 for the rhombic dodecahedron stem.

Based on their findings, the authors concluded that the non-stochastic mesh structures, particularly the rhombic dodecahedron, allowed for the design of a hip stem with a lower bend modulus. This, in turn, leads to reduced stress shielding and more uniform bone remodeling.

4.9 Case of study 9

The implants, designed to resemble the outer surface dimensions of CoCr stems, were manufactured using EBM technology. The rhombic dodecahedron lattice structure was implemented in the stems, with customized orientation and size to approximate the modulus of cortical bone. Thirteen pairs of femora from skeletally mature large-breed dogs were obtained, and radiographic views (craniocaudal and mediolateral) were used to estimate the

mediolateral fit and craniocaudal fit, respectively. The stems were then hammered into the femur bones, and the positions around the medial aspect of the neck cuts were recorded.

To evaluate the mechanical behavior of the samples, UHMWPE cups were mounted on the crosshead, and an axial preload of 20 N was applied for 30 s. Subsequently, the cups were loaded four times at a rate of 0.1 mm/min up to 800 N. After that, the samples were preloaded again and loaded four times at the same rate up to 1600 N. The experimental setup, depicted in Fig. 33, was similar to the setups used in the previous studies (4 and 5), where the femur with the implanted stem was cut and embedded in polymethylmethacrylate, held at a 10° angle vertically by a custom jig.

The authors found that the lattice samples had a mean YM of 995 ± 80 N/mm, while the commercial stems had a YM of 1606 ± 240 N/mm. This indicated that the lattice samples were approximately 40% less stiff than the commercial ones. Additionally, the subsidence of the lattice stem after loading to 1600 N was measured to be 2.6 ± 1.1 mm, while the commercial stem subsided by 3.0 ± 1.6 mm (based on analysis of 7 pairs of femurs). One commercial sample exhibited subsidence of more than 10 mm at a load of 800 N, while the lattice sample from the opposite limb developed a fissure at the medial view of the femoral neck at a load of 1600 N. Another EBMP sample experienced subsidence of more than 10 mm at a load of 1600 N. Due to these failures, this pair of samples was excluded from the subsidence analyses and the analysis of bone surface strains at the 1600 N load.

Based on their findings, the authors concluded that the low-modulus lattice stems did not sustain damage or create femoral fissures or fractures during impaction and testing. Furthermore, these stems did not experience greater subsidence than the commercial stems during axial loading. Therefore, the authors suggest that lattice stems could be considered for clinical applications.
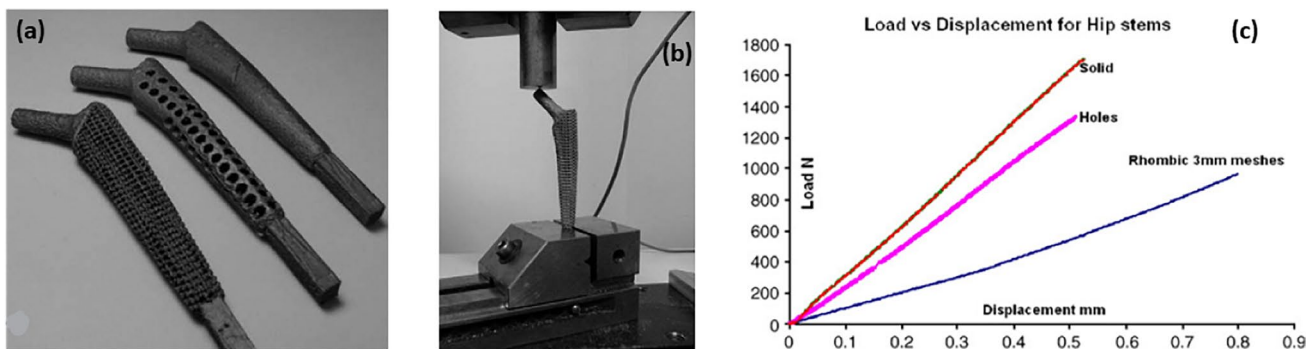
Fig. 32 (**a**) Hip stems with mesh, hole, and solid configuration. (**b**) Loading of mesh hip stem for flexure testing. (**c**) Results of bend testing of all the samples (image reproduction with permission from reference [250])
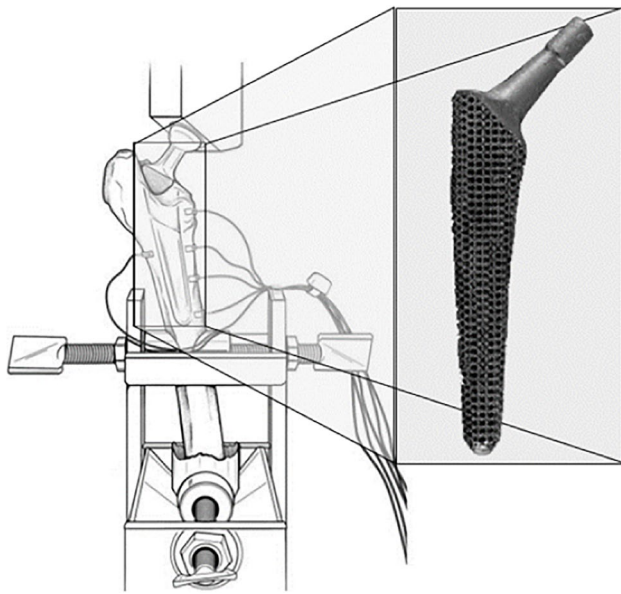
Fig. 33 Representation of the experimental setup and the femoral stem produced (image adapted from reference [251])
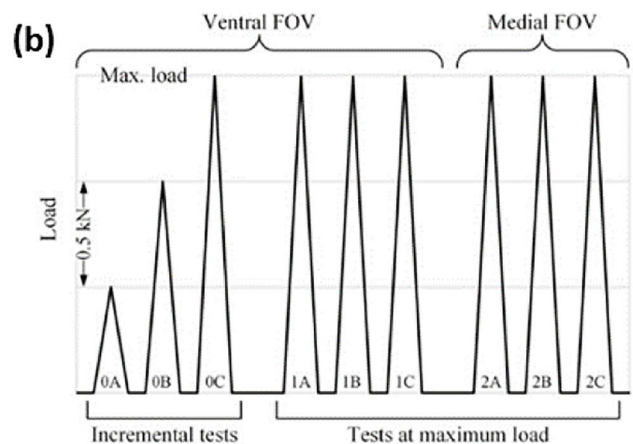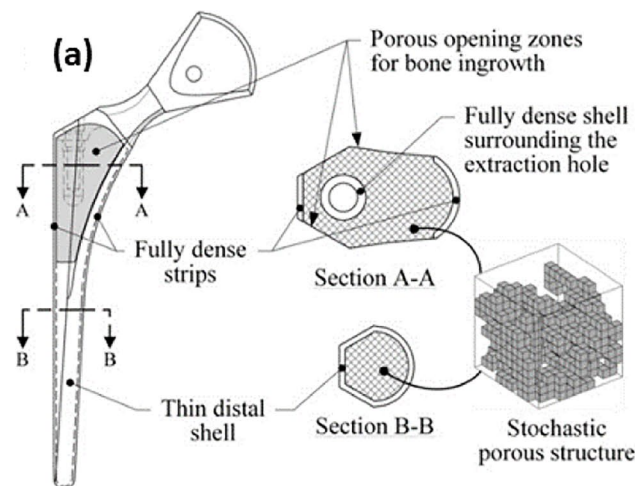
4.10 Case of study 10

A Stryker implant called Secur-FitTM Max was used as the basis for reverse engineering to create a CAD model of a femoral stem. Subsequently, a lattice structure was implemented in the CAD model. The modifications involved creating a stochastic open-cell structure by hollowing the distal tip to form a dense shell with an internal cellular structure. Two dense strips were added to join the distal shell and the neck region on the medial and lateral planes of the stem, leaving openings on the dorsal and ventral planes.

The remaining volume was filled with the cellular structure. These sections are illustrated in Fig. 34.

Using an EOSINT M 280 equipment, one porous and one dense femoral stem were manufactured. After the manufacturing process, the excess powder was removed using a vibrating table and compressed air, and heat treatment was conducted to release any residual stresses induced during processing. Similar to the previous cases studied, the distal section of the femoral stems was potted in an aluminum tube using epoxy resin for the experimental setup.

The tests were conducted using an MTS Alliance RF/200 equipment with a 10 kN load cell and a crosshead speed of 2 mm/min. To evaluate displacement and strain fields on the external surfaces of the femoral stem, a non-contact optical strain measurement system called ARAMIS 5 M v6.3 was used, along with DIC. Some sample preparations, such as applying hot glue, were done to ensure good image acquisition. For the mechanical testing, the porous stem was loaded up to 1.5 kN, while the dense stem was loaded up to 3 kN, with increments of 0.5 kN. Three consecutive tests were performed at the maximum load with a FOV on the ventral side. Subsequently, three consecutive tests were conducted at the maximum load with a medial FOV. The load test process is depicted in Fig. 34.

The authors concluded that the porous stem exhibited a 47% reduction in flexural Young's modulus compared to its dense counterpart. While the finite element (FE) model of the dense stem showed agreement with the experimental results, there was a poor correlation between the porous stem model and the experiment. After optimizing the FE model to account for the porosity offset, a significant but not complete decrease in the discrepancy between the modeling and the experiment was observed.

Fig. 34 (**a**) Porous stem with dense and porous material regions identification and (**b**) testing protocol (images reproduction with permission from reference [252])

4.11 Case of study 11

In pursuit of a femoral implant design commonly used in North America, the authors opted for a short stem with a single tapered wedge design as their optimal solution. The lattice structure utilized the tetrahedron unit cell, which has shown promising results in orthopedic applications and bone ingrowth. The optimum density distribution determined through numerical optimization was applied, resulting in a gradient porous microarchitecture within the implant, as depicted in Fig. 35.

The architectured samples were manufactured using the Renishaw AM250 equipment and underwent thermal treatment at 720 °C under argon for 2 h. The mechanical integrity of the cell struts was analyzed through CT scan images, confirming the absence of breaks or discontinuities among the elements. However, the presence of loose powder particles within the cell pores was observed, as shown in Fig. 35.

For the experimental evaluation, six fourth-generation femurs from Sawbones® were obtained. The femurs were resected at 22 cm from the tip of the greater trochanter and fixed at 12° flexion and 12° abduction angle by embedding them in epoxy resin, following a setup similar to the previous cases studied (4, 5, 6, and 7). The implants, including the solid control stem and the fully porous stems, were implanted in the femurs, and radiographs were taken to ensure consistent implant positioning, neck offset, and length. Subsequently, the femoral heads were loaded up to 2300 N, and the mechanical response was evaluated.

The mechanical results of the implants, including Yield strength, Young's modulus, Ultimate Compressive strength,

and others, were not achieved. As shown in Fig. 36, the fully porous stem exhibited a $71 \pm 14\%$, $7 \pm 7\%$, and $2 \pm 3\%$ surface bone loss at Gruen zones 7, 6, and 5, respectively. On the other hand, the fully solid stem showed $70 \pm 24\%$, $25 \pm 5\%$, and $7 \pm 10\%$ surface bone loss at the same zones, respectively, indicating a significant reduction in strain shielding, particularly in Gruen zone 6.

The authors believe that they have identified a reasonable FEA method for simulating and measuring volumetric bone loss. They also demonstrate that a high-strength, fully porous femoral stem with tailored mechanical properties can be designed and manufactured to reduce potential stress shielding in the bone.

4.12 Case of study 12

The selection of the vintile unit cell for this study was based on the authors' previous research [259], which identified it as the most mechanically efficient option among the six lattice topologies investigated: cubic, tetrahedron, hexagon, octagon, rhombic dodecahedron, and vintile. Notably, the vintile lattice exhibited minimal stress concentration, offered a high plateau stress lower strain, and boasted a greater number of bearing struts compared to the alternatives [259]. To produce the cellular hip implant, four distinct unit cell sizes and porosities were chosen.

A total of 12 cellular hip implants were produced using the EOS-M290 equipment, with 400 W Ytterbium fiber laser within an argon atmosphere. The manufactured implants are depicted in Fig. 37. Similar to the results in the second case of study, the resulting structures closely mirrored the CAD design, featuring circular beams in the cross-sectional area
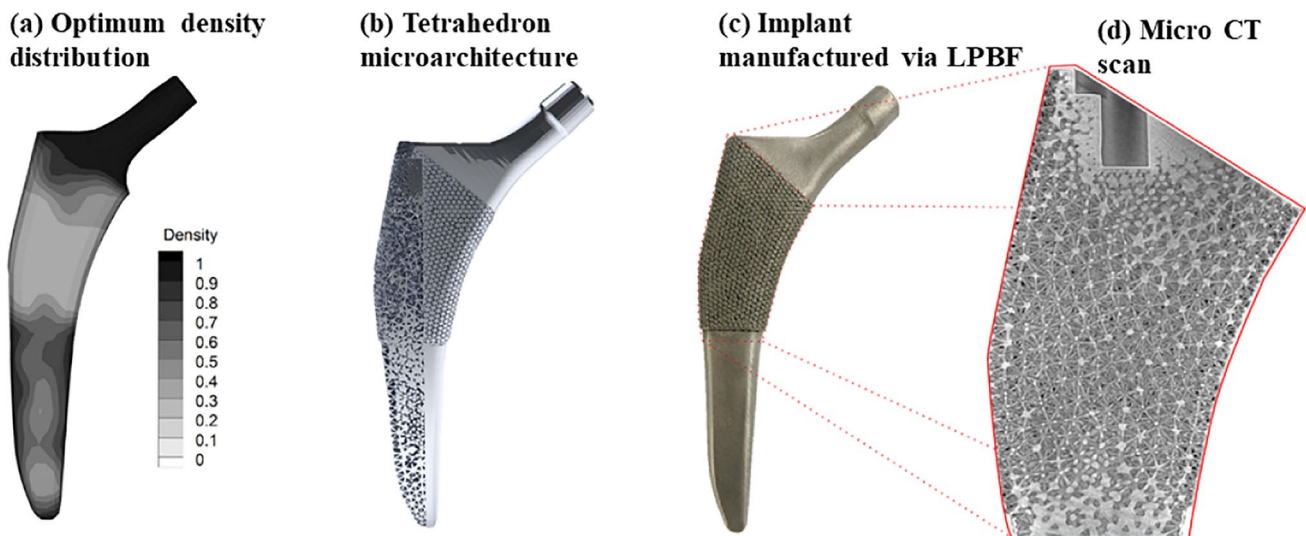
**Fig. 35** (**a**) Optimum relative density distribution of the fully porous implant. (**b**) Generation of lattice microarchitecture from optimal relative density distribution using a high-strength tetrahedron topology.

(**c**) Implant manufacturing via LPFB. (**d**) Micro-CT assessment of the implant lattice in the proximal region (images reproduced with permission from reference [253])

Fig. 36 Surface bone loss measurement obtained from the DIC experiment (image reproduced with permission from reference [253])
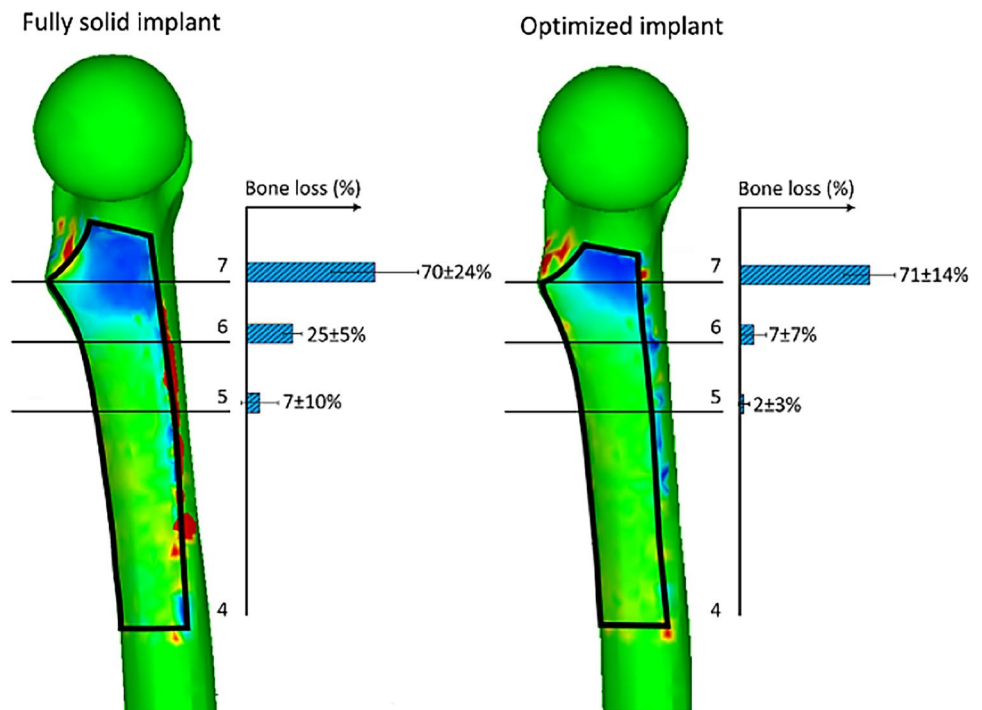
and spherical cores. While the morphology did not exhibit a balling effect within the beams, observations revealed the presence of cracks measuring less than 15 μm in length and 0.6 μm in width. Additionally, there were bonded particles on the beam surfaces, which had not fully melted. The authors attributed this phenomenon to the partially melted metallic powder at the beam boundaries, as the size of the powder particles closely matched that of these bonded particles.

The mechanical evaluation of the hip cellular implants, both from an FEA and experimental perspective, was conducted using the HT-2402 standard computer universal testing machines in accordance with ISO 7206–4 procedures. To ensure consistent testing conditions, the hip cellular implants were securely positioned within an aluminum cylindrical tube, which was subsequently filled with embedding acrylic resin. This positioning method mirrors that employed in the fourth and fifth cases of the study. The minimum and maximum loads were 300 N and 2330 N, respectively, with a 15-Hz frequency. Notably, the Ultimate Compressive strength, Yield stress, and stiffness exhibited an increase with decreasing pore diameter and porosity.

The authors observed congruent outcomes between the FEA simulations and the experimental tests. Their findings indicated good resistance to normal loads, excellent interconnectivity, high porosity, and an elastic modulus close to that of bone tissue. Abate et al. [254] believe that the use of their optimization technique has the potential to mitigate stress shielding by ensuring an uniform distribution of stress. Furthermore, the increase in pore size and porosity,
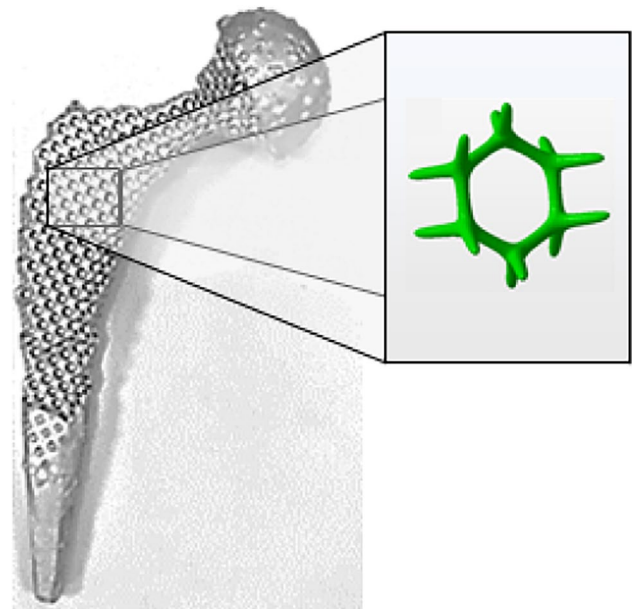
Fig. 37 Sample additively manufactured by LPBF with vintile unit cell (image adapted from references [254, 259])

as identified in their study, is believed to enhance initial implant stability and confer inherent flexibility reminiscent of natural bone. In conclusion, this additive manufacturing process emerges as a promising solution to produce cellular implants with anticipated and reliable mechanical performance.

5 Conclusions and future research directions

This review highlights the historical context of total hip arthroplasty and identifies the persistent need for innovation in the field despite prior advancements. Commercial solutions, including fully porous shells and coatings, are explored, along with the transformative potential of additive manufacturing. The primary objective was to offer insight into the mechanical performance of previously examined hip implants with cellular structures. The findings were organized into case studies, demonstrating advancements in durable implant development, although the replication of natural bone behavior and reduction of bone resorption posed ongoing challenges. The authors emphasize the necessity for additional fatigue and biological tests to improve implant effectiveness. While challenges persist in replicating natural bone behavior, progress has been made in creating durable implants.

The integration of cellular structures in hip implants presents significant challenges that warrant careful consideration. Ensuring the long-term structural integrity and mechanical stability of the implant remains a crucial concern, demanding thorough assessment to prevent premature failure. Attaining optimal osseointegration and long-term stability within the host bone poses another noteworthy challenge, requiring meticulous control to avoid complications like implant loosening and bone resorption.

Additionally, the design and manufacturing process may encounter limitations, impacting the production of tailored cellular structures for customized patient care. Striking a balance between design customization, material selection, and manufacturing feasibility is pivotal for successful implementation. Additionally, investigating the biocompatibility and potential immune responses to the materials used in cellular structures and implants is imperative, underlining the significance of comprehensive biocompatibility studies for ensuring patient safety and implant success.

Surgeons and trainees will require additional qualifications to navigate these complex implants, including learning new surgical procedures and techniques for evaluating and collecting patient data. Overall, addressing these challenges through rigorous research, advanced manufacturing techniques, and comprehensive biocompatibility studies is crucial to maximize the effectiveness and long-term success of cellular structures in hip implants.

Despite the potential complications, Additive Manufacturing remains a promising avenue for producing personalized hip implants with intricate cellular structures. With further research and development, this technology has the potential to facilitate mass production in a more sustainable manner, minimizing material waste. Its role in orthopedics is expected to expand significantly, offering a path toward more efficient, tailored, and sustainable solutions for patients in need of hip implants. Indeed, additive manufacturing represents the future of orthopedic interventions, demonstrating the possibilities of advanced manufacturing techniques in enhancing patient-specific care.

Declarations

Conflict of interest The authors declare no competing interests.

References

1. Gomez PF, Morcuende JA (2005) Early attempts at hip arthroplasty - 1700s to 1950s. Iowa Orthop J 25:2529
2. Canadian Institute for Health Information (2020) Hip and knee replacements in Canada: CJRR revision risk curves, 2018-2019-data tables
3. American Joint Replacement Registry (AJRR) (2019) 2019 Annual Report. American Academy of Orthopaedic Surgeons (AAOS), Rosemont, IL
4. Beck M, Brand C, Christen B, Zdravkovic V (2020) Swiss National Hip & Knee Joint Registry - Report 2020 - Annual Report of the SIRIS Registry. Hip & Knee:2012–2019
5. Portuguese Society of Orthopaedics and Traumatology (2013) 2013 Annual report: Portuguese arthroplasty register: 1–124

6. AOANJRR (2021) Hip, Knee and Shoulder Arthroplasty. 21:436

7. National Joint Registry (2021) 18th Annual NJR Report 2021. Natl. Jt. Regist. 3

8. National Joint Registry, 18th Annual NJR Report 2021. National Joint Registry. 3 (2021)

9. Hernigou P (2013) Earliest times before hip arthroplasty: from John Rhea Barton to Themistocles Glück. Int Orthop 37:2313–2318. https://doi.org/10.1007/s00264-013-2004-4

10. Eynon-Lewis NJ, Ferry D, Pearse MF (1992) Themistocles Gluck: an unrecognised genius. BMJ 305:19–26

11. Smith-Petersen MN (1948) Evolution of mould arthroplasty of the hip joint. J Bone Jt Surg 30:59–75

12. Judet J, Judet R, Paris F (1950) The use of an artificial femoral head for arthroplasty of the hip joint. J bone Jt Surg 32:166–173

13. Charnley J (1979) Low friction arthroplasty of the hip : theory and practice. Springer, Berlin Heidelberg

14. Wiles P (1958) The surgery of the osteo-arthritic hip. Br J Surg 45:488–497

15. Evans JT, Evans JP, Walker RW et al (2019) How long does a hip replacement last? A systematic review and meta-analysis of case series and national registry reports with more than 15 years of follow-up. Lancet (London, England) 393:647–654. https://doi.org/10.1016/S0140-6736(18)31665-9

16. OECD (2021) Health at a Glance 2021. Indicators:274

17. Klug A, Pfluger DH, Gramlich Y et al (2021) Future burden of primary and revision hip arthroplasty in Germany: a socio-economic challenge. Arch Orthop Trauma Surg 141:2001–2010. https://doi.org/10.1007/s00402-021-03884-2

18. Culliford D, Maskell J, Judge A et al (2015) Future projections of total hip and knee arthroplasty in the UK: results from the UK Clinical Practice Research Datalink. Osteoarthr Cartil 23:594–600. https://doi.org/10.1016/j.joca.2014.12.022

19. Singh JA, Yu S, Chen L, Cleveland JD (2019) Rates of total joint replacement in the United States: future projections to 2020–2040 using the national inpatient sample. J Rheumatol 46:1134–1140. https://doi.org/10.3899/JRHEUM.170990

20. Ghazlan A, Ngo T, Nguyen T et al (2020) Uncovering a high-performance bio-mimetic cellular structure from trabecular bone. Sci Rep 10:14247. https://doi.org/10.1038/s41598-020-70536-7

21. Bartolomeu F, Dourado N, Pereira F et al (2020) Additive manufactured porous biomaterials targeting orthopedic implants: a suitable combination of mechanical, physical and topological properties. Mater Sci Eng C 107:110342. https://doi.org/10.1016/J.MSEC.2019.110342

22. Bartolomeu F, Costa MM, Alves N et al (2021) Selective laser melting of Ti6Al4V sub-millimetric cellular structures: prediction of dimensional deviations and mechanical performance. J Mech Behav Biomed Mater 113:104123. https://doi.org/10.1016/j.jmbbm.2020.104123

23. Bartolomeu F, Gasik M, Silva FS, Miranda G (2022) Mechanical properties of Ti6Al4V fabricated by laser powder bed fusion: a review focused on the processing and microstructural parameters influence on the final properties. Metals (Basel) 12:986. https://doi.org/10.3390/met12060986

24. Cosma C, Drstvensek I, Berce P et al (2020) Physical-mechanical characteristics and microstructure of Ti6Al7Nb lattice structures manufactured by selective laser melting. Mater (Basel, Switzerland) 13:4123. https://doi.org/10.3390/MA13184123

25. Leonardo RA (1943) History of surgery. In: Press F (ed) History of Surgery. Froben Press, Michigan University, p 237

26. Rizzo TD (2020) Total hip replacement. In: Frontera WR, Silver JK (eds) Essentials of physical medicine and rehabilitation: musculoskeletal disorders, pain, and rehabilitation, 4th edn. Elsevier Inc, pp 337–345

27. Di Matteo B, Tarabella V, Filardo G et al (2013) John Rhea Barton: the birth of osteotomy. Knee Surgery, Sport Traumatol Arthrosc 21:1957–1962. https://doi.org/10.1007/s00167-013-2387-1

28. Selberg CM, Chidsey B, Skelton A, Mayer S (2020) Pelvic osteotomies in the child and young adult hip: indications and surgical technique. J Am Acad Orthop Surg 28:e230–e237

29. Barton JR (1827) On the treatment of anchylosis, by the formation of artificial joints. London Med Phys J 3:138–150

30. Boutin P (1972) Total arthroplasty of the hip by fritted alumina prosthesis. Experimental study and 1st clinical applications. Orthop Traumatol Surg Res 58:229–246. https://doi.org/10.1016/J.OTSR.2013.12.004

31. Gluck T, Brand RA (2011) The classic: report on the positive results obtained by the modern surgical experiment regarding the suture and replacement of defects of superior tissue, as well as the utilization of re-absorbable and living tamponade in surgery. Clinical Orthopaedics and Related Research. Springer, New York LLC, pp 1528–1535

32. Moore AT, Bohlman HR (2006) Metal hip joint: a case report. 1942. Clin Orthop Relat Res 453:22–24. https://doi.org/10.1097/01.blo.0000246558.27596.7a

33. Hernigou P, Quiennec S, Guissou I (2014) Hip hemiarthroplasty: from Venable and Bohlman to Moore and Thompson. Int Orthop 38:655–661. https://doi.org/10.1007/s00264-013-2153-5

34. Emery D, Britton A, Clarke H et al (1997) The Stanmore total hip arthroplasty A 15-to 20-year follow-up study. J Arthroplasty 12(7):728–735

35. Mckee GK, Watson-Farrar J (1966) Replacement of arthritic hips by the McKee-Farrar prosthesis. J bone Jt Surg 48:245–259

36. Ring PA (1968) Complete replacement arthroplasty of the hip by the ring prosthesis. J bone Jt Surg 50:720–731

37. Miguel Fonseca de Sousa L, Doutor António Paulo Monteiro Baptista P (2010) Comportamento Tribológico de Materiais para Prótese da Anca [Master's Thesis Faculdade de Engenharia da Universidade do Porto]

38. Tigani D, Fosco M, Ben Ayad R, Fantasia R (2012) Orthopaedic implant materials and design. In: Affatato S (ed) Wear of orthopaedic implants and artificial joints, 1st edn. Elsevier, pp 133–177

39. Briggs D (2013) The evolution of the femoral stem design in total hip arthroplasty. UNM Orthop Res J 2:10

40. Charnley J (1960) Surgery of the hip joint: present and future developments. Brithis Med J 1:821–826

41. Neri T, Philippot R, Klasan A et al (2018) Dual mobility acetabular cups for total hip arthroplasty: advantages and drawbacks. Expert Rev Med Devices 15:835–845. https://doi.org/10.1080/17434440.2018.1538781

42. Foxall-Smith M, Wyatt MC, Frampton C et al (2023) The 45-year evolution of the Mathys RM monoblock cups: have the paradigm shifts been worthwhile? HIP Int 33:193–202. https://doi.org/10.1177/11207000211067507

43. Williams HDW, Browne G, Gie GA et al (2002) The Exeter Universal cemented femoral component at 15 to 17 years: an update on the first 325 hips. J Bone Jt Surg 84:324–334. https://doi.org/10.1302/0301-620X.91B6.21627

44. Stryker (2020) Stryker's Exeter hip stem turns 50. https://www.stryker.com/pl/en/about/news/2020/stryker-s-exeter-hip-stem-turns-50.html. Accessed 5 Jul 2022

45. Hook S, Moulder E, Yates PJ et al (2006) The Exeter universal stem. J Bone Jt Surg - Ser B 88:1584–1590. https://doi.org/10.1302/0301-620X.88B12.18345/FORMAT/EPUB

46. Stryker (2018) Exeter ® V40 ® Femoral Stem using Exeter Broach: Surgical technique, Brochure

47. Maurer T, Ochsner P, Schwarzer G, Schumacher M (2001) Increased loosening of cemented straight stem prostheses made from titanium alloys. An analysis and comparison with prostheses made of cobalt-chromium-nickel alloy. Int Orthop 25:77–80. https://doi.org/10.1007/s002640000219

48. McLaughlin JR, Lee KR (1997) Total hip arthroplasty with an uncemented femoral component. J Bone Joint Surg Br 79(6):900–907. https://doi.org/10.1302/0301-620x.79b6.0790900

49. Vidalain J-P (2011) Twenty-year results of the cementless Corail stem. Int Orthop 35:189–194. https://doi.org/10.1007/s00264-010-1117-2

50. Erivan R, Villatte G, Brientini J-M et al (2019) 7-year results of primary total hip arthroplasty with the uncemented Avenir stem. HIP Int 29:418–423. https://doi.org/10.1177/1120700018810211

51. Stryker (2009) Exeter: technical guide. Brochure

52. Dubin JA, Westrich GH (2019) Anatomic dual mobility compared to modular dual mobility in primary total hip arthroplasty: a matched cohort study. Arthroplast Today 5:509–514. https://doi.org/10.1016/j.artd.2019.09.006

53. Zimmer Biomet (2020) G7 ® Acetabular System, Brochure

54. DePuy Synthes J& J (2022) PINNACLE® Acetabular cup. https://www.jnjmedtech.com/en-US/product/pinnacler-acetabular-cup-system. Accessed 23 May 2022

55. Zimmer Biomet (2019) Avenir Complete™ Hip System, Brochure

56. Zimmer Biomet (2021) Fitmore ® Hip Stem: Surgical Technique, Brochure

57. Miranda G, Araújo A, Bartolomeu F et al (2016) Design of Ti6Al4V-HA composites produced by hot pressing for biomedical applications. Mater Des 108:488–493. https://doi.org/10.1016/J.MATDES.2016.07.023

58. Nazari-Farsani S (2014) Precision and accuracy of marker-based and model-based radiostereometric analyses in determination of three-dimensional micromotion of a novel hip stem [Master's thesis, Department of Bioscience, Åbo Akademi University]

59. Holzwarth U, Cotogno G (2012) Total hip arthroplasty : state of the art, challenges and prospects. Publication Office of the European Union, Luxembourg. https://doi.org/10.2788/31286

60. Affatato S (2014) Contemporary designs in total hip arthroplasty (THA). In: Perspectives in total hip arthroplasty. Elsevier, pp 46–64

61. Pivec R, Johnson AJ, Mears SC, Mont MA (2012) Hip arthroplasty. The Lancet 380(9855):1768–1777

62. Fischman D, Mahatma MM, Slullitel P et al (2022) Does a monoblock acetabular component with a ceramic liner cause more pelvic bone loss than a conventional modular cementless acetabular component? A 2-year randomized clinical trial. J Arthroplasty 37:75–82. https://doi.org/10.1016/j.arth.2021.08.033

63. Zajc J, Moličnik A, Fokter SK (2021) Dual modular titanium alloy femoral stem failure mechanisms and suggested clinical approaches. Materials 14(11):3078

64. Stulberg SD, Patel RM (2013) The short stem: promises and pitfalls. Bone Joint J 95-B:57–62. https://doi.org/10.1302/0301-620X.95B11.32936

65. Feyen H, Shimmin AJ (2014) Is the length of the femoral component important in primary total hip replacement? Bone Jt J 96 B:442–448. https://doi.org/10.1302/0301-620X.96B4.33036

66. Demey G, Fary C, Lustig S et al (2011) Does a collar improve the immediate stability of uncemented femoral hip stems in total hip arthroplasty? A bilateral comparative cadaver study. J Arthroplasty 26:1549–1555. https://doi.org/10.1016/j.arth.2011.03.030

67. Al-Dirini RMA, Huff D, Zhang J et al (2018) Influence of collars on the primary stability of cementless femoral stems: a finite element study using a diverse patient cohort. J Orthop Res 36:1185–1195. https://doi.org/10.1002/jor.23744

68. Joint Replacement Market Size & Share Report, 2021–2028. https://www.grandviewresearch.com/industry-analysis/joint-replacement-market-report. Accessed 23 May 2022

69. Hip Replacement Implants Market to Experience Significant Growth by 2031 | BioSpace. https://www.biospace.com/article/hip-replacement-implants-market-to-experience-significant-growth-by-2031/. Accessed 23 May 2022

70. Hip Replacement Market Size & Share | Forecast Report 2021–2027. https://www.gminsights.com/industry-analysis/hip-replacement-market. Accessed 23 May 2022

71. Hip Replacement Market Analysis, Size, Trends | Global | 2018–2024 | MedCore - iData Research. https://idataresearch.com/product/hip-replacement-market/. Accessed 23 May 2022

72. Large Joint Device Market Analysis, Size, Trends | Global | MedSuite. https://idataresearch.com/product/large-joint-devices-market/. Accessed 23 May 2022

73. Zimmer Biomet Avantage Dual Mobility Cup System | Zimmer Biomet EU. https://www.zimmerbiomet.eu/en/products-and-solutions/specialties/hip/avantage-dual-mobility-cup-system.html. Accessed 23 May 2022

74. Zimmer Biomet (2011) Allofit ® /Allofit ®-S Alloclassic ® Acetabular Cup System, Brochure

75. Zimmer Biomet Total Hip Arthroplasty | G7 Acetabular System. https://www.zimmerbiomet.lat/en/medical-professionals/hip/product/g7-acetabular-system.html. Accessed 23 May 2022

76. DePuy Synthes J & J (2015) PINNACLE ® Hip Solutions: Surgical Technique, Brochure

77. DePuy Synthes J& J (2022) BI-MENTUM™ Dual Mobility System. In: BI-MENTUM™ Dual Mobil. Syst. https://www.jnjmedtech.com/en-US/product/bi-mentum-dual-mobility-system

78. DePuy Synthes J & J (2019) BI-MENTUM™ Dual Mobility Cup, Brochure

79. Stryker (2021) Trident . https://www.stryker.com/us/en/joint-replacement/products/trident.html. Accessed 23 May 2022

80. Stryker (2019) Design rationale Trident ® II Acetabular System, Brochure

81. Stryker (2019) Modular dual mobility acetabular system design rationale, Brochure

82. Stryker (2021) Anatomic dual mobility . https://www.stryker.com/us/en/joint-replacement/products/adm.html. Accessed 24 May 2022

83. Zimmer Biomet (2012) Design rationale taperloc complete hip system, Brochure

84. Zimmer Biomet Fitmore® Hip Stem | Zimmer Biomet EU. https://www.zimmerbiomet.eu/en/products-and-solutions/specialties/hip/fitmore-hip-stem.html. Accessed 23 May 2022

85. DePuy Synthes (2022) CORAIL hip system: Surgical Technique, Brochure

86. DePuy Synthes (2022) SUMMIT® hip system hip stems. https://www.jnjmedtech.com/en-US/product/summitr-tapered-hip-system. Accessed 23 May 2022

87. Synthes D C-STEM® AMT hip replacement. https://www.jnjmedtech.com/en-GB/product/c-stem-amt. Accessed 23 May 2022

88. Stryker (2021) Exeter . https://www.stryker.com/us/en/joint-replacement/products/exeter.html. Accessed 23 May 2022

89. Stryker (2021) Accolade II . https://www.stryker.com/us/en/joint-replacement/products/accolade-ii.html. Accessed 23 May 2022

90. Stryker (2020) Design rationale Accolade ® II Femoral Hip Stem, Brochure

91. Stryker (2022) Insignia® . https://www.stryker.com/us/en/joint-replacement/products/Insignia.html. Accessed 23 May 2022

92. Stryker (2021) Insignia hip stem, Brochure
93. Zimmer Biomet (2001) AVANTAGE ® Acetabulum System, Brochure
94. Jung JM, Kim CS (2014) Analysis of stress distribution around total hip stems custom-designed for the standardized Asian femur configuration. Biotechnol Biotechnol Equip 28:525–532. https://doi.org/10.1080/13102818.2014.928450
95. Erens GA, Walter B (2022) Complications of total hip arthroplasty - UpToDate. In: Complicat. Total hip Arthroplast. https://www.uptodate.com/contents/complications-of-total-hip-arthroplasty?search=osteolysis in implants&source=search_result&selectedTitle=2~150&usage_type=default&display_rank=2. Accessed 3 Jun 2022
96. Krumme JW, Bonanni S, Patel NK, Golladay GJ (2022) Technical considerations and avoiding complications in total hip arthroplasty. J Am Acad Orthop Surg Glob Res Rev 6:1–9. https://doi.org/10.5435/JAAOSGlobal-D-22-00234
97. Wilson M, Maggs J (2017) The relative merits of cemented and uncemented prostheses in total hip arthroplasty. Indian J Orthop 51:377–385. https://doi.org/10.4103/ortho.IJOrtho_405_16
98. Bastian D, Aguado-Maestro I, de Blas-Sanz I et al (2022) Dual mobility cups as the routine choice in total hip arthroplasty. Medicina (B Aires) 58:1–9. https://doi.org/10.3390/medicina58040528
99. Dawson-Amoah K, Raszewski J, Duplantier N, Waddell BS (2018) Dislocation of the hip: a review of types, causes, and treatment. Ochsner J 18:242–252. https://doi.org/10.31486/toj.17.0079
100. Alberio RL, Rusconi M, Martinetti L et al (2021) Total hip arthroplasty (THA) for Femoral neck fractures: comparison between standard and dual mobility implants. Geriatrics 6:1–9. https://doi.org/10.3390/geriatrics6030070
101. Gausden EB, Beiene ZA, Blevins JL et al (2021) Periprosthetic femur fractures after total hip arthroplasty: does the mode of failure correlate with classification? J Arthroplasty 36:2597–2602. https://doi.org/10.1016/J.ARTH.2021.02.048
102. Moreta J, Uriarte I, Bidea I et al (2021) High mortality rate following periprosthetic femoral fractures after total hip arthroplasty A multicenter retrospective study. Injury 52:3022–3027. https://doi.org/10.1016/J.INJURY.2021.01.035
103. Sershon RA, McDonald JF, Ho H, Hamilton WG (2021) Periprosthetic femur fracture risk: influenced by stem choice, not surgical approach. J Arthroplasty 36:S363–S366. https://doi.org/10.1016/j.arth.2021.02.012
104. Baba T, Uchino M, Ochi H et al (2021) Atypical periprosthetic femoral fractures after arthroplasty for fracture are at high risk of complications. Sci Reports 11:14378. https://doi.org/10.1038/s41598-021-93574-1
105. Sheth NP, Rozell JC, Paprosky WG (2019) Evaluation and Treatment of patients with acetabular osteolysis after total hip arthroplasty. J Am Acad Orthop Surg 27:e258–e267
106. Kandahari AM, Yang X, Laroche KA et al (2016) A review of UHMWPE wear-induced osteolysis: the role for early detection of the immune response. Bone Res 4:16014. https://doi.org/10.1038/boneres.2016.14
107. Skjöldebrand C, Tipper JL, Hatto P et al (2022) Current status and future potential of wear-resistant coatings and articulating surfaces for hip and knee implants. Mater Today Bio 15:100270. https://doi.org/10.1016/j.mtbio.2022.100270
108. Manfreda F, Bufi E, Francesco Florio E et al (2021) Osteolysis in total hip arthroplasty in relation to metal ion release: comparison between monolithic prostheses and different modularities. World J Orthop 12:768–780. https://doi.org/10.5312/wjo.v12.i10.768
109. Fernández-Fairén M, Torres-Perez A, Perez R et al (2020) Early short-term postoperative mechanical failures of current

110. Saleh KJ, Thongtrangan I, Schwarz EM (2004) Osteolysis: medical and surgical approaches. Clin Orthop Relat Res 427:138–147. https://doi.org/10.1097/01.blo.0000142288.66246.4d
111. Gallo J, Goodman SB, Konttinen YT, Raska M (2013) Particle disease: biologic mechanisms of periprosthetic osteolysis in total hip arthroplasty. Innate Immun 19:213–224. https://doi.org/10.1177/1753425912451779
112. Shah S, Kim SYR, Dubov A et al (2011) The biomechanics of plate fixation of periprosthetic femoral fractures near the tip of a total hip implant: cables, screws, or both? Proc Inst Mech Eng Part H J Eng Med 225:845–856. https://doi.org/10.1177/0954411911413060
113. Melo-Fonseca F, Miranda G, Domingues HS et al (2020) Reengineering bone-implant interfaces for improved mechanotransduction and clinical outcomes. Stem Cell Rev Reports 16:1121–1138. https://doi.org/10.1007/S12015-020-10022-9
114. Ebrahimi H, Rabinovich M, Vuleta V et al (2012) Biomechanical properties of an intact, injured, repaired, and healed femur: an experimental and computational study. J Mech Behav Biomed Mater 16:121–135. https://doi.org/10.1016/j.jmbbm.2012.09.005
115. Anderson DE, Madigan ML (2013) Effects of age-related differences in femoral loading and bone mineral density on strains in the proximal femur during controlled walking. J Appl Biomech 29:505–516. https://doi.org/10.1123/jab.29.5.505
116. Pivonka P, Park A, Forwood MR (2018) Functional adaptation of bone: the mechanostat and beyond. In: Pivonka P (ed) Multiscale mechanobiology of bone remodeling and adaptation, vol 578. CISM International Centre for Mechanical Sciences, Springer International Publishing, pp 1–60
117. Su SC, Skedros JG, Bachus KN, Bloebaum RD (1999) Loading conditions and cortical bone construction of an artiodactyl calcaneus. J Exp Biol 202:3239–3254. https://doi.org/10.1242/jeb.202.22.3239
118. Misch CE (2015) 7: Bone density: a key determinant for treatment planning - pocket dentistry. In: Implantology. https://pocketdentistry.com/7-bone-density-a-key-determinant-for-treatment-planning/. Accessed 25 Jan 2022
119. Frost HM (1994) Wolff's law and bone's structural adaptations to mechanical usage: an overview for clinicians. Angle Orthod 64:175–188
120. Tyrovola JB (2015) The "Mechanostat Theory" of frost and the OPG/RANKL/ RANK system. J Cell Biochem 116:2724–2729. https://doi.org/10.1002/jcb.25265
121. Allen MR, Burr DB (2013) Bone modeling and remodeling. In: Basic and applied bone biology. Academic Press, pp 75–90
122. Hillam RA, Goodship AE, Skerry TM (2015) Peak strain magnitudes and rates in the tibia exceed greatly those in the skull: an in vivo study in a human subject. J Biomech 48:3292–3298. https://doi.org/10.1016/j.jbiomech.2015.06.021
123. Coathup MJ, Blackburn J, Goodship AE et al (2005) Role of hydroxyapatite coating in resisting wear particle migration and osteolysis around acetabular components. Biomaterials 26:4161–4169. https://doi.org/10.1016/j.biomaterials.2004.10.020
124. Frost HM (1987) Bone "Mass" and the "Mechanostat": a proposal. Anat Rec 219:1–9
125. Sanjeev A (2004) Osteolysis - basic science, incidence and diagnosis. Curr Orthop 18(3):220–231. https://doi.org/10.1016/j.cuor.2004.03.002
126. Ulrich SD, Seyler TM, Bennett D et al (2008) Total hip arthroplasties: what are the reasons for revision? Int Orthop 32:597–604. https://doi.org/10.1007/s00264-007-0364-3

127. Malfroy Camine V, Terrier A, Pioletti DP (2017) Micromotion-induced peri-prosthetic fluid flow around a cementless femoral stem. Comput Methods Biomech Biomed Engin 20:730–736. https://doi.org/10.1080/10255842.2017.1296954

128. Leuridan S, Goossens Q, Roosen J et al (2017) A biomechanical testing system to determine micromotion between hip implant and femur accounting for deformation of the hip implant: assessment of the influence of rigid body assumptions on micromotions measurements. Clin Biomech 42:70–78. https://doi.org/10.1016/J.CLINBIOMECH.2017.01.009

129. Crosnier EA, Keogh PS, Miles AW (2014) A novel method to assess primary stability of press-fit acetabular cups. Proc Inst Mech Eng Part H J Eng Med 228:1126–1134. https://doi.org/10.1177/0954411914557714

130. Crosnier EA, Keogh PS, Miles AW (2016) The effect of dynamic hip motion on the micromotion of press-fit acetabular cups in six degrees of freedom. Med Eng Phys 38:717–724. https://doi.org/10.1016/J.MEDENGPHY.2016.04.014

131. Malfroy Camine V, Rüdiger HA, Pioletti DP, Terrier A (2018) Effect of a collar on subsidence and local micromotion of cementless femoral stems: in vitro comparative study based on micro-computerised tomography. Int Orthop 42:49–57. https://doi.org/10.1007/s00264-017-3524-0

132. Arvidson K, Abdallah BM, Applegate LA et al (2011) Bone regeneration and stem cells. J Cell Mol Med 15:718–746. https://doi.org/10.1111/j.1582-4934.2010.01224.x

133. Schwartz AM, Farley KX, Guild GN, Bradbury TL (2020) Projections and epidemiology of revision hip and knee arthroplasty in the United States to 2030. J Arthroplasty 35:S79–S85. https://doi.org/10.1016/J.ARTH.2020.02.030

134. Cook SD (1991) Porous coated total hip replacement system.U.S. Patent No. 5,004,476

135. Rohr WLJ, Swarts DF, Devanathan T et al (1996) Orthopaedic implant with bearing surface. European Patent Application (EPO) No EP0761242 A1

136. Cueille C, Pichon D (2003) Acetabular cup. European Patent Application No EP 1 290 992 A1

137. Sump KR (1987) Production of porous coating on a prosthesis. U.S. Patent No. 4,644,942

138. Schug M (1996) Process for the production of a bone implant and a bone implant produced thereby.U.S. Patent No. 5,571,185

139. Bales JP (2004) Method and apparatus for hindering osteolysis in porous implants. U.S. Patent No. 6,746,488 B1

140. Fridstand N, Gabel DW, Charlesbois SJ, et al (2012)Hip stem prosthesis. U.S. Patent No. 8,206,455 B2

141. Li Y, Li Y (2016) Artificial acetabulum with multi-layer shell core composite structure. U.S. Patent No. 2016/0220376 A1

142. Moreau P-E, Rouvray TL De, Brosset T, et al (2015) Cup for an orthopaedic implant, orthopaedic implant comprising such a cup and method for producing such a cup. U.S. Patent No. 2015/0012109 A1

143. Pressaco M, Lualdi G, Pria PD (2013)Prosthetic element and relative method to make it.U.S. Patent No. 8,454,705 B2

144. Jones E, Sutcliffe CJ, Stamp R (2006)Implant with laser-produced porous surface.European Patent Application No. 1 800 700 A2

145. Conway JS, Kelman DC, Lambert RD, et al (2022) Implant components and methods. U.S. Patent No. 2022/0039961 A1

146. Pasini D, Tanzer M, Arabnejad S, Johnston B (2021) Structural porous biomaterial and implant formed of same. U.S. Patent No. 2021/0045880 A1

147. Harris WH (1983) Stemmed femoral component for the human hip. U.S. Patent No. 4,406,023

148. Harris WH (1985) Stemmed femoral component for the human hip. U.S. Patent No. 4,514,865

149. Murray I (2007) Differential porosity prosthetic hip system. U.S. Patent No. 2007/0043446 A1

150. Brown DR, Meridew JD, Ronk RM, Hershberger TW (2007) Method and apparatus for use of porous implants. European Patent No. 1 820 475 A1

151. Brown DR, Meridew JD, Ronk RM, Hershberger TW (2012) Method and apparatus for use of porous implants. U.S. Patent No. 9,197,550 B2

152. Smith LW, Estes JF, Cowles RJ, Bruchmann H (1967)Prosthetic parts and methods of making the same. U.S. Patent No. 3,314,420

153. Zimmer Biomet (220AD) Zimmer biomet completes acquisition of A&E medical corporation. https://investor.zimmerbiomet.com/news-and-events/news/2020/12-01-2020-120239474. Accessed 29 Jun 2022

154. Charlesbois S, Blanchard C, Hawkins M, Swarts D (2004) Prosthetic device and method of making the same. U.S. Patent No. 2004/0098127 A1

155. Mcdaniel JM, Noblitt NL (1984) Prosthesis formation having solid and porous polymeric components. U.S. Patent No. 4:454,612

156. Crowninshield RD (1988) Femoral component and the method of constructing the same. U.S. Patent No. 4:718,912

157. Conway J, Landon RL, Shea JJ (2011) Implant components and methods. World Intellectual Property Organization Patent No. WO 2011/15651U A2

158. Birkbeck A, Collins R (2012) Surgical prostheses. U.S. Patent No. 2012/0116527 A1

159. Han S (2018) The fourth industrial revolution and oral and maxillofacial surgery. J Korean Assoc Oral Maxillofac Surg 44:205–206. https://doi.org/10.5125/jkaoms.2018.44.5.205

160. Cronskär M (2011) The use of additive manufacturing in the custom design of orthopedic implants. [Bachelor's Thesis, Department of Technology and Sustainable Development Mid Sweden University]

161. Javaid M, Haleem A (2020) Impact of industry 4.0 to create advancements in orthopaedics. J Clin Orthop Trauma 11:S491–S499. https://doi.org/10.1016/j.jcot.2020.03.006

162. Li B, Zhang M, Lu Q et al (2022) Application and development of modern 3D printing technology in the field of orthopedics. Biomed Res Int 2022:1–15. https://doi.org/10.1155/2022/8759060

163. Lyons R, Newell A, Ghadimi P, Papakostas N (2021) Environmental impacts of conventional and additive manufacturing for the production of Ti-6Al-4V knee implant: a life cycle approach. Int J Adv Manuf Technol 112:787–801. https://doi.org/10.1007/s00170-020-06367-7

164. Bartolomeu F, Costa MM, Alves N, et al (2020) Engineering the elastic modulus of NiTi cellular structures fabricated by selective laser melting. J Mech Behav Biomed Mater 110:103891. https://doi.org/10.1016/J.JMBBM.2020.103891

165. DebRoy T, Wei HL, Zuback JS et al (2018) Additive manufacturing of metallic components – process, structure and properties. Prog Mater Sci 92:112–224. https://doi.org/10.1016/J.PMATSCI.2017.10.001

166. McGregor M, Patel S, McLachlin S, Vlasea M (2021) Architectural bone parameters and the relationship to titanium lattice design for powder bed fusion additive manufacturing. Addit Manuf 47:102273

167. Ejnisman L, Gobbato B, de França Camargo AF, Zancul E (2021) Three-dimensional printing in orthopedics: from the basics to surgical applications. Curr Rev Musculoskelet Med 14:1–8. https://doi.org/10.1007/s12178-020-09691-3

168. Elenskaya N, Tashkinov M, Vindokurov I et al (2023) Understanding of trabecular-cortical transition zone: numerical and experimental assessment of multi-morphology scaffolds. J Mech

Behav Biomed Mater 147:106146. https://doi.org/10.1016/j.jmbbm.2023.106146

169. Hussain S, Nazir A, Waqar S et al (2023) Effect of additive manufactured hybrid and functionally graded novel designed cellular lattice structures on mechanical and failure properties. Int J Adv Manuf Technol. https://doi.org/10.1007/s00170-023-12201-7

170. Liu W, Sang L, Zhang Z et al (2023) Compression and resilient behavior of graded triply periodic minimal surface structures with soft materials fabricated by fused filament fabrication. J Manuf Process 105:1–13. https://doi.org/10.1016/j.jmapro.2023.09.034

171. Winhard BF, Haida P, Plunkett A et al (2023) 4D-printing of smart, nacre-inspired, organic-ceramic composites. Addit Manuf 77:103776. https://doi.org/10.1016/j.addma.2023.103776

172. Willems E, Turon-Vinas M, Camargo dos Santos B et al (2021) Additive manufacturing of zirconia ceramics by material jetting. J Eur Ceram Soc 41:5292–5306. https://doi.org/10.1016/j.jeurceramsoc.2021.04.018

173. Marques A, Cunha A, Gasik M et al (2023) 3D multi-material laser powder bed fusion: Ti6Al4V–CuNi2SiCr parts for aerospace applications. Prog Addit Manuf. https://doi.org/10.1007/s40964-023-00460-5

174. Iantaffi C, Bele E, McArthur D et al (2023) Auxetic response of additive manufactured cubic chiral lattices at large plastic strains. Mater Des 233:112207. https://doi.org/10.1016/j.matdes.2023.112207

175. Liu L, Minasyan T, Kamboj N et al (2020) Bio-inspired TiB2-TiB-TiN lattices by selective laser melting. Mater Lett 277:128337. https://doi.org/10.1016/J.MATLET.2020.128337

176. Yared W, Xie L, Gadow R (2023) Manufacturability and geometrical limitations of β-tricalcium phosphate-filled resins using LCD stereolithography. Open Ceram 16:100473. https://doi.org/10.1016/j.oceram.2023.100473

177. Hazlehurst KB, Wang CJ, Stanford M (2014) An investigation into the flexural characteristics of functionally graded cobalt chrome femoral stems manufactured using selective laser melting. Mater Des 60:177–183. https://doi.org/10.1016/J.MATDES.2014.03.068

178. Standard ASTM (2012) Standard terminology for additive manufacturing technologies. ASTM Int F2792–12a:1–9

179. Tshephe TS, Akinwamide SO, Olevsky E, Olubambi PA (2022) Additive manufacturing of titanium-based alloys- a review of methods, properties, challenges, and prospects. Heliyon 8:e09041. https://doi.org/10.1016/J.HELIYON.2022.E09041

180. Davoodi E, Montazerian H, Mirhakimi AS et al (2022) Additively manufactured metallic biomaterials. Bioact Mater 15:214–249. https://doi.org/10.1016/J.BIOACTMAT.2021.12.027

181. Depboylu FN, Yasa E, Poyraz Ö et al (2022) Titanium based bone implants production using laser powder bed fusion technology. J Mater Res Technol 17:1408–1426. https://doi.org/10.1016/j.jmrt.2022.01.087

182. Bartolomeu F, Costa MM, Alves N et al (2020) Engineering the elastic modulus of NiTi cellular structures fabricated by selective laser melting. J Mech Behav Biomed Mater 110:103891. https://doi.org/10.1016/J.JMBBM.2020.103891

183. Parvizi S, Hashemi SM, Asgarinia F et al (2021) Effective parameters on the final properties of NiTi-based alloys manufactured by powder metallurgy methods: a review. Prog Mater Sci 117:100739. https://doi.org/10.1016/j.pmatsci.2020.100739

184. Busachi A, Erkoyuncu J, Colegrove P et al (2017) A review of additive manufacturing technology and cost estimation techniques for the defence sector. CIRP J Manuf Sci Technol 19:117–128. https://doi.org/10.1016/J.CIRPJ.2017.07.001

185. Aslan B, Yıldız AR (2020) Optimum design of automobile components using lattice structures for additive manufacturing. Mater Test 62:633–639. https://doi.org/10.3139/120.111527

186. Hegab H, Khanna N, Monib N, Salem A (2023) Design for sustainable additive manufacturing: a review. Sustain Mater Technol 35:e00576. https://doi.org/10.1016/j.susmat.2023.e00576

187. Rodriguez Colon R, Nayak VV, Parente PEL et al (2023) The presence of 3D printing in orthopedics: a clinical and material review. J Orthop Res 41:601–613. https://doi.org/10.1002/jor.25388

188. Rouf S, Malik A, Singh N et al (2022) Additive manufacturing technologies: industrial and medical applications. Sustain Oper Comput 3:258–274. https://doi.org/10.1016/j.susoc.2022.05.001

189. Guo L, Ataollah Naghavi S, Wang Z et al (2022) On the design evolution of hip implants: a review. Mater Des 216:110552. https://doi.org/10.1016/j.matdes.2022.110552

190. Tamayo JA, Riascos M, Vargas CA, Baena LM (2021) Additive manufacturing of Ti6Al4V alloy via electron beam melting for the development of implants for the biomedical industry. Heliyon 7:e06892. https://doi.org/10.1016/J.HELIYON.2021.E06892

191. Chen LY, Liang SX, Liu Y, Zhang LC (2021) Additive manufacturing of metallic lattice structures: unconstrained design, accurate fabrication, fascinated performances, and challenges. Mater Sci Eng R Reports 146:100648

192. Miranda G, Faria S, Bartolomeu F et al (2016) Predictive models for physical and mechanical properties of 316L stainless steel produced by selective laser melting. Mater Sci Eng A 657:43–56. https://doi.org/10.1016/J.MSEA.2016.01.028

193. Rashid R, Masood SH, Ruan D et al (2017) Effect of scan strategy on density and metallurgical properties of 17–4PH parts printed by selective laser melting (SLM). J Mater Process Technol 249:502–511. https://doi.org/10.1016/J.JMATPROTEC.2017.06.023

194. Jang TS, Kim DE, Han G et al (2020) Powder based additive manufacturing for biomedical application of titanium and its alloys: a review. Biomed Eng Lett 10:505–516. https://doi.org/10.1007/s13534-020-00177-2

195. Choy SY, Sun CN, Leong KF, Wei J (2017) Compressive properties of Ti-6Al-4V lattice structures fabricated by selective laser melting: design, orientation and density. Addit Manuf 16:213–224. https://doi.org/10.1016/j.addma.2017.06.012

196. Bartolomeu F, Fonseca J, Peixinho N et al (2019) Predicting the output dimensions, porosity and elastic modulus of additive manufactured biomaterial structures targeting orthopedic implants. J Mech Behav Biomed Mater 99:104–117. https://doi.org/10.1016/J.JMBBM.2019.07.023

197. Genovese K, Leeflang S, Zadpoor AA (2017) Microscopic full-field three-dimensional strain measurement during the mechanical testing of additively manufactured porous biomaterials. J Mech Behav Biomed Mater 69:327–341. https://doi.org/10.1016/J.JMBBM.2017.01.010

198. Bai L, Zhang J, Chen X et al (1856) (2018) Configuration optimization design of Ti6Al4V lattice structure formed by SLM. Mater 2018:11. https://doi.org/10.3390/MA11101856

199. Günaydın AC, Yıldız AR, Kaya N (2022) Multi-objective optimization of build orientation considering support structure volume and build time in laser powder bed fusion. Mater Test 64:323–338. https://doi.org/10.1515/mt-2021-2075

200. Costa MM, Lima R, Melo-Fonseca F et al (2019) Development of β-TCP-Ti6Al4V structures: driving cellular response by modulating physical and chemical properties. Mater Sci Eng C 98:705–716. https://doi.org/10.1016/j.msec.2019.01.016

201. Onal E, Frith JE, Jurg M et al (2018) (2018) Mechanical properties and in vitro behavior of additively manufactured and

functionally graded Ti6Al4V porous scaffolds. Met 2018 8:200. https://doi.org/10.3390/MET8040200

202. Bartolomeu F, Abreu CS, Moura CG et al (2019) Ti6Al4V-PEEK multi-material structures – design, fabrication and tribological characterization focused on orthopedic implants. Tribol Int 131:672–678. https://doi.org/10.1016/J.TRIBOINT.2018.11.017

203. Lakes RS (1989) Cellular solids. J Biomech 22:397

204. Park K-M, Min K-S, Roh Y-S (2022) Design optimization of lattice structures under compression: study of unit cell types and cell arrangements. Materials (Basel) 15:97. https://doi.org/10.3390/ma15010097

205. Yang L, Harrysson O, West H, Cormier D (2012) Compressive properties of Ti-6Al-4V auxetic mesh structures made by electron beam melting. Acta Mater 60:3370–3379. https://doi.org/10.1016/J.ACTAMAT.2012.03.015

206. Schwerdtfeger J, Heinl P, Singer RF, Körner C (2010) Auxetic cellular structures through selective electron-beam melting. Phys status solidi 247:269–272. https://doi.org/10.1002/PSSB.200945513

207. Gunaydin K, Türkmen HS, Airoldi A et al (2022) Compression behavior of EBM printed auxetic chiral structures. Materials (Basel) 15:1520. https://doi.org/10.3390/ma15041520

208. Bari K, Arjunan A (2019) Extra low interstitial titanium based fully porous morphological bone scaffolds manufactured using selective laser melting. J Mech Behav Biomed Mater 95:1–12. https://doi.org/10.1016/j.jmbbm.2019.03.025

209. Liang H, Yang Y, Xie D et al (2019) Trabecular-like Ti-6Al-4V scaffolds for orthopedic: fabrication by selective laser melting and in vitro biocompatibility. J Mater Sci Technol 35:1284–1297. https://doi.org/10.1016/J.JMST.2019.01.012

210. Dara A, Bahubalendruni MAR, Johnney Mertens A, Balamurali G (2022) Numerical and experimental investigations of novel nature inspired open lattice cellular structures for enhanced stiffness and specific energy absorption. Mater Today Commun 31:103286. https://doi.org/10.1016/j.mtcomm.2022.103286

211. Amin Yavari S, Ahmadi SM, Wauthle R et al (2015) Relationship between unit cell type and porosity and the fatigue behavior of selective laser melted meta-biomaterials. J Mech Behav Biomed Mater 43:91–100. https://doi.org/10.1016/J.JMBBM.2014.12.015

212. Distefano F, Mineo R, Epasto G (2023) Mechanical behaviour of a novel biomimetic lattice structure for bone scaffold. J Mech Behav Biomed Mater 138:105656. https://doi.org/10.1016/j.jmbbm.2023.105656

213. Wang N, Meenashisundaram GK, Kandilya D et al (2022) A biomechanical evaluation on cubic, octet, and TPMS gyroid Ti6Al4V lattice structures fabricated by selective laser melting and the effects of their debris on human osteoblast-like cells. Biomater Adv 137:212829. https://doi.org/10.1016/j.bioadv.2022.212829

214. Arabnejad S, Burnett Johnston R, Pura JA et al (2016) High-strength porous biomaterials for bone replacement: a strategy to assess the interplay between cell morphology, mechanical properties, bone ingrowth and manufacturing constraints. Acta Biomater 30:345–356. https://doi.org/10.1016/j.actbio.2015.10.048

215. Deng F, Liu L, Li Z, Liu J (2021) 3D printed Ti6Al4V bone scaffolds with different pore structure effects on bone ingrowth. J Biol Eng 15:4. https://doi.org/10.1186/s13036-021-00255-8

216. Zhao D, Huang Y, Ao Y et al (2018) Effect of pore geometry on the fatigue properties and cell affinity of porous titanium scaffolds fabricated by selective laser melting. J Mech Behav Biomed Mater 88:478–487. https://doi.org/10.1016/J.JMBBM.2018.08.048

217. Wally ZJ, Haque AM, Feteira A et al (2019) Selective laser melting processed Ti6Al4V lattices with graded porosities for dental applications. J Mech Behav Biomed Mater 90:20–29. https://doi.org/10.1016/J.JMBBM.2018.08.047

218. Xiong Y-Z, Gao R-N, Zhang H et al (2020) Rationally designed functionally graded porous Ti6Al4V scaffolds with high strength and toughness built via selective laser melting for load-bearing orthopedic applications. J Mech Behav Biomed Mater 104:103673. https://doi.org/10.1016/j.jmbbm.2020.103673

219. Eldesouky I, Harrysson O, West H, Elhofy H (2017) Electron beam melted scaffolds for orthopedic applications. Addit Manuf 17:169–175. https://doi.org/10.1016/J.ADDMA.2017.08.005

220. Liu YJ, Ren DC, Li SJ et al (2020) Enhanced fatigue characteristics of a topology-optimized porous titanium structure produced by selective laser melting. Addit Manuf 32:101060. https://doi.org/10.1016/J.ADDMA.2020.101060

221. Caravaggi P, Liverani E, Leardini A et al (2019) CoCr porous scaffolds manufactured via selective laser melting in orthopedics: topographical, mechanical, and biological characterization. J Biomed Mater Res B Appl Biomater 107:2343–2353. https://doi.org/10.1002/JBM.B.34328

222. Jiang CP, Wibisono AT, Pasang T (2021) Selective laser melting of stainless steel 316L with face-centered-cubic-based lattice structures to produce rib implants. Mater (Basel, Switzerland) 14:5962. https://doi.org/10.3390/MA14205962

223. Li Y, Ding Y, Munir K et al (2019) Novel β-Ti35Zr28Nb alloy scaffolds manufactured using selective laser melting for bone implant applications. Acta Biomater 87:273–284. https://doi.org/10.1016/J.ACTBIO.2019.01.051

224. Novak N, Krstulović-Opara L, Ren Z, Vesenjak M (2020) Compression and shear behaviour of graded chiral auxetic structures. Mech Mater 148:103524. https://doi.org/10.1016/J.MECHMAT.2020.103524

225. Pagani S, Liverani E, Giavaresi G et al (2021) Mechanical and in vitro biological properties of uniform and graded cobalt-chrome lattice structures in orthopedic implants. J Biomed Mater Res Part B Appl Biomater 109:2091–2103. https://doi.org/10.1002/jbm.b.34857

226. Dhiman S, Singh M, Sidhu SS et al (2021) Cubic lattice structures of Ti6Al4V under compressive loading: towards assessing the performance for hard tissue implants alternative. Mater (Basel, Switzerland) 14:3866. https://doi.org/10.3390/MA14143866

227. Xiao Z, Yang Y, Xiao R et al (2018) Evaluation of topology-optimized lattice structures manufactured via selective laser melting. Mater Des 143:27–37. https://doi.org/10.1016/J.MATDES.2018.01.023

228. Melo-Fonseca F, Lima R, Costa MM et al (2018) 45S5 BAG-Ti6Al4V structures: the influence of the design on some of the physical and chemical interactions that drive cellular response. Mater Des 160:95–105. https://doi.org/10.1016/j.matdes.2018.08.056

229. Dallago M, Fontanari V, Torresani E et al (2018) Fatigue and biological properties of Ti-6Al-4V ELI cellular structures with variously arranged cubic cells made by selective laser melting. J Mech Behav Biomed Mater 78:381–394. https://doi.org/10.1016/J.JMBBM.2017.11.044

230. Pereira H, Cengiz IF, Maia FR et al (2020) Physicochemical properties and cytocompatibility assessment of non-degradable scaffolds for bone tissue engineering applications. J Mech Behav Biomed Mater 112:103997. https://doi.org/10.1016/j.jmbbm.2020.103997

231. Zhang Y, Sun N, Zhu M et al (2022) The contribution of pore size and porosity of 3D printed porous titanium scaffolds to osteogenesis. Biomater Adv 133:112651. https://doi.org/10.1016/j.msec.2022.112651

232. Amin Yavari S, Wauthle R, Van Der Stok J et al (2013) Fatigue behavior of porous biomaterials manufactured using selective laser melting. Mater Sci Eng C 33:4849–4858. https://doi.org/10.1016/J.MSEC.2013.08.006

233. Goto M, Matsumine A, Yamaguchi S et al (2021) Osteoconductivity of bioactive Ti-6Al-4V implants with lattice-shaped interconnected large pores fabricated by electron beam melting. J Biomater Appl 35:1153–1167. https://doi.org/10.1177/0885328220968218

234. Van Bael S, Chai YC, Truscello S et al (2012) The effect of pore geometry on the in vitro biological behavior of human periosteum-derived cells seeded on selective laser-melted Ti6Al4V bone scaffolds. Acta Biomater 8:2824–2834. https://doi.org/10.1016/j.actbio.2012.04.001

235. Parthasarathy J, Starly B, Raman S, Christensen A (2010) Mechanical evaluation of porous titanium (Ti6Al4V) structures with electron beam melting (EBM). J Mech Behav Biomed Mater 3:249–259. https://doi.org/10.1016/j.jmbbm.2009.10.006

236. Yang L, Han C, Wu H et al (2020) Insights into unit cell size effect on mechanical responses and energy absorption capability of titanium graded porous structures manufactured by laser powder bed fusion. J Mech Behav Biomed Mater 109:103843. https://doi.org/10.1016/j.jmbbm.2020.103843

237. Xu Z, Zhang Y, Wu Y et al (2022) In vitro and in vivo analysis of the effects of 3D-printed porous titanium alloy scaffold structure on osteogenic activity. Biomed Res Int 2022:1–13. https://doi.org/10.1155/2022/8494431

238. Yu T, Gao H, Liu T et al (2020) Effects of immediately static loading on osteointegration and osteogenesis around 3D-printed porous implant: a histological and biomechanical study. Mater Sci Eng C 108:110406. https://doi.org/10.1016/j.msec.2019.110406

239. Impens S, Chen Y, Mullens S et al (2010) Controlled cell-seeding methodologies: a first step toward clinically relevant bone tissue engineering strategies. Tissue Eng Part C Methods 16:1575–1583. https://doi.org/10.1089/ten.tec.2010.0069

240. Petrie RJ, Yamada KM (2012) At the leading edge of three-dimensional cell migration. J Cell Sci 125:5917–5926. https://doi.org/10.1242/jcs.093732

241. Michaud A, Swider ZT, Landino J et al (2021) Cortical excitability and cell division. Curr Biol 31:R553–R559. https://doi.org/10.1016/j.cub.2021.02.053

242. BogitiBurton J, Carter CE (2019) "General characteristics of the euprotista (Protozoa)" In: Human Parasitology (Fifth Edition) Elsevier, Oxford: 35–49.

243. Kolken HMA, de Jonge CP, van der Sloten T et al (2021) Additively manufactured space-filling meta-implants. Acta Biomater 125:345–357. https://doi.org/10.1016/j.actbio.2021.02.020

244. Abate KM, Nazir A, Chen J-E, Jeng J-Y (2019) Design, optimization, and evaluation of additively manufactured vintiles cellular structure for acetabular cup implant. Processes 8:25. https://doi.org/10.3390/pr8010025

245. Chegurov OK, Ovchinnikov EN, Stogov MV et al (2019) Design of individual components of the prosthesis for revision hip replacement. Biomed Eng (NY) 53:172–175. https://doi.org/10.1007/s10527-019-09902-3

246. Delikanli YE, Kayacan MC (2019) Design, manufacture, and fatigue analysis of lightweight hip implants. J Appl Biomater Funct Mater 17:228080001983683. https://doi.org/10.1177/2280800019836830

247. Jetté B, Brailovski V, Dumas M et al (2018) Femoral stem incorporating a diamond cubic lattice structure: design, manufacture and testing. J Mech Behav Biomed Mater 77:58–72. https://doi.org/10.1016/j.jmbbm.2017.08.034

248. Jetté B, Brailovski V, Simoneau C et al (2018) Development and in vitro validation of a simplified numerical model for the design of a biomimetic femoral stem. J Mech Behav Biomed Mater 77:539–550. https://doi.org/10.1016/j.jmbbm.2017.10.019

249. Kolken HMA, Janbaz S, Leeflang SMA et al (2018) Rationally designed meta-implants: a combination of auxetic and conventional meta-biomaterials. Mater Horizons 5:28–35. https://doi.org/10.1039/C7MH00699C

250. Harrysson OLA, Cansizoglu O, Marcellin-Little DJ et al (2008) Direct metal fabrication of titanium implants with tailored materials and mechanical properties using electron beam melting technology. Mater Sci Eng C 28:366–373. https://doi.org/10.1016/j.msec.2007.04.022

251. Marcellin-Little DJ, Cansizoglu O, Harrysson OLA, Roe SC (2010) In vitro evaluation of a low-modulus mesh canine prosthetic hip stem. Am J Vet Res 71:1089–1095. https://doi.org/10.2460/ajvr.71.9.1089

252. Simoneau C, Terriault P, Jetté B et al (2017) Development of a porous metallic femoral stem: design, manufacturing, simulation and mechanical testing. Mater Des 114:546–556. https://doi.org/10.1016/j.matdes.2016.10.064

253. Arabnejad S, Johnston B, Tanzer M, Pasini D (2017) Fully porous 3D printed titanium femoral stem to reduce stress-shielding following total hip arthroplasty. J Orthop Res 35:1774–1783. https://doi.org/10.1002/jor.23445

254. Abate KM, Nazir A, Jeng J-Y (2021) Design, optimization, and selective laser melting of vin tiles cellular structure-based hip implant. Int J Adv Manuf Technol 112:2037–2050. https://doi.org/10.1007/s00170-020-06323-5

255. Ahmadi SM, Campoli G, Amin Yavari S et al (2014) Mechanical behavior of regular open-cell porous biomaterials made of diamond lattice unit cells. J Mech Behav Biomed Mater 34:106–115. https://doi.org/10.1016/J.JMBBM.2014.02.003

256. Zadpoor AA, Hedayati R (2016) Analytical relationships for prediction of the mechanical properties of additively manufactured porous biomaterials. J Biomed Mater Res - Part A 104:3164–3174. https://doi.org/10.1002/jbm.a.35855

257. Dumas M (2016) Modélisation et simulation du comportement d'une tige fémorale poreuse. [PhD Thesis, École de Technologie Supérieure]

258. Bergmann G, Bergmann G, Deuretzabacher G et al (2001) Hip forces and gait patterns from routine activities. J Biomech 34:859–871

259. Abate KM, Nazir A, Yeh Y-P et al (2020) Design, optimization, and validation of mechanical properties of different cellular structures for biomedical application. Int J Adv Manuf Technol 106:1253–1265. https://doi.org/10.1007/s00170-019-04671-5

260. Hu CY, Yoon T-R (2018) Recent updates for biomaterials used in total hip arthroplasty. Biomater Res 22:1–12. https://doi.org/10.1186/s40824-018-0144-8

261. Alexander-Malhias M, De Martino I, Gu A et al (2019) Complete wear-through of a metal-backed acetabular cup in an ambulatory patient. Arthroplast Today 5:394–400. https://doi.org/10.1016/J.ARTD.2019.09.008

262. Huang Y, Shao H, Zhou Y et al (2019) Femoral bone remodeling in revision total hip arthroplasty with use of modular compared with monoblock tapered fluted titanium stems: the role of stem length and stiffness. J Bone Jt Surg - Am 101:531–538. https://doi.org/10.2106/JBJS.18.00442

263. Higuchi Y, Seki T, Takegami Y et al (2018) Same survival but higher rate of osteolysis for metal-on-metal Ultamet versus ceramic-on-ceramic in patients undergoing primary total hip arthroplasty after 8 years of follow-up. Orthop Traumatol Surg Res 104:1155–1161. https://doi.org/10.1016/J.OTSR.2018.08.005

264. Cahir JG, Toms AP, Marshall TJ et al (2007) CT and MRI of hip arthroplasty. Clin Radiol 62:1163–1171. https://doi.org/10.1016/J.CRAD.2007.04.018

265. Skedros JG, Mason MW, Bloebaum RD (2001) Modeling and remodeling in a developing artiodactyl calcaneus: a model for evaluating Frost's mechanostat hypothesis and its corollaries. Anat Rec 263:167–185. https://doi.org/10.1002/ar.1094

266. Baino F, Minguella-Canela J, Korkusuz F et al (2019) In vitro assessment of bioactive glass coatings on alumina/zirconia composite implants for potential use in prosthetic applications. Int J Mol Sci 20:722. https://doi.org/10.3390/ijms20030722

267. Ring PA (1971) Replacement of the hip joint. Ann R Coll Surg Engl 48(6):344–355

268. Zenz P, Stiehl JB, Knechtel H et al (2009) Ten-year follow-up of the non-porous Allofit cementless acetabular component. J Bone Jt Surg Br 91(11):1443–1447. https://doi.org/10.1302/0301-620X.91B11